

EFFECTS OF SUBSTRATE ON 2D MATERIALS, GRAPHENE, MOS_2 , WS_2 ,
AND BLACK PHOSPHORUS, INVESTIGATED BY HIGH TEMPERATURE
AND SPATIALLY RESOLVED RAMAN SCATTERING AND
PHOTOLUMINESCENCE

by

Liqin Su

A dissertation submitted to the faculty of
The University of North Carolina at Charlotte
in partial fulfillment of the requirements
for the degree of Doctor of Philosophy in
Electrical Engineering

Charlotte

2015

Approved by:

Dr. Yong Zhang

Dr. Raphael Tsu

Dr. Michael Fiddy

Dr. Qiuming Wei

ABSTRACT

LIQIN SU. Effects of substrate on 2D materials, Graphene, MoS₂, WS₂, and Black phosphorus, investigated by high temperature and spatially resolved Raman scattering and photoluminescence. (Under the direction of DR. YONG ZHANG)

The exploration of a group of new 2D materials, such as graphene and transition metal dichalcogenides, has become the hottest research of interest in recent years. With the dependable techniques of producing 2D materials, particularly mechanical exfoliation and chemical vapor deposition, we are able to study all kinds of their unique properties in mechanical, electrical and optical fields. In this dissertation, we examine the vibrational and thermal properties of four 2D materials – graphene, MoS₂, WS₂ and black phosphorus – as well as their interaction with the supporting substrates, by using temperature-dependent Raman spectroscopy. Regarding the increasing interests of studying on the fabrication and applications of 2D materials, the role of 2D-material/substrate interaction has seldom been taken into consideration which would significantly affects the quality of the grown films and the performance of the devices. To the best of our knowledge, we are the first to systematically investigate on this issue.

At first, we performed temperature-dependent Raman spectroscopy on two graphene samples prepared by CVD and ME up to 400 °C, as well as graphite as a reference. The temperature dependence of both graphene samples shows very non-linear behavior for G and 2D bands, but with the CVD-grown graphene more nonlinear. Comparing to the Raman spectra collected before the measurements, the spectra after the measurements exhibit not only a shift of peak position but also a huge broadening of linewidth, especially for CVD-grown graphene. This study implies that the polymeric residues from either scotch tape or PMMA during transfer process are converted to amorphous carbon after annealed at high temperature, which may significantly

change the optical and electrical properties of graphene.

With the same temperature-dependent Raman technique as graphene, we examine on monolayer MoS₂ and WS₂, and thin-film black phosphorus and demonstrate that the film morphology and the substrate play very important roles in modifying the properties of the materials. For the films transferred onto SiO₂/Si substrates, the E_{2g}^1 mode is only weakly affected by the substrate, whereas the A_{1g} mode is strongly perturbed, showing a highly nonlinear temperature dependence in Raman peak shift and linewidth. In contrast, for the films epitaxially grown on sapphire substrate, E_{2g}^1 is tuned more significantly by the substrate by showing a much smaller temperature coefficient than the bulk, while A_{1g} is less. A two-round temperature dependent Raman measurements on a transferred MoS₂ on SiO₂ sample confirm these findings. These experiments suggest that the film-substrate coupling depends sensitively on the preparation method, and in particular on the film morphology for the transferred film. Additionally, temperature-dependent PL spectroscopy of monolayer WS₂ shows a 0.2 eV activation energy for CVD-grown films on SiO₂/Si substrate.

Besides temperature dependent Raman spectroscopy, we also perform PL and Raman mappings on monolayer WS₂ triangles prepared by both chemical vapor deposition and transfer, and find both Raman and PL are very sensitive to strain and doping effects. The non-uniform strain distribution over one single triangle is determined both qualitatively and quantitatively through the shift of E_{2g}^1 mode and PL peak energy. In transferred WS₂ monolayer, comparing to suspended WS₂ film a very strong PL quench in WS₂ film supported by SiO₂/Si substrate is observed, which is attributed to charge transfer between the film and the substrate.

Finally, the thermal conductivity of thin-film black phosphorus is determined by its temperature and laser power dependent Raman spectroscopy. An average thermal conductivity of a suspended black phosphorus film has been determined to be 15.8

$$K/(m \cdot W).$$

To my family, with love

ACKNOWLEDGEMENTS

If you decide to have a acknowledgements page, your acknowledgement text would go here.

The Acknowledgement page should be brief, simple, and free of sentimentality or trivia. It is customary to recognize the role of the advisor, the other members of the advisory committee, and only those organizations or individuals who actually aided in the project. Further, you should acknowledge any outside source of financial assistance, such as GASP grants, contracts, or fellowships.

TABLE OF CONTENTS

LIST OF FIGURES	xi
LIST OF TABLES	xv
LIST OF ABBREVIATIONS	1
CHAPTER 1: INTRODUCTION	1
1.1. Introduction	1
1.2. Outline	2
1.3. Structures and Properties of Layered 2D Materials	3
1.3.1. Graphene	3
1.3.2. Transition Metal Dichalcogenides (TMDs)	5
1.3.3. Black Phosphorus/Phosphorene	11
1.4. Fabrication of Layered Materials	13
1.4.1. Mechanical Exfoliation	14
1.4.2. Chemical Vapor Deposition	15
1.5. Aims of Research	17
CHAPTER 2: TEMPERATURE DEPENDENCE OF RAMAN SCATTERING AND PHOTOLUMINESCENCE	20
2.1. Temperature Dependence of Raman Scattering	20
2.1.1. Raman Scattering	20
2.1.2. Temperature Effect of Phonons	24
2.2. Temperature Dependence of photoluminescence	28
2.2.1. Photoluminescence	28
2.2.2. Temperature Dependence of Photoluminescence	30

2.3. Experimental Setups	32
CHAPTER 3: TEMPERATURE DEPENDENCE OF RAMAN SCATTERING IN GRAPHENE	35
3.1. Fabrication and Characterization of Graphene	35
3.1.1. Fabrication of Graphene	35
3.1.2. Characterization of Graphene Samples	36
3.2. Temperature Dependent Measurements and Results	43
3.3. Conclusions	47
CHAPTER 4: TEMPERATURE DEPENDENCE OF RAMAN SCATTERING IN MONOLAYER AND BILAYER MoS_2	49
4.1. Fabrication and Characterization of MoS_2 Samples	49
4.1.1. Sample Fabrication	49
4.1.2. Characterization of MoS_2 samples	49
4.2. Temperature Dependence of Raman Scattering	53
4.2.1. Temperature Dependent Raman Spectroscopy	53
4.2.2. Simulation for Temperature Dependence of Raman Shift	62
4.2.3. Full Width at Half Maximum (FWHM)	65
4.3. Annealing Effect on Monolayer MoS_2 Film Transferred on SiO_2/Si Substrate	66
4.4. Conclusions	76
CHAPTER 5: TEMPERATURE DEPENDENCE OF RAMAN AND PL IN MONOLAYER WS_2	79
5.1. Fabrication and Characterization of WS_2 Samples	79
5.1.1. Sample Fabrication	79

5.1.2. Characterization of WS ₂ samples	80
5.2. Temperature Dependence of Raman Scattering	87
5.3. Temperature Dependence of PL	92
5.4. Spatial Resolved Study on As-grown Monolayer WS ₂ Triangles	94
5.5. Conclusions	101
CHAPTER 6: TEMPERATURE DEPENDENCE OF RAMAN SCATTERING IN THIN-FILM BLACK PHOSPHORUS	104
6.1. Black Phosphorus Sample Preparation and Its Anisotropic Effects	104
6.1.1. Sample Preparation and Characterization	104
6.1.2. Anisotropic Effect of Raman Spectroscopy	106
6.2. Temperature Dependence of Raman in BP	109
6.3. Thermal Conductivity of BP	112
6.4. Conclusions	116
CHAPTER 7: CONCLUSIONS	117
REFERENCES	122
APPENDIX A: QUADRATIC FIT COMPARISON GRAPHS	133

LIST OF FIGURES

FIGURE 1.1: Lattice and band structures of graphene.	4
FIGURE 1.2: Crystal structure of MoS ₂ .	7
FIGURE 1.3: Band structure of bulk MoS ₂ .	8
FIGURE 1.4: Single-layer MoS ₂ devices: transistor and photodetector.	9
FIGURE 1.5: Electronic band structures and PL spectra of monolayer MoS ₂ and WS ₂ .	10
FIGURE 1.6: The lattice structure, PL spectra, and I-V characteristic of a few-layer phosphorene FET.	12
FIGURE 1.7: An illustration of the procedure of producing graphene from graphite by the technique of mechanical exfoliation with the scotch tape.	15
FIGURE 1.8: An illustration of the procedure of producing graphene from graphite by the technique of mechanical exfoliation with the scotch tape.	16
FIGURE 1.9: Growth techniques of MoS ₂ monolayers.	17
FIGURE 2.1: The displacement of planes of atoms.	24
FIGURE 2.2: Sketch of the basic processes involved in a typical photoluminescence of semiconductors.	29
FIGURE 2.3: Confocal microscope.	32
FIGURE 2.4: Experimental setups.	33
FIGURE 3.1: Optical images of graphene samples and graphite.	36
FIGURE 3.2: The Raman spectra of graphene and graphite.	39
FIGURE 3.3: Double resonance for the 2D peak.	41
FIGURE 3.4: G and 2D band Raman mapping results of ME graphene sample.	42

FIGURE 3.5: G and 2D band Raman mapping results of CVD-grown graphene sample.	42
FIGURE 3.6: Temperature dependence of Raman frequencies of (a) G and (b) 2D bands for the two graphene samples and graphite.	44
FIGURE 3.7: The representative Raman spectra at different temperatures for the two graphene samples and graphite.	44
FIGURE 3.8: The spectra before and after temperature-dependent Raman measurement.	46
FIGURE 4.1: The optical images of MoS ₂ samples.	50
FIGURE 4.2: The characterizations of all the six MoS ₂ samples.	51
FIGURE 4.3: MoS ₂ structure and Raman active modes.	52
FIGURE 4.4: The temperature dependence of E_{2g}^1 and A_{1g} modes for all six samples.	56
FIGURE 4.5: Representative Raman spectra of 1L-ME-SiO ₂ sample at selected temperatures.	57
FIGURE 4.6: Spatial maps ($6\mu m \times 6\mu m$) of the Raman frequencies of (a) E_{2g}^1 and (b) A_{1g} modes for 1L-ME-SiO ₂ sample, and the unit is cm ⁻¹ .	61
FIGURE 4.7: Raman spectra collected before and after temperature-dependent Raman measurements.	62
FIGURE 4.8: The modeling of temperature dependent Raman shift.	64
FIGURE 4.9: Temperature dependence of FWHM of E_{2g}^1 and A_{1g} modes in bulk and all other 1L and 2L samples.	66
FIGURE 4.10: The optical image and characterizations of the monolayer MoS ₂ film transferred onto SiO ₂ /Si substrate.	68
FIGURE 4.11: The Raman and PL mapping results of the monolayer MoS ₂ film.	70
FIGURE 4.12: The temperature dependence of Raman spectroscopy of monolayer MoS ₂ up to 305 °C.	72

FIGURE 4.13: The PL and Raman mapping results after the second-cycle heating.	76
FIGURE 5.1: The optical images of monolayer WS ₂ samples.	80
FIGURE 5.2: The characterizations of all WS ₂ samples.	82
FIGURE 5.3: The comparison of Raman spectra collected with 441.6 nm and 532 nm lasers.	84
FIGURE 5.4: Temperature dependence of Raman spectroscopy of all the WS ₂ samples.	88
FIGURE 5.5: The baseline correction of Raman signal from WS ₂ monolayer on sapphire.	88
FIGURE 5.6: The Raman spectra before and after temperature-dependent Raman measurements.	92
FIGURE 5.7: Temperature dependence of PL.	94
FIGURE 5.8: The Raman and PL mapping results of the monolayer WS ₂ triangle on sapphire.	96
FIGURE 5.9: DFT calculation of strain-induced Raman and PL shifts.	98
FIGURE 5.10: The optical characterizations of WS ₂ triangles after transferred.	100
FIGURE 6.1: Optical images and an AFM image of BP films.	105
FIGURE 6.2: Raman spectra of all the BP samples.	106
FIGURE 6.3: Anisotropic nature in Raman spectroscopy of BP.	108
FIGURE 6.4: Representative Raman spectra for S2 and S4 at different temperatures.	109
FIGURE 6.5: Temperature-dependent Raman spectroscopy of all the four BP samples.	110
FIGURE 6.6: Temperature-dependent of Raman spectroscopy of the suspended BP flake.	113

FIGURE 6.7: Laser power dependence of Raman spectroscopy for the suspended BP flake.

LIST OF TABLES

TABLE 4.1: Temperature coefficients of bulk, 1L and 2L samples with polynomial fitting to third order.	59
TABLE 4.2: The fitting parameters A and B for both E_{2g}^1 and A_{1g} modes used in three- and four-phonon coupling model.	64
TABLE 4.3: Temperature coefficient of E_{2g}^1 and A_{1g} modes in two temperature cycles.	71
TABLE 5.1: Relative intensities of Raman and PL of four monolayer WS_2 samples measured by two excitation wavelengths: 532 nm and 441.6 nm. For each column, the weakest intensity serves as unity reference.	84
TABLE 5.2: Temperature coefficients of bulk and 1L WS_2 samples.	91
TABLE 6.1: Temperature coefficients of Ag1, B2g and Ag2 modes of samples S1-S4, suspended and supported BP flakes.	112

CHAPTER 1: INTRODUCTION

1.1 Introduction

“There is plenty of room at the bottom,” prophesized the future of nanotechnology by the American physicist Richard Feynman in 1959. Feynman had described a process to manipulate individual atoms and molecules, where surface tension and van der Waals attraction would become more significant [1]. In the past decades, quite a few new detection techniques were invented, including atomic force microscope (AFM) [2], scanning electron microscope (SEM) [3,4], and tunneling electron microscope (TEM). With the assistance of these tools, more new materials, such as buckminsterfullerene (or bucky-ball, C_{60}) [5], and new structures, such as heterostructures and superlattices [6–8], were able to be discovered and investigated. The scale of materials was minimized from millimeter to nanometer. For years people have been asking this question: “How small can materials be?”

After a great amount of theoretical studies had been carried out on two-dimensional (2D) materials [9], the revolution took place in 2004 when graphene – atomically thin layers of graphite – was experimentally obtained by using Scotch tape, which brought the investigations of solid state materials into a new era – two-dimensional scale [10,11]. For the first time, it is possible to produce single 2D atomic layers of atoms in the lab. Following graphene came other new layered materials such as boron nitride (BN) [12,13], transition metal dichalcogenides (TMDs) [?, 14, 15], and black phosphorus (BP) [16,17]. The discovery of these materials has answered the question that we can actually produce thinnest objects imaginable – atomically thick.

With these new materials came new opportunities to examine old problems that have been studied in bulk or three-dimensional (3D) materials, as well as to find new ones specifically belonging to 2D structures. To study a new material, its physical and chemical properties are the first concerns. For example, as an electronic material, the covalent sp^2 C-C bond in graphene leaves one of carbon's four electrons free on surface giving the film a remarkably higher mobility than graphite [10, 11]. The new properties arising from the downscale of materials set up a new path for future applications. However, these findings also have suggested that the atomically thin layers are susceptible to perturbation within the film itself and from substrates to hold the film, which is in accord with Feynman's predication of the importance of surface tension and van der Waals force. These influences from the film and substrates can change the properties of the film to a significant extent so that thorough research needs to be carried out.

1.2 Outline

This dissertation presents systematic experiments on temperature-dependent high temperature Raman scattering of four 2D materials – graphene, molybdenum disulfide (MoS_2), tungsten disulfide (WS_2) and BP – to investigate their vibrational properties and the interaction between 2D materials and their substrates. For WS_2 , temperature-dependent high temperature photoluminescence were also performed. Spatially resolved Raman and PL mapping was used as well for selected materials. Chapters 1-2 include an overview of the basic concepts and literature work relevant to the experiments and results presented in Chapter 3-6. The experimental section begins in Chapter 3 where we carry out temperature-dependent high temperature Raman scattering on graphene. We find that the hydrocarbonization of polymeric residues leads to the broadening of D and G bands, and the temperature dependence is significant-

ly affected by the substrate due to the difference in thermal expansion of graphene with respect to the substrate. Temperature-dependent Raman scattering results on two typical TMDs – MoS₂ and WS₂ – are presented in Chapter 4 and 5, respectively, where we analyze the temperature-dependent behavior of Raman and PL. A modified form of the work on temperature-dependent Raman results in Chapter 4 has been published in *Nanoscale* 6, 4920 (2014), and the rest is under preparation. One part of Chapter 5 has appeared in *Nano Research* (2015), and the rest will be published separately. Chapter 6 extends this work on few-layer thin BP films to investigate the temperature coefficients of BP phonons as well as the thermal conductivity, where substrate effect on the properties of BP films is also discussed. The major content of this chapter has been published in *Applied Physics Letters* 107, 071905 (2015).

1.3 Structures and Properties of Layered 2D Materials

1.3.1 Graphene

Single-layer graphene (SLG) is the building block of graphite, whose lattice structure is shown Figure 1.1(a). The covalent C-C bonds of graphene are formed by sp²-hybridized orbitals through σ bond, giving rise to its extraordinary in-plane mechanical strength; whereas the remaining p-electron per atom can bind covalently with neighboring carbons to form a π band that is fully filled but with zero bandgap with the anti-bonding π^* band. Any perturbation that changes the occupation condition of the π or π^* band can lead to the change of electric conductivity [18, 19]. The unit cell of graphene comprises two atoms, denoted as A and B depicted in blue and red, respectively. The distance between nearest-neighbor carbons is 1.42 Å. In reciprocal space, the first Brillouin zone also has a hexagonal shape. With a tight-binding approach, the band structure is shown in Figure 1.1(b) where valence band maximum (VBM) and conduction band minimum (CBM) touch at K and K' points

at the corner of the first Brillouin zone. Within a small energy range near K points, a linear dispersion of electronic excitations is observed, which are called massless Dirac electrons [11]. This linear dispersion relation was first reported by P. R. Wallace in 1946 who showed the band structure of graphene as well as the unusual semimetallic behavior of graphite [9].

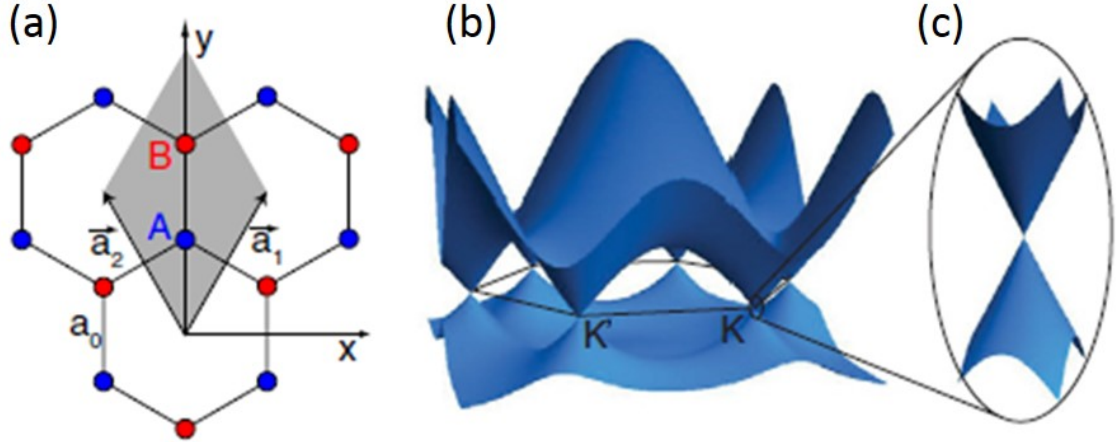


Figure 1.1: Lattice and band structures of graphene. (a) Lattice structure of graphene. a_0 is the nearest-neighbor distance. The unit cell is depicted in gray, together with the primitive lattice vectors $\vec{a}_{1,2}$. (b) Band structure of graphene. (c) The dispersion relation close to the K-point for small energies. Reproduced from F. Molitor et al. [19].

Multi-layer Graphene (MLG) or even bulk graphite consists of stacked graphene layers which are held together by weak van der Waals forces. The stacking order usually is Bernal stacking, i.e. ABA stacking. The distance between layers is 3.35 Å. For bilayer graphene, there are four energy bands if taking into account one $2p_z$ orbital on each of the four atomic sites in the unit cell: a pair of conduction bands and a pair of valence bands. Each pair has a splitting of ~ 0.4 eV over most of the Brillouin zone. Near the K points, one CBM and one VBM are split away from zero energy, whereas the other two bands touch at zero energy. Therefore, this region is relevant to electronic properties of bilayer graphene. For MLG, the band structure, though more bands exist, has two bands touching at K points, leading to its electronic

properties near K points similar to SLG [20].

SLG has quite a few promising and unique properties: negative thermal expansion coefficient (TEC) [21], unconventional integer quantum Hall effect [22], ultra-high mobility [23], valley polarization [24], etc. Unfortunately, graphene is a zero-gap material, which means it is not suitable or designable for use in electronic and optoelectronic devices. Bandgap engineering has been applied to open a bandgap in SLG, but the gap is only about a few hundred *meV* which is still too small [25–27]. Additionally, SLG, as an atomic layer, is susceptible to the influence of surrounding environment such as substrates and adsorbents. The non-uniform morphology of SLG like ripples and wrinkles can change its electronic structure and thus modify the thermal, mechanical and electrical behaviors of SLG. Instead, MLG, which is less susceptible to the external environment, was found to show similar behaviors as SLG, contributing to the diversities of graphene’s applications. Though graphene has zero gap which limits it to be used in FET applications, the extraordinary electrical, mechanical, thermal, and other multitudinous properties of graphene launch the potential applications such as flexible display screens, electrical circuits, and energy storage, as well as various medical, chemical and industrial processes with the use of new graphene materials [28, 29].

1.3.2 Transition Metal Dichalcogenides (TMDs)

As the first experimentally-discovered 2D material graphene has a zero bandgap, people started to search for other potential layered materials possessing direct bandgaps. Boron nitride has a graphene-like structure with a direct bandgap of $\sim 5\text{-}6$ eV which is too large to be used in regular electronic and optoelectronic applications [30]. Following BN, transition metal dichalcogenides (TMDs), another family of layered materials, such as MoS_2 , MoSe_2 , WS_2 and WSe_2 , have merged into the family of

2D materials. The bandgap of bulk TMDs is usually indirect, while it transits to direct bandgap when the layer number goes to monolayer [15]. Thus, the most advantageous property of monolayer TMDs comes from their intrinsic bandgaps ranging from ~ 0.4 to ~ 2.3 eV [31–35], which covers near infrared and most visible spectral range where most optoelectronic applications happen. For this reason, TMDs have been attracting tremendous interest of research in not only their fundamental nature such as optical and electrical properties but the applications of monolayer or few-layer TMDs based electronic and optoelectronic devices. In this work, we are only focusing on two TMDs: molybdenum disulfide (MoS_2) and tungsten disulfide (WS_2).

1.3.2.1 Molybdenum disulfide (MoS_2)

The crystal structure of MoS_2 has been studied for more than five decades [36]. As a layered structure similar to graphite, individual MoS_2 layers are stacking upon each to form the bulk through weak van der Waals force between layers. Each MoS_2 monolayer consists of a plane of molybdenum atoms sandwiched by two planes of sulfur atoms, and all the three plane are hexagonally arranged with the covalently bonded S-Mo-S atoms in a trigonal prismatic arrangement forming a hexagonal crystal structure, as shown in Figure 1.2. The thickness of each MoS_2 monolayer is about 0.65 nm. There are two commonly found crystal structures of MoS_2 : hexagonal (2H- MoS_2) and octahedral (1T- MoS_2) structures [37]. The former is semiconducting, while the latter is metallic. Theoretically, the former is more stable than the latter, out of which has been used to produce monolayer MoS_2 and intensively studied.

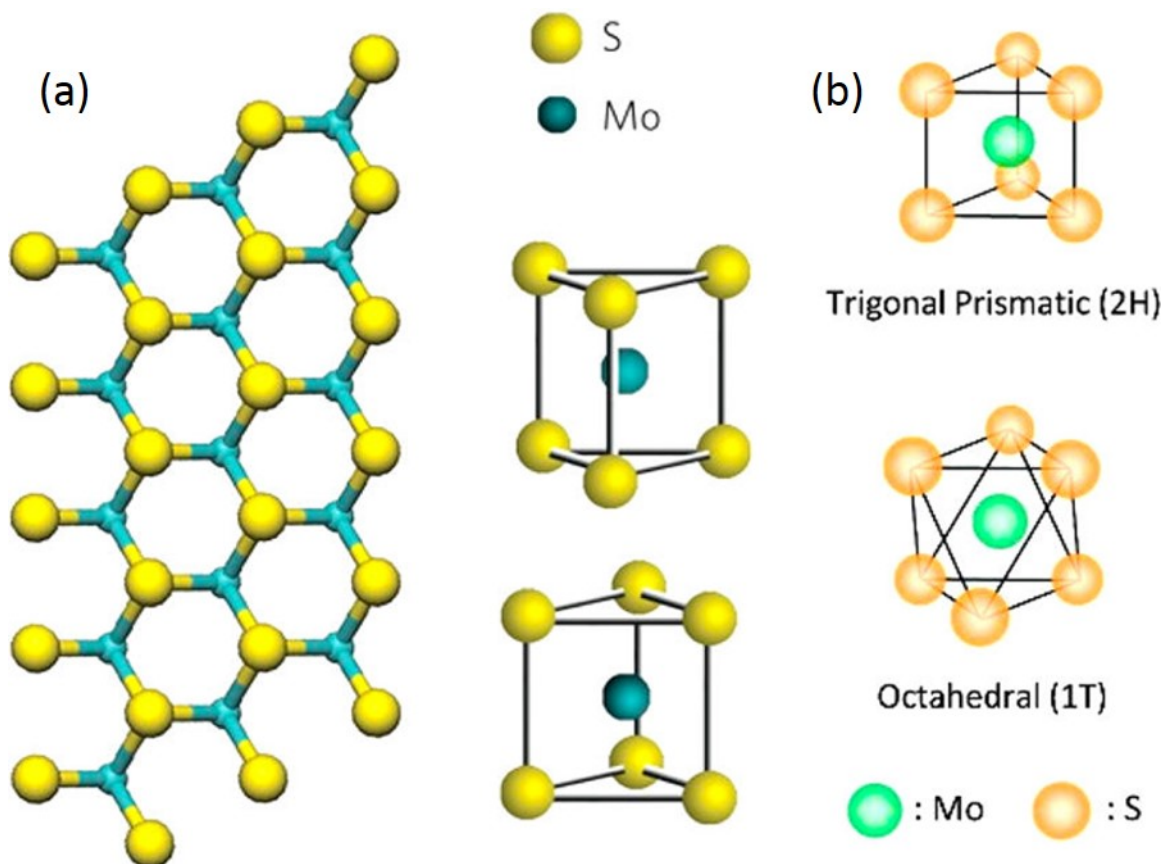


Figure 1.2: Crystal structure of MoS₂. (a) Top view of monolayer hexagonal crystal structure of MoS₂. (b) Two type of unit cell structures of MoS₂: Trigonal prismatic (2H) and Octahedral (1T). Panel (a) reproduced from H. Zeng et al. [38]. Panel (b) reproduced from G. Eda et al. [39].

Bulk MoS₂ has an indirect bandgap of 1.29 eV (Figure 1.3a) [?]. As the layer number decreases, the conduction band minimum moves upward, increasing the overall bandgap [40,41]. The states at K point in conduction band are mainly due to the d -orbitals of the molybdenum atoms which are barely affected by interlayer interactions, while the states at Γ point hybridization between p_z -orbitals of sulfur atom and the d -orbitals of molybdenum atoms that are affected drastically by interlayer interactions [42,43]. Therefore, the bands at Γ point are more sensitive to the decrease of layer number. Eventually in the monolayer, the indirect transition becomes larger than the direct transition at K point with a bandgap of ~ 1.9 eV [43], as shown in

Figure 1.3b. The direct transition of monolayer MoS₂ makes it a promising material that can be applied in field effect transistors (FETs) to achieve improved performance compared with graphene FETs, or can be used as a promising candidate for lower power electronics, such as photodetectors, due to their bandgaps in visible spectral range, shown in Figure 1.4. Top gated monolayer MoS₂ FETs showed an excellent on/off current ratio up to 108, a mobility of at least 200 cm²V⁻¹s⁻¹ at room temperature, and ultralow standby power dissipation (Figure 1.4a-c) [31]. Ultrasensitive photodetectors based on monolayer MoS₂ exhibited an external photoresponsivity of 880 A/W at a wavelength of 561 nm and a photoresponse in the range of 400-680 nm (Figure 1.3d-e) [44]. These results indicate great potential for applications in MoS₂-based integrated optoelectronic circuits, light sensing, biomedical imaging, video recording and spectroscopy.

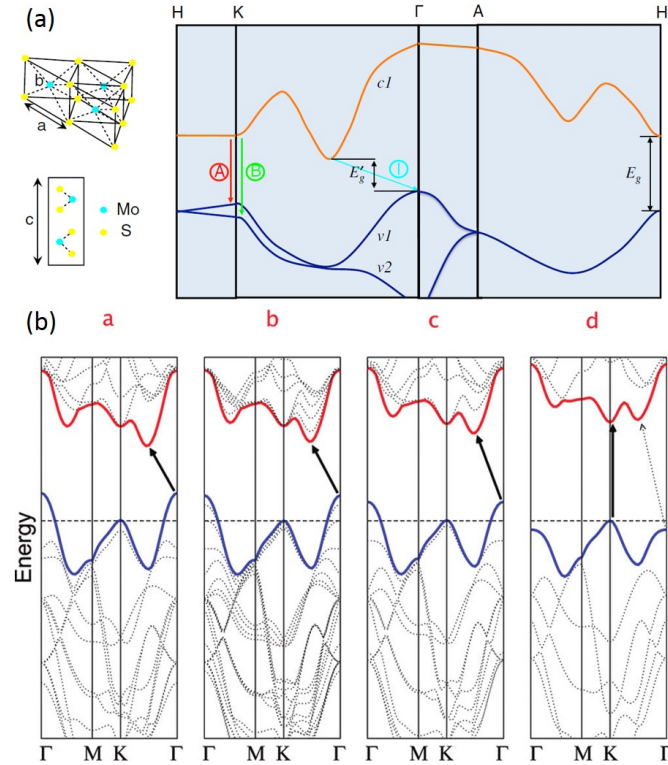


Figure 1.3: Band structure of bulk MoS₂. (a) The direct and indirect band gap, as well as the A and B excitons. (b) Transition of the band structure from indirect to direct band gap when the thickness of MoS₂ decreases (a-d). Panel (a) reproduced from Mak K. F. et al. [?]. Panel (b) reproduced from Splendiani A. et al. [43].

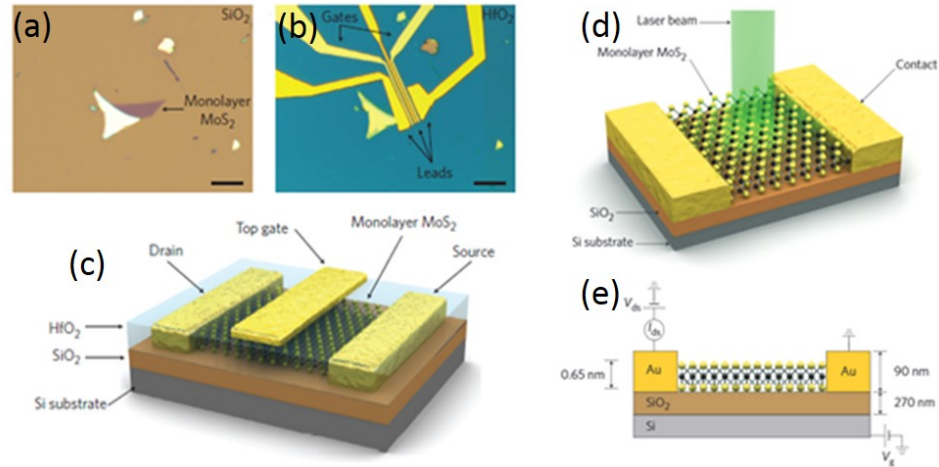


Figure 1.4: Single-layer MoS₂ devices: transistor and photodetector. (a) Optical image of a single layer of MoS₂ on SiO₂/Si substrate. (b) Optical image of a transistor based on the flake shown in a. (c) Three-dimensional schematic view of the transistor shown in b. (d)-(e) The schematic view of single-layer MoS₂ based photodetector. Panels a-c reproduced from Radisavljevic B. et al. [31]. Panels d and e reproduced from Lopez-Sanchez O. et al. [44].

Bulk MoS₂ belongs to the space group of D6h, while monolayer MoS₂ belongs to D3h space group. D6h possesses inversion symmetry, while D3h lacks [45]. In monolayer MoS₂, the lack of inversion symmetry combining with spin-orbit interaction breaks the spin degeneracy of the valence and conduction bands along the $\Gamma - K$ line, results in a band splitting of 148 meV at K point [46]. Thus, at K point of the Brillouin zone there are two direct transitions between conduction band and valence band, which are known as A and B excitons, respectively (Figure 1.5a) [47,48]. The energies corresponding to the two excitons are 1.85 eV (A exciton) and 2.00 eV (B exciton). The photoluminescence spectrum of monolayer MoS₂ is shown in Figure 1.5c, exhibiting two pronounced emissions at the A and B excitonic transitions [43].

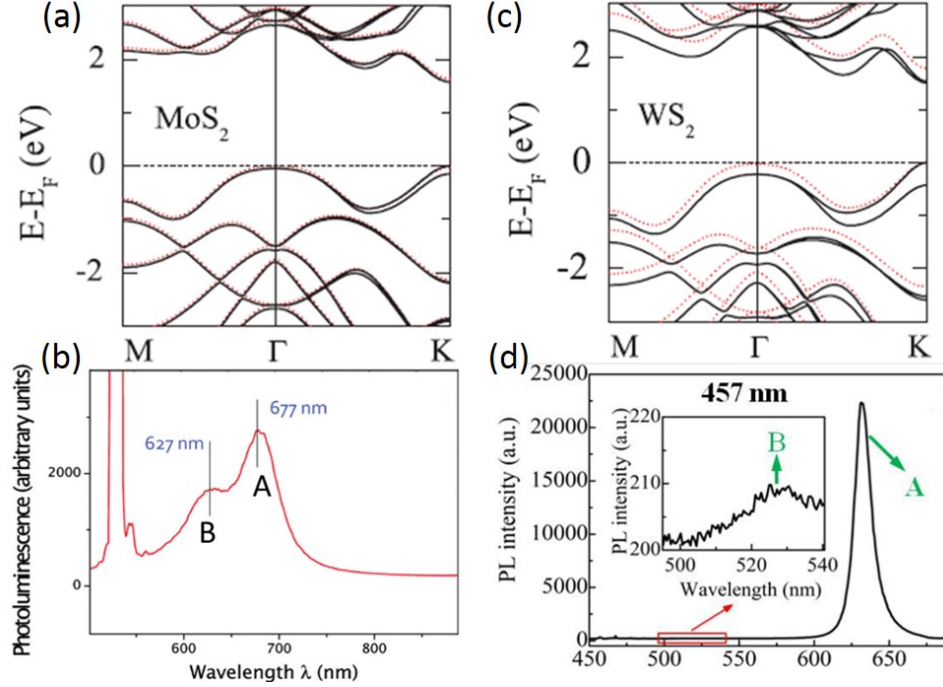


Figure 1.5: Electronic band structures and PL spectra of monolayer MoS₂ and WS₂. (a) and (c) The electronic band structures calculated for (a) MoS₂ and (c) WS₂ monolayer systems with (solid line) and without (dotted line) considering the spin-orbit interaction. (b) and (d) The PL spectra of monolayer (b) MoS₂ and (d) WS₂, showing both A and B excitons. Panels a and c reproduced from Zhu Z.Y. et al. [46]. Panel b reproduced from Splendiani A. et al. [43]. Panel d reproduced from Cong C. et al. [49].

On the other hand, MoS₂ possesses very high mechanical strength, showing a higher Young's modulus than that of steel. Its in-plane stiffness is ~ 180 N/m, corresponding to an effective Young's modulus of 270 GPa [50], compared to 2.4 TPa for graphene [51]. Though it might be argued that its mechanical property is not as exceptional as graphene, monolayer MoS₂ is still competent in the applications of flexible electronics and optoelectronics that requires a bandgap.

1.3.2.2 Tungsten disulfide (WS_2)

Bulk WS_2 is another representative of the family of TMD semiconductors, which has the same crystal structure as bulk MoS_2 that is belonging to D6h space group. Whereas, monolayer WS_2 belongs to D3h space group. According to optical measurements, monolayer WS_2 exhibits a strong photoluminescence at the direct bandgap transition of 2 eV, known as A excitonic transition (Figure 1.5d). Due to the strong spin-orbit coupling induced band splitting, another direct transition at K point has also been observed at the energy of 2.4 eV (i.e. B exciton). The valence band splitting for monolayer WS_2 is theoretically calculated to be 426 meV (Figure 1.5b), which is almost three times of that for monolayer MoS_2 (148 meV).

Based on theoretical prediction, among the semiconducting 2D TMDs WS_2 should have the highest mobility due to the reduced effective mass [52]. FETs based on monolayer WS_2 has been investigated to have a room temperature mobility of $\sim 50 \text{ cm}^2\text{V}^{-1}\text{s}^{-1}$ with an on/off ratio of 106 [53]. With long *in situ* annealing to improve the contact transparency and remove adsorbates, the mobility saturates below 83 K at $140 \text{ cm}^2\text{V}^{-1}\text{s}^{-1}$ for monolayer WS_2 and above $300 \text{ cm}^2\text{V}^{-1}\text{s}^{-1}$ for bi-layer one. Besides, with ionic liquid gated FET structures, the light emission from both mono- and bilayers of WS_2 has become a reality, though the quantum efficiency is low at this stage [32].

1.3.3 Black Phosphorus/Phosphorene

Black phosphorus (BP) or phosphorene has become a newer class of 2D layered materials, which is the most stable form among various phosphorus allotropies. Similar to graphite and TMDs, bulk BP consists of atomic monolayers, i.e., phosphorene, connected by weak interlayer bonding while within each individual layer the structure

is covalently bonded. Each phosphorus atom is covalently bonded to three phosphorus neighbors with one lone pair electrons left, forming a puckered honeycomb structure as shown in Figure 1.6a-b [54]. The space group of bulk BP is D2h; thus, BP or phosphorene has lower in-plane symmetry compared to graphite and TMDs, resulting in its unique in-plane anisotropic nature. Therefore, BP's optical, electrical, mechanical, thermoelectric, and other miscellaneous properties are expected to show angle dependence [54].

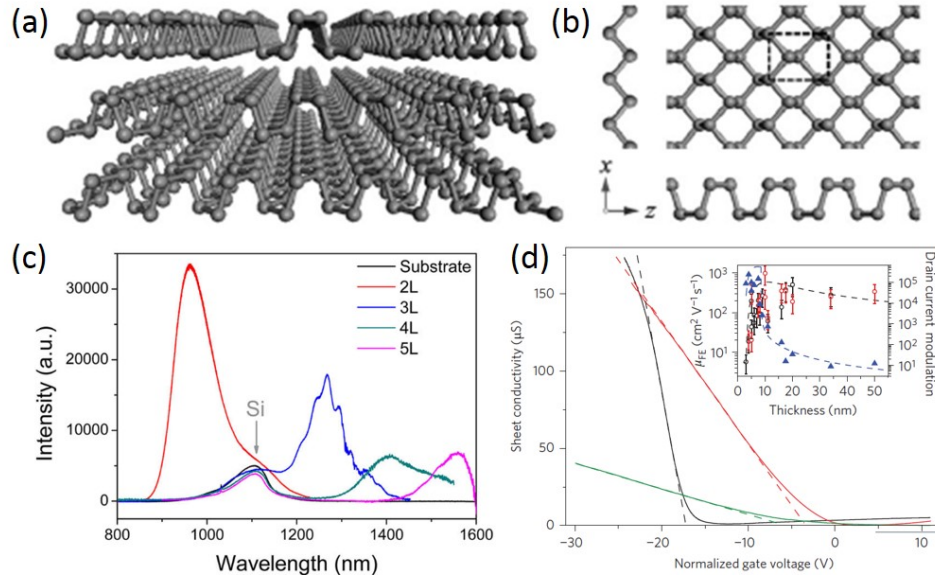


Figure 1.6: The lattice structure, PL spectra, and I-V characteristic of a few-layer phosphorene FET. (a) The puckered structure of a few-layer BP thin film. (b) Top view of monolayer BP. The zigzag and armchair directions are denoted as x and z axis, respectively. (c) PL spectra of two-, three-, four-, and five-layer phosphorenes. (d) Drain-source current I_{ds} as a function of bias V_{ds} at different gate voltages for a few-layer phosphorene FET on a SiO_2/Si substrate. Panels a and b reproduced from Wu J. et al. [54]. Panel c reproduced from Zhang S. et al. [55]. Panel d reproduced from Li L. et al. [17].

Unlike semiconducting TMDs having direct bandgap only in monolayer, BP possesses a layer-dependent direct bandgap ranging from 0.3 eV for the bulk to 1.5 eV for monolayer (Figure 1.6c), enabling the applications of BP for high-performance optoelectronic devices [55]. Few-layer BP based FETs has been shown to have re-

liable performance at room temperature with an on/off ration on the order of 10⁵ and a hole mobility more than $\sim 1,000 \text{ cm}^2\text{V}^{-1}\text{s}^{-1}$ (Figure 1.6d) [17]. Besides FET application, BP can also be used as photosensors and solar cells [56–59]. However, few layer BP is not air stable [60].

1.4 Fabrication of Layered Materials

A key component in nanotechnology is the production of the materials from which electronic/optoelectronic devices are made. These materials are usually required to be high perfection and high purity. The earliest growth techniques involved in growing bulk crystal from using one of the bulk crystal growth techniques: Czochralski, Bridgman, or float zone. These methods are appropriate for the synthesis of large-volume crystals to produce high purity, near perfect single crystal, but has no flexibility to control alloy composition or grow heterostructures. Whereas, epitaxial growth techniques have been specially developed for the synthesis of high-quality semiconductor alloys and heterostructures with precise controls, and normally single-crystal thin films are deposited on a substrate. These techniques include liquid phase epitaxy, vapor phase epitaxy, molecular beam epitaxy and metalorganic chemical vapor deposition. There are other thin-film deposition techniques that can be used for the deposition of polycrystalline semiconductors, including plasma-enhanced chemical vapor deposition, vacuum evaporation, and sputtering [61, 62].

For 2D materials their thicknesses are one or few atomic monolayers, which makes most of these growth techniques mentioned above infeasible to be used in the production of 2D materials. However, up to now, a large number of methods have been developed, which can be categorized into two major classes: bottom-up methods and top-down methods. The former involves the chemical reaction of molecules to form covalently linked 2D nanosheets, such as chemical vapor deposition (CVD). The latter

depends on the exfoliation of bulk layered materials, such as mechanical exfoliation (ME). Both methods can yield high-quality monolayers with a small number of defects that is suitable for applications of electronic/optoelectronic devices. Here, we mainly discuss two widely used techniques, i.e. mechanical exfoliation and CVD.

1.4.1 Mechanical Exfoliation

The birth of the first graphene is attributed to the mechanical exfoliation of HOPG (Highly Ordered Pyrolytic Graphite) in 2004. The general idea of this method is to exfoliate graphene layers from the bulk HOPG surface by applying normal and/or shear force with Scotch tape or tips of scanning probes [63–67]. The weak van der Waals attraction between graphene layers makes it possible to isolate single-layer graphene from the surface of the bulk. The procedure is shown in Figure 1.7. A small flake of graphite is placed on Scotch tape, and the tape is folded repeatedly over the graphite until it is coated with a relatively thin layer of graphite. Then the tape is pressed onto a silicon wafer coated with a 300-nm thick SiO_2 layer. In order to see the graphene optically, the thickness of SiO_2 layer is selected to be 90 nm or 285 nm to achieve the optimal optical contrast around 550 nm that results from interference effect. One may need to attempt numerous times of mechanical exfoliation, and on a good day, monolayer graphene with dimensions of tens of micrometers should be able to be obtained. This method has also been used to produce monolayer h-BN, TMDs and BP by many researchers, including myself.

Though very high-quality and large-size 2D materials can be produced with this method, it is extremely labor-intensive and time consuming, which makes it limited to laboratorial research and impossible for large-scale industrial production. For this reason, people developed other mechanical exfoliation methods, such as using sonication, ball milling, fluid dynamics, supercritical fluids, etc. [68].

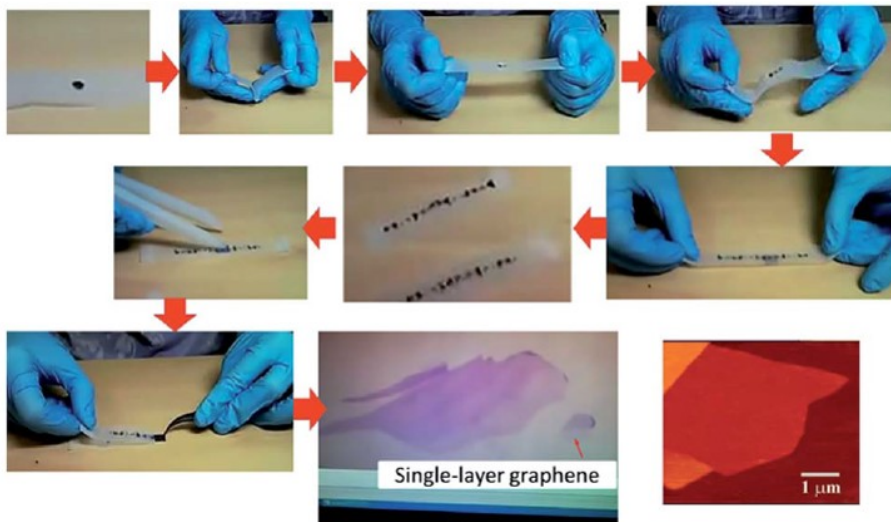


Figure 1.7: An illustration of the procedure of producing graphene from graphite by the technique of mechanical exfoliation with the scotch tape. Reproduced from Yi M. et al. [68].

1.4.2 Chemical Vapor Deposition

Within the bottom-up concept, the most widely used growth technique to synthesize 2D materials is chemical vapor deposition. In this process, desired materials are deposited onto the substrate surface after the reaction and/or decomposition of gaseous precursors. With precisely control, it is possible to grow high-quality and large-scale 2D materials for the high demand toward the implementation of these materials in industrial applications.

For the synthesis of graphene, people tried a variety of metal substrates such as Ni, Cu, Ru, Ir, Pt, Co, Pd, and Re, showing different carbon solubility and catalytic effect. During the CVD growth process, gas species are fed into the reactor and pass through the hot zone, and then the gaseous precursors decompose, leaving carbon particles at the surface of metal substrate and forming monolayer and few-layers graphene (Figure 1.8a). Among all these candidates of metal substrates, Ni has rel-

atively high carbon solubility at elevated temperatures; however, the percentage and size of monolayer graphene region are limited by the quality of Ni films. Whereas, graphene deposited on polycrystalline Cu, though Cu has ultralow carbon solubility, is uniform monolayer, which makes Cu a better substrate for monolayer graphene synthesis [67]. To facilitate graphene for electronic and photoelectronic applications, monolayer graphene on metal substrate needs to be transferred onto designated substrates. Figure 1.8b shows the schematic diagram of the transfer process by using a thin-layer of polymethyl methacrylate (PMMA) as the transfer medium. This technique has also been broadly used to transfer other CVD-grown 2D materials to arbitrary substrates.

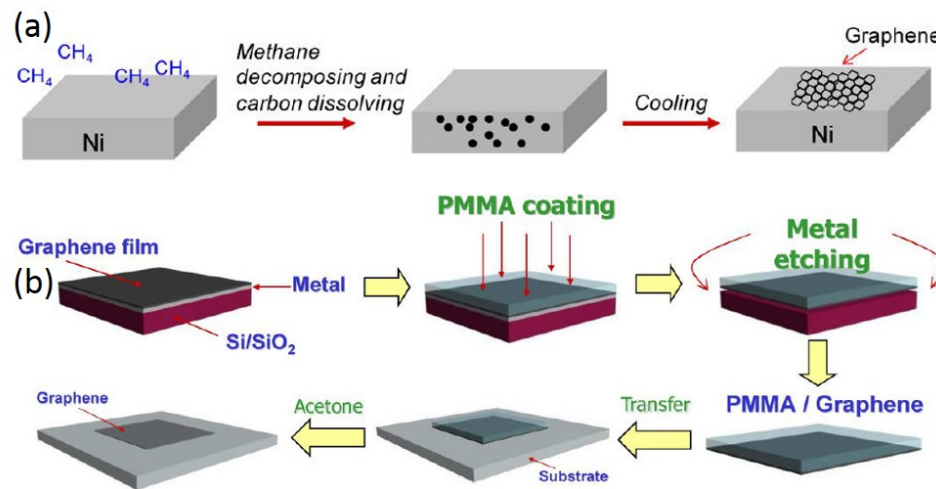


Figure 1.8: An illustration of the procedure of producing graphene from graphite by the technique of mechanical exfoliation with the scotch tape. Reproduced from Yi M. et al. [68].

The CVD growth process of TMDs is quite similar to that of graphene. Taking the growth of thin MoS₂ as an example, there are three ways corresponding to three precursors: ammonium thiomolybdate [(NH₄)₂MoS₄] solution [69], a thin deposition of elemental molybdenum [70, 71], or molybdenum trioxide [MoO₃] powder [72, 73], as shown in Figure 1.9. The substrates mostly used are SiO₂/Si and sapphire. In most cases, MoS₂ grown on sapphire substrates exhibited better quality and larger

grains than those grown on SiO_2 [36]. In addition, scattered single-crystalline MoS_2 triangles are initially grown, and then the triangle grains expand to join neighboring MoS_2 grains at the boundaries as the growth time increases. Eventually, complete MoS_2 films are formed. The synthesis of WS_2 is very similar to that of MoS_2 . Up to now no CVD synthesis of phosphorene has been reported yet. In all reported research on BP, the materials were obtained by the ME method.

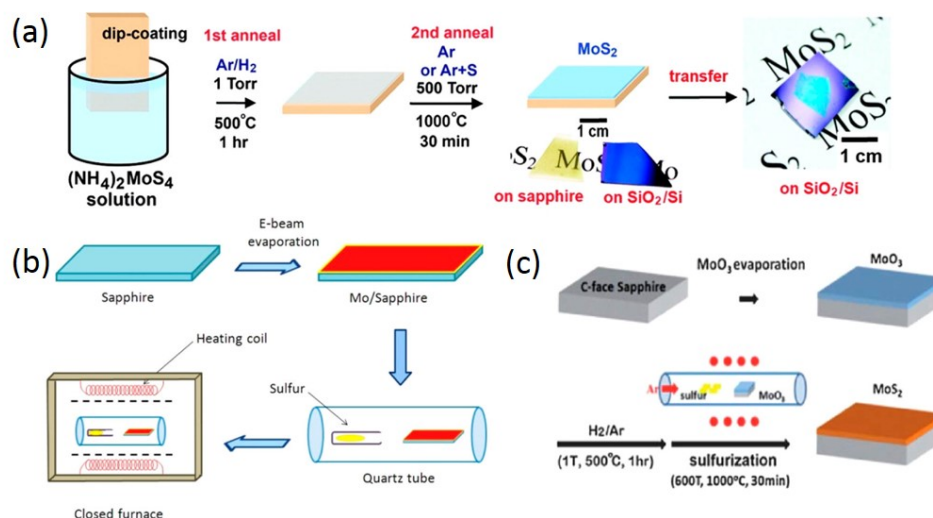


Figure 1.9: Growth techniques of MoS_2 monolayers. (a) MoS_2 growth on SiO_2/Si substrate using ammonium thiomolybdate. (b) Growth of MoS_2 directly from the sulfurization of elemental molybdenum. (c) Growth using molybdenum trioxide as the precursors. Panel a reproduced from Liu K. et al. [69]. Panel b reproduced from Laskar M. R. et al. [71]. Panel c reproduced from Lin Y. et al. [73].

1.5 Aims of Research

As Feynman predicted, materials of nanoscale must take into consideration of the surface tension and van der Waals force which would be significant to material properties. For 2D materials, they have a thickness of one or few atomic layers, less than 1 nm. Consequently, it is extremely susceptible for them to be influenced by surrounding environment, such as adsorbates at the surface and the interaction with substrates. In the preparation of 2D materials, the perturbations of fabrication process, such as

temperature, precursor ratios, etc., can be the origination of the changes of material properties. For instance, mechanical exfoliation may introduce polymer residues to the film as well as non-planar morphology, while CVD-grown films could have strong chemical bonding with substrate, i.e. strong interaction between the substrate and the films. Meanwhile, possible defects introduced to the films during fabrication, which may significantly modify the optical and electrical properties, should be taken into account.

Actually, all these influences in 2D materials can be interpreted as two major factors: (1) strain effect, and (2) doping or charge exchange effect. For instance, the defects, polymer residues and charge transfer from substrate are likely to change the charged carrier concentration or doping level in the film; whereas the non-planar morphology indicates non-uniform strain distribution over the film. As is well-known, Raman spectroscopy is a nondestructive technique, which has been widely used to characterize the structural and electronic properties of materials. It is very sensitive to the changes of strain and doping in the materials.

Therefore, the first aim of this research is to investigate the strain and doping effects of 2D materials as well as their interactions with substrate, and thus understand the intrinsic properties of the 2D material. In order to accomplish this, 2D films are prepared on different substrates by different fabrication techniques. By comparing the Raman results combining with PL spectroscopic results, we are able to distinguish the contributions of different effects in the changes of optical and electrical properties of 2D materials.

Besides, for any kind of material, the goal of studying is also application-oriented. Thus, it is also true for 2D materials that they can be applied in electronic/optoelectronic devices, particularly field effect transistors. However, because of the internal resistance, significant heat will be generated with bias applied, which consequently can

change the performance of the devices. With increasing temperature, the structural and electronic properties of the 2D materials used in devices can be modified. Since Raman spectroscopy can effectively determine the property changes, a temperature dependent Raman spectroscopy investigation on 2D materials can help us understand how self-heating changes the properties of materials and hence the performance of devices, which leads to the second aim of research that is to investigate the vibrational properties and electron-phonon coupling in 2D materials by using temperature dependent high temperature Raman spectroscopy. This study can further help us understand those effects mentioned in the first aim of research. Additionally, by combining temperature dependent Raman studies with laser power dependent Raman studies, we are able to extract thermal conductivity of 2D materials.

The final aim of this dissertation is to understand the electron-hole interaction of 2D materials. For instance, MoS₂ has a direct bandgap that is revealed by strong photoluminescence quantum yield. The photoluminescence involves in the recombination of electrons and holes. The recombination in 2D material are more complex than the bulk because it is more easily to be perturbed (either enhanced or quenched) by any slight change in the film internally or externally. PL spectroscopy and temperature dependent PL studies enable us to investigate the radiative and the non-radiative recombination of photo-generated carriers in 2D materials.

CHAPTER 2: TEMPERATURE DEPENDENCE OF RAMAN SCATTERING AND PHOTOLUMINESCENCE

2.1 Temperature Dependence of Raman Scattering

In this dissertation, temperature dependent Raman spectroscopy is the most used technique for investigating the structural and electronic properties of 2D materials as well as their changes with temperature, in particular in the elevated temperature region from room temperature up to the decomposition temperature of the material of interest. Raman spectroscopy is a spectroscopic technique based on Raman scattering or Raman effect. Before we move on to discuss temperature dependence of Raman scattering, we should review Raman scattering first.

2.1.1 Raman Scattering

Raman scattering, in a word, is the inelastic scattering of a photon. The phenomenon was first discovered by C. V. Raman and K. S. Krishnan in liquids [74], and by G. Landsberg and L. Mandelstam in crystals [75], among whom C. V. Raman was granted Nobel Prize in 1930. Unlike Rayleigh scattering where scattered photon have the same energy as the incident photon, Raman scattering results in scattered photon having a frequency different from that of the incident photon. The frequency difference between the incident photon and the scattered phonon through Raman scattering, observed by Raman spectroscopy, provides a fingerprint to identify and analyze molecules in chemistry, making it recognized as a landmark tool in chemistry history for analyzing

the composition of liquids, gases, and solids.

2.1.1.1 Raman Theory

According to classical treatment of Raman scattering [76, 77], the incident photons can be considered as an electromagnetic waver (usually laser beam) which is expressed as:

$$\mathbf{E}(\mathbf{r}, t) = \mathbf{E}_i(\mathbf{k}_i, \omega_i) \cos(\mathbf{k}_i \cdot \mathbf{r} - \omega_i t), \quad (2.1)$$

where $\mathbf{E}(\mathbf{r}, t)$ is the electric field strength, $\mathbf{E}_i(\mathbf{k}_i, \omega_i)$ the amplitude, \mathbf{k}_i the wavevector, and ω_i the frequency of the phonons. When the medium is irradiated by the wave/light, a sinusoidal polarization $\mathbf{P}(\mathbf{r}, t)$ will be induced:

$$\mathbf{P}(\mathbf{r}, t) = \mathbf{P}(\mathbf{k}_i, \omega_i) \cos(\mathbf{k}_i \cdot \mathbf{r} - \omega_i t) = \chi(\mathbf{k}_i, \omega_i) \mathbf{E}_i(\mathbf{k}_i, \omega_i) \cos(\mathbf{k}_i \cdot \mathbf{r} - \omega_i t). \quad (2.2)$$

Its frequency and wavevector are the same as those of the incident photons. If the medium is vibrating with a frequency of ω_m , the atomic displacement $\mathbf{Q}(\mathbf{r}, t)$ can be written as:

$$\mathbf{Q}(\mathbf{r}, t) = \mathbf{Q}(\mathbf{q}, \omega_m) \cos(\mathbf{q} \cdot \mathbf{r} - \omega_m t) \quad (2.3)$$

with wavevector \mathbf{q} . The normal modes of the molecule vibrations are called *phonons*. These atomic vibrations will modify χ , and it can be expressed as a function of \mathbf{Q} with a Taylor series:

$$\chi(\mathbf{k}_i, \omega_i, \mathbf{Q}) = \chi_0(\mathbf{k}_i, \omega_i) + (\partial\chi/\partial\mathbf{Q})_0 \mathbf{Q}(\mathbf{r}, t) + \dots, \quad (2.4)$$

where χ_0 denotes the electric susceptibility of the medium without fluctuations. The second and higher terms in Eq.(2.4) represents the oscillating susceptibilities induced by the lattice displacement $\mathbf{Q}(\mathbf{r}, t)$. Substituting Eq.(2.4) into Eq.(2.2), the polariza-

tion $\mathbf{P}(\mathbf{r}, t, \mathbf{Q})$ of the medium can be expressed as:

$$\mathbf{P}(\mathbf{r}, t, \mathbf{Q}) = \mathbf{P}_0(\mathbf{r}, t) + \mathbf{P}_{ind}(\mathbf{r}, t, \mathbf{Q}), \quad (2.5)$$

where

$$\mathbf{P}_0(\mathbf{r}, t) = \chi_0(\mathbf{k}_i, \omega_i) \mathbf{E}_i(\mathbf{k}_i, \omega_i) \cos(\mathbf{k}_i \cdot \mathbf{r} - \omega_i t) \quad (2.6)$$

is a polarization vibrating in phase with the incident photons and

$$\mathbf{P}_{ind}(\mathbf{r}, t, \mathbf{Q}) = (\partial\chi/\partial\mathbf{Q})_0 \mathbf{Q}(\mathbf{r}, t) \mathbf{E}_i(\mathbf{k}_i, \omega_i) \cos(\mathbf{k}_i \cdot \mathbf{r} - \omega_i t) \quad (2.7)$$

is a polarization wave induced by the phonon. To determine the frequency and wavevector of \mathbf{P}_{ind} the Eq.(2.7) can be rewritten as:

$$\begin{aligned} \mathbf{P}_{ind}(\mathbf{r}, t, \mathbf{Q}) &= (\partial\chi/\partial\mathbf{Q})_0 \mathbf{Q}(\mathbf{q}, \omega_m) \cos(\mathbf{q} \cdot \mathbf{r} - \omega_m t) \\ &\quad \times \mathbf{E}_i(\mathbf{k}_i, \omega_i) \cos(\mathbf{k}_i \cdot \mathbf{r} - \omega_i t) \end{aligned} \quad (2.8a)$$

$$\begin{aligned} &= \frac{1}{2} (\partial\chi/\partial\mathbf{Q})_0 \mathbf{Q}(\mathbf{q}, \omega_m) \mathbf{E}_i(\mathbf{k}_i, \omega_i) \\ &\quad \times \{ \cos[(\mathbf{k}_i + \mathbf{q}) \cdot \mathbf{r} - (\omega_i + \omega_m)t] \\ &\quad + \cos[(\mathbf{k}_i - \mathbf{q}) \cdot \mathbf{r} - (\omega_i - \omega_m)t] \}. \end{aligned} \quad (2.8b)$$

According to the classical theory, the \mathbf{P}_{ind} expressed in Eq.(2.8b) consists of two sinusoidal terms with the frequencies of $\omega_i - \omega_m$ and $\omega_i + \omega_m$, which are denoted as *Stokes* and *anti-Stokes* shifted waves, respectively. If $(\partial\chi/\partial\mathbf{Q})_0$ goes to zero, \mathbf{P}_{ind} is zero which indicates the vibration is not Raman-active. In other words, for a Raman-active vibration, the rate of polarizability change with the vibration must not be zero.

2.1.1.2 Raman Tensors and Selection Rules

Now that we understand the origin of Raman shift we will discuss the intensity of scattered radiation. The intensity of the scattered radiation, I_s , is related to the time-averaged power radiated by the induced polarizations \mathbf{P}_{ind} into unit solid angle, which can be expressed as [77]:

$$I_s \propto |\mathbf{e}_i \cdot \mathcal{R} \cdot \mathbf{e}_s|^2, \quad (2.9)$$

where \mathbf{e}_i and \mathbf{e}_s are the polarizations of the incident and scattered lights, and \mathcal{R} is known as the Raman tensor. By introducing a unit vector $\hat{\mathbf{Q}} = \mathbf{Q}/|\mathbf{Q}|$ parallel to the phonon displacement \mathcal{R} can be defined as:

$$\mathcal{R} = (\partial\chi/\partial\mathbf{Q})_0 \hat{\mathbf{Q}}(\omega_m) \quad (2.10)$$

In general \mathcal{R} is a complex second-rank tensor with components like χ , which can be obtained by a contraction of \mathbf{Q} and the derivative of χ with respect to \mathbf{Q} . The symmetry of the Raman tensor or the corresponding Raman-active mode can be deduced from measuring the dependence of the scattered intensity on the incident and scattered polarizations. On the other words, Raman scattering can be applied to determine both the frequency and symmetry of a zone-center phonon mode. The manipulation of the polarizations \mathbf{e}_i and \mathbf{e}_s and scattering geometries to switch on and off the vibrational modes is called Raman selection rules. For a Raman tensor, it is symmetric only when the difference in frequency between the incident and scattered light can be ignored. In practice, it is assumed to be symmetric because the laser frequency is much larger than phonon frequency. Usually non-symmetric components in the Raman tensor can be introduced only by magnetic fields [77].

2.1.2 Temperature Effect of Phonons

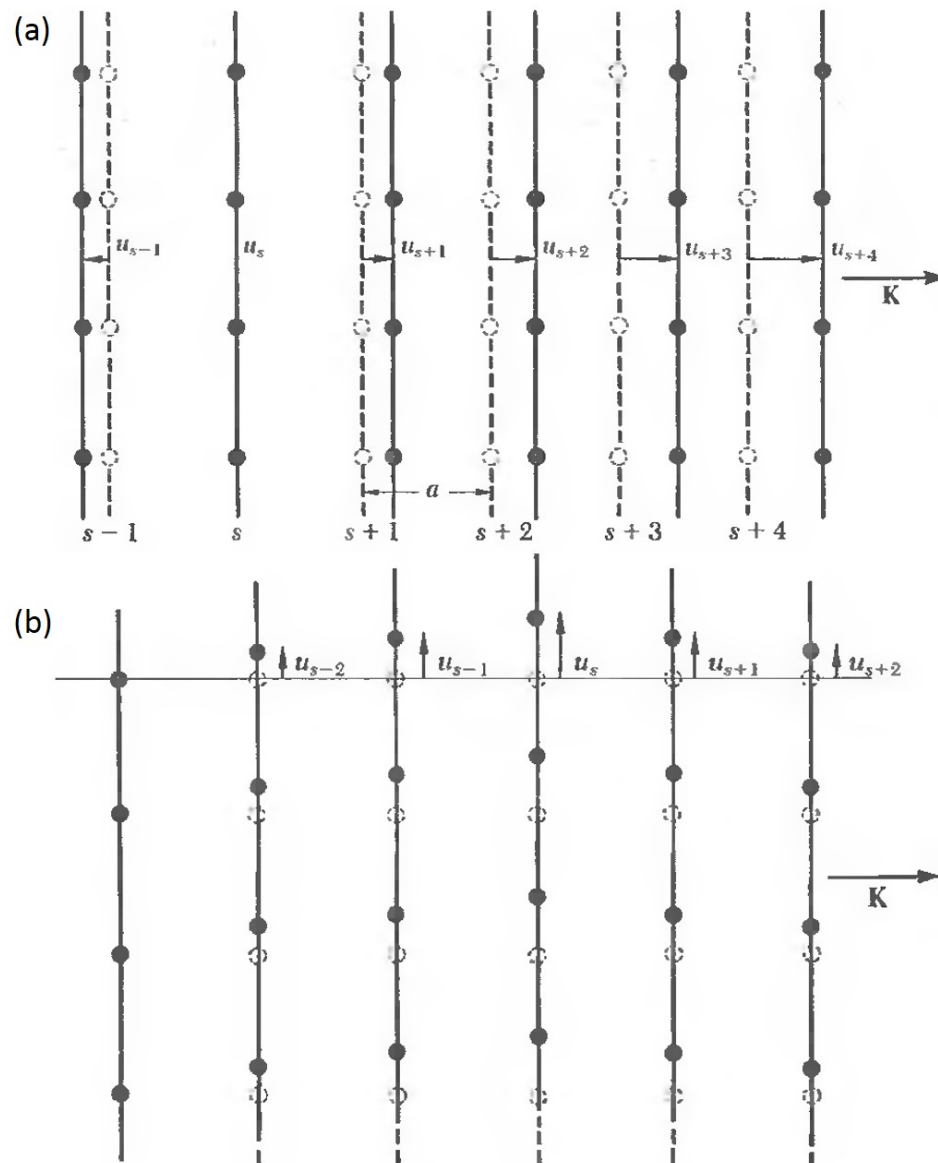


Figure 2.1: The displacement of planes of atoms. (a) Planes of atoms as displaced during passage of a longitudinal wave. (b) Planes of atoms when displaced as a longitudinal wave (solid lines). The dashed lines represents atoms in equilibrium. The coordinate u measures the displacement of the planes. Reproduced from Kittel C. [76].

Considering the elastic vibrations of a crystal with one atom in the primitive cell, the motion of each individual atom within a plane can be written as (Figure 2.1) [76]:

$$M \frac{d^2 u_s}{dt^2} = C(u_{s+1} + u_{s-1} - 2u_s), \quad (2.11)$$

where C is the force constant between nearest-neighbor planes and will differ for longitudinal and transverse waves, M is the mass of an atom, and u_s , u_{s+1} and u_{s-1} are the displacements of the plane s , $s + 1$ and $s - 1$, respectively. Assumptions are made that all the displacements have the same time dependence $\exp(-i\omega t)$ and that this differential equation has traveling wave solution, i.e.,

$$u_{s\pm 1} = u \cdot \exp(isKa) \exp(\pm iKa), \quad (2.12)$$

where a is the spacing between planes and K is the wavevector. Therefore, the dispersion relation between ω and K can be expressed as:

$$\omega^2 = (2C/M)(1 - \cos Ka). \quad (2.13)$$

Within the harmonic approximation, phonons have no interaction and an infinite lifetime. However, the main focus of this work is on the temperature dependence of Raman scattering. At very low temperatures, the thermal effect of lattice vibration can be described by a harmonic model, which is limited in the potential energy of terms quadratic in the interatomic displacements. However, as temperature goes up the harmonic theory would yield these consequences: (1) phonons do not decay or change with time; (2) there is no thermal expansion; (3) heat capacity becomes constant at high temperatures; (4) adiabatic and isothermal elastic constants are equal, and the elastic constants are independent of pressure and temperature [76]. In reality, none of these implications holds true. Therefore, the anharmonic (higher

than quadratic) terms in the interatomic displacements should be taken into account to correct the deficiencies of the harmonic theory. The change of phonon frequency and width with temperature is a manifestation of anharmonic effects in the lattice potential energy, which is the main focus of this work.

The change of phonon frequency with temperature ($\Delta\omega$) can be divided into two parts: (1) thermal expansion of the lattice ($\Delta\omega_E$), (2) anharmonic effect ($\Delta\omega_A$) which causes the change of phonon self-energy. Thus Raman shift can be written as [78,79]:

$$\Delta\omega(T) = \Delta\omega_E(T) + \Delta\omega_A(T), \quad (2.14)$$

where T is the crystal temperature. Although the first term, $\Delta\omega_E$, in Eq.(2.12) stands for the thermal expansion which occurs as a result of anharmonicity, it affects the harmonic frequencies through the change of force constant C , which may change with volume. Whereas, the second term is the purely anharmonic contribution to the shift, also known as the “self-energy” shift, which is only considered as a function of temperature T at constant volume.

Firstly, the contribution of thermal expansion to the shift of phonon frequency can be estimated by Grüneisen approximation, expressed as [78,80]:

$$\Delta\omega_E(T) = \omega_{T_0} \exp\left(-m\gamma \int_{T_0}^T \alpha \, dT\right) - \omega_{T_0}, \quad (2.15)$$

where ω_{T_0} is the phonon frequency at temperature T_0 ; m is the degeneracy, for cubic bulk crystal, m equals 3; γ is the Grüneisen parameter, and α is the thermal expansion coefficient of the crystal.

After separating out the contribution of the thermal expansion, the remaining change of phonon frequency is attributed to the pure temperature effects. These

effects are manifested as the higher terms of the interatomic displacement, which are correlated to an interaction of phonons. As a result, a phonon from a given state will decay into other phonons after a finite time. In a perturbation theory, the vibrational Hamiltonian can be written as [81]:

$$H = H_0 + H_A \quad (2.16)$$

where H_0 is the harmonic Hamiltonian, and H_A is the anharmonic Hamiltonian. H_A consists of the perturbation terms involving three, four, five, and more interacting phonons. As the simplest case, three-phonon interaction involves in decay of a phonon into two other phonons and vice-versa.

In thermal equilibrium, the phonon occupation number follows the Planck distribution function [76]:

$$\langle n \rangle = \frac{1}{\exp(\hbar\omega/\tau) - 1}, \quad (2.17)$$

where $\langle \dots \rangle$ denotes the average in thermal equilibrium, and $\tau = k_B T$ (k_B is Boltzmann constant). Normally, the change of phonon frequency arising from pure temperature effects can be derived from a semi-quantitative simple Klemens model [81, 82], which is expressed as:

$$\Delta\omega_A(T) = A \left(1 + \frac{2}{e^x - 1} \right) + B \left(1 + \frac{3}{e^y - 1} + \frac{3}{(e^y - 1)^2} \right) \quad (2.18a)$$

$$= A (1 + 2\langle n_1 \rangle) + B (1 + 3\langle n_2 \rangle + 3\langle n_2 \rangle^2), \quad (2.18b)$$

where $x = \hbar\omega/(2k_B T)$, $y = \hbar\omega/(3k_B T)$, and A and B coefficients are constants, representing contribution of three- and four-phonon processes to the change of phonon frequency, respectively. $\langle n_1 \rangle$ and $\langle n_2 \rangle$ are the occupation numbers of phonons with frequencies of $\omega/2$ and $\omega/3$. Here the assumptions are made that three-phonon process

involves in the decay of a phonon into two phonons with the same frequency of $\omega/2$, and four-phonon process into three phonons with the same frequency of $\omega/3$.

The anharmonicity arising from temperature effects also involves the damping of phonons, which is attributed to the decay of phonons as well. If only three- and four-phonon processes are taken into consideration, the damping constant $\Gamma(T)$ can be written as [81]:

$$\Gamma(T) = C \left(1 + \frac{2}{e^x - 1} \right) + D \left(1 + \frac{3}{e^y - 1} + \frac{3}{(e^y - 1)^2} \right) \quad (2.19a)$$

$$= C (1 + 2\langle n_1 \rangle) + D (1 + 3\langle n_2 \rangle + 3\langle n_2 \rangle^2), \quad (2.19b)$$

where C and D coefficients are constants. In Raman spectroscopy, the damping constant reflects the broadening of Raman peaks.

2.2 Temperature Dependence of photoluminescence

Besides Raman spectroscopy, in this dissertation photoluminescence spectroscopy was another useful technique to investigate the electronic structures of the 2D materials. It is a non-destructive method often used to analyze the electronic structure near the fundamental band gap, and light emission processes related to doping, and impurity levels of the crystal. Temperature dependent photoluminescence is often used to investigate radiative and non-radiative recombination process and exciton-phonon interactions in semiconductor materials.

2.2.1 Photoluminescence

Most of time, photoluminescence is the light emission after the absorption of excitation photons of energy ($\hbar\omega_{ex}$) higher than that of the band gap, and the energy

($\hbar\omega_{em}$) of radiated photons is lower than the excitation photons.

Photoluminescence can be divided into three stages, as indicated in Figure 2.2. First, the electrons in the valence band (ground states) are excited into the conduction band (excited states) by absorbing photons with energy of $\hbar\omega_{ex}$, creating electron-hole pairs. Second, the non-equilibrium electrons and holes tend to reach thermal equilibrium, which is caused by energy transfer to the crystal lattice, i.e., a step-by-step excitation of lattice vibrations. As a result, the electrons relax to the conduction band minimum (CBM) while the holes to the valence band maximum (VBM). Finally, the electron-hole pairs recombine through the emission of light whose energy is $\hbar\omega_{em}$. In high-quality semiconductors, the photoluminescence process discussed above is the typical transition which occurs at the band edge, which is dominated by radiative annihilation of electron-hole pairs (excitons) producing the so-called free exciton peak.

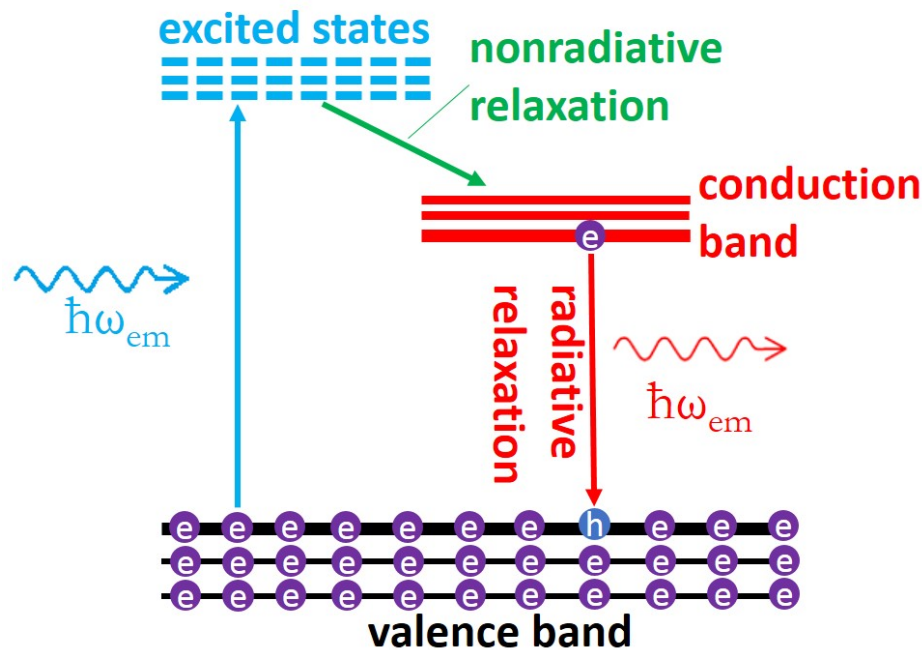


Figure 2.2: Sketch of the basic processes involved in a typical photoluminescence of semiconductors.

However, quite often a semiconductor contains various impurity and defect states within the fundamental bandgap, of which some are shallow, i.e., close to the band edges, and some are deep, i.e., away from the band edges. Such impurities or defects usually play the roles of donors or acceptors. Under equilibrium conditions, some of the electrons from the donors will be captured by the acceptors, resulting in donor (D^+) and acceptor (A^-) states. By optical excitation, electrons and holes that created in the conduction and valence bands, respectively, will then be captured by D^+ and A^- states to produce neutral D_0 and A_0 centers. Some of the electrons on the neutral donors will recombine radiatively with holes on the neutral acceptors. The process is known as a donor-acceptor pair transition. Meanwhile, the excitons may also be attracted to impurities such as donors or acceptors to form bound excitons at low temperature. This attraction lowers the exciton energy, hence the energy of radiated photons is lower than that of the band-edge free-exciton transition. The recombination of an exciton bound to a neutral donor atom is usually denoted by D_0X , while that to a neutral acceptor A_0X . Excitons can also bind to ionized impurities, form bound excitons denoted as D^+X or A^-X . These complex, known as trions, can be considered as charged excitons, which are abbreviated as X^+ (positively charged) and X^- (negatively charged) [77].

2.2.2 Temperature Dependence of Photoluminescence

The PL emission spectra usually show a characteristic temperature dependence. As the temperature increases, the emission energy usually shifts to a lower energy, the emission band broadens, and at high temperatures the emission is quenched. Temperature dependent PL spectroscopy is often used to investigate the radiative and non-radiative recombination processes and exciton-phonon interaction in semiconductor materials. In general, the thermal quenching in PL intensity with increasing

temperature is attributed to the thermal activation of nonradiative recombination processes.

A widely used relation for the variation of the energy gap (E_g) with temperature (T) in semiconductor materials is the so-called Varshni relation that is given as [83]:

$$E_g = E_0 - \frac{\alpha T^2}{T + \beta}, \quad (2.20)$$

where E_0 is the band gap at $T = 0$ K, and α and β are constants. The variation of the energy gap with temperature is believed to stem from two mechanisms: (1) A shift in the relative position of the conduction and valence bands due to the temperature-induced change of the lattice; (2) The major contribution comes from a shift of the energy gap due to a temperature-dependent electron lattice interaction.

A simple Arrhenius formula, as given below, is often used to describe the temperature induced quench in PL intensity. It is valid when only one simple thermal quench mechanism is involved and no other mechanisms that may transfer or deplete the carriers to or from the state of interest [84, 85]. The Arrhenius formula can be written as [86]:

$$I(T) = \frac{I_0}{1 + A \exp(-E_a/k_B T)}, \quad (2.21)$$

where $I(T)$ represents the integrated PL intensity, E_a is the activation energy of the thermal quenching process, k_B is the Boltzmann constant, I_0 is the integrated intensity at $T = 0$ K, and A is a pre-factor related to the density of non-radiative recombination centers of the quenching process.

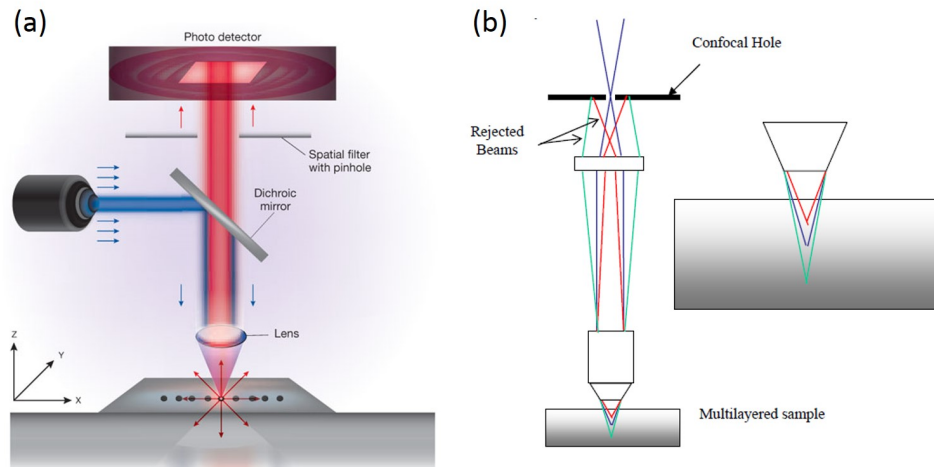


Figure 2.3: Confocal microscope. (a) A simplified view of confocal microscope. (b) The schematic of the confocality. Panel a reproduced from Nwaneshiudu A., et al. [87].

2.3 Experimental Setups

In recent years, the confocal microscope has been widely used as a research instrument to measure Raman and fluorescence in physics, material science, biology, and medicine fields. In comparison with conventional non-confocal microscopy, confocal microscopy is an optical technique to increase the optical resolution and contrast by adding a pinhole at the confocal plane [88], as shown in Figure 2.3a. For a conventional non-confocal microscope, due to diffraction effect the maximum resolution is proportional to the size of its objective, and inversely proportional to the wavelength of the light being observed. Thus, the microscope is said to be diffraction limited. As a result of diffraction, the pattern observed in the image shows a bright region in the center accompanied by a series of concentric rings of decreasing intensity around it, which is called the Airy disc. The diameter of the Airy disc can be written as:

$$d = \frac{1.22\lambda}{NA}, \quad (2.22)$$

where λ is the wavelength of light being observed and NA is numerical aperture of the objective being used.

However, the confocal microscope can increase the resolution beyond the diffraction limit. As shown in Figure 2.3a, the incident light (usually laser) is focused through the objective on the sample examined, and the same objective collects the light coming back from the sample, such as reflected light, Raman or photoluminescence. In conventional microscopy, some of the light scatters which could blur or obscure the image. Confocal microscopy overcomes this problem using a small pinhole aperture, allowing the pass of only the light emitting from the desired focal spot. Any light outside the pinhole is blocked (Figure 2.3b). In the very original design of confocal system [89], the pinhole is placed at the confocal plane of microscope system; however, in the case of Figure 2.3a it is placed in a conjugate focal plane as the focal plane on the sample. The light passing through the pinhole is finally collected by a sensitive light detector, such as charge-coupled device (CCD) or photomultiplier tube (PMT).

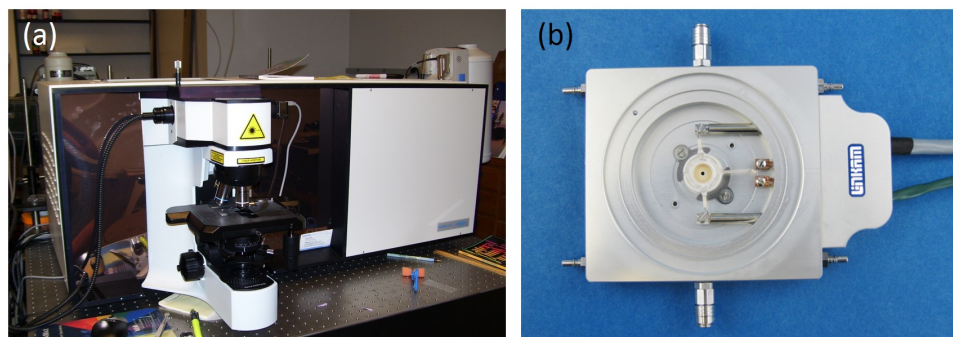


Figure 2.4: Experimental setups. The views of (a) Horiba LabRAM HR800 micro-Raman/PL spectroscopy, and (b) Linkam TS1500 heating stage.

Therefore, the advantages of using confocal microscopy are as below: (1) the increase of axial resolution as well as lateral resolution; (2) the improvement of image contrast; (3) capability to reconstruct 3D images. Given all these advantages of

confocal microscope, the works related to optical spectroscopies in this dissertation were mostly carried out with a confocal system – Horiba LabRAM HR800. With the confocal configuration, the spatial resolution can be achieved beyond the diffraction limit. Meanwhile, with a long focal length of spectrometer (800 *cm*) allows the tool to achieve a high spectral resolution. For instance, with a grating of 1200 groove/mm and a CCD of 2048-pixel array, the spectral resolution of the system is $\sim 0.5 \text{ cm}^{-1}$ when 532 *nm* laser is used. With a 2400 groove/mm grating, the resolution can be even better. Another advantage of this tool is the ability of scanning the sample with a precisely-controlled sample stage, which allows us to perform a mapping of Raman or PL at a designated area to examine the variation of a specific optical characteristic. Besides this confocal system, all the temperature-dependent measurements were performed with a heating system – Linkam TS1500. This system has a temperature control accuracy of less than 1 °C, and allows us to purge gases into the chamber or even to create a vacuum environment. In Figure 2.4 shows the appearance of these two instruments.

CHAPTER 3: TEMPERATURE DEPENDENCE OF RAMAN SCATTERING IN GRAPHENE

3.1 Fabrication and Characterization of Graphene

3.1.1 Fabrication of Graphene

Graphene, as a single layer of graphite, can be fabricated by either mechanical exfoliation or chemical vapor deposition. For mechanical exfoliation, the graphene is usually transferred to silicon substrate coated with a 300 *nm* SiO₂ thermal layer, with which graphene can be observed under optical microscope [10, 90]. For CVD growth, the graphene films are typically synthesized on Cu or Ni, and then transferred to SiO₂/Si substrate. During the transferring process, scotch tape is utilized for mechanically exfoliated (ME) graphene and PMMA for CVD grown films, thus it is quite possible that polymer residues from the tape and PMMA will be remained on top of the graphene films, which are difficult to be fully removed either by solvents like methanol or by annealing. Figure 3.1 shows the optical images of two graphene samples fabricated by these two methods. Especially for the CVD sample, polymer residues can be clearly observed. Besides the two samples fabricated with these two methods, the optical image of graphite, which is used for exfoliation and as reference, is also shown in Figure 3.1.

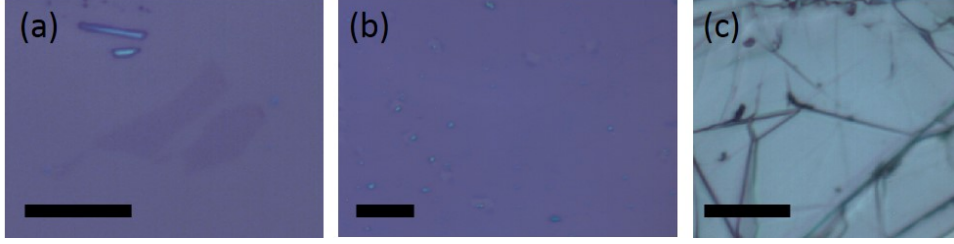


Figure 3.1: Optical images of graphene samples and graphite. (a) ME graphene on SiO_2/Si by the scotch tape technique. (b) CVD-grown graphene transferred onto SiO_2/Si by PMMA. (c) Graphite. The scale bar is $10 \mu\text{m}$.

3.1.2 Characterization of Graphene Samples

Atomic force microscopy (AFM) is perhaps in general the most reliable method to identify single- and few-layer 2D materials, but for graphene it has limitations. The thickness of graphene has been theoretically predicted to be of $\sim 0.35 \text{ nm}$. However, due to the chemical contrast between graphene and the substrate, which results in a chemical thickness of $0.5\text{-}1 \text{ nm}$ (much bigger than the interlayer graphite spacing), the identification of single layer graphene is a great challenge with AFM. Therefore, seeking for a more reliable method to determine the layer number of exfoliate graphene layers is necessary for the widespread utilization of this material. As it has been demonstrated, the graphene's electronic structure can be uniquely reflected in its Raman spectrum, which reveals the changes in the electronic band structure for single layer, bilayers, and few layers [91]. Therefore, Raman spectroscopy can be used as fingerprints to nondestructively identify the thickness (layer number) of graphene layers.

Bulk graphite belongs to the space group of $P63/mmc$ ($D6h4$); its isogonal point group is $D6h$. The irreducible representations of graphite vibration modes at Brillouin zone center are: $\Gamma^{\text{graphite}} = 2A_{2u} + 2B_{2g} + 2E_{1u} + 2E_{2g}$ [92,93]. Among them, there are two Raman active vibrations at the Γ point of the Brillouin zone: $E_{2g(2)} \approx 1582 \text{ cm}^{-1}$

and $E_{2g(1)} \approx 42 \text{ cm}^{-1}$. For single graphene layer, there are two atoms per unit cell, giving six normal modes for the zone center. The irreducible representations for the zone-center modes of graphene are: $\Gamma^{\text{graphite}} = A_{2u} + B_{2g} + E_{1u} + E_{2g}$ [94]. The A_{2u} mode represents translation perpendicular to the graphene plane and the E_{1u} the translation in the graphene plane. The B_{2g} mode is an inactive optical phonon mode of which the carbon atoms vibrate perpendicularly to the graphene plane. The E_{2g} mode is doubly degenerate in-plane optical vibration, which is the only Raman active mode for graphene at the zone center. The frequency of the E_{2g} mode is expected at $\sim 1587 \text{ cm}^{-1}$ [91]. In the literature, the graphite $E_{2g(2)}$ mode is usually assigned as the G peak, which is carried over to single or few-layers graphene. If the number of layers increases from graphene to graphite, the peak position of G band tends to decrease from 1587 cm^{-1} to 1581.5 cm^{-1} while its intensity increases linearly from monolayer to 20-layers [95].

If graphite sample contains disorder in its crystalline structure, a new Raman line appears at $\sim 1370 \text{ cm}^{-1}$. It is assigned as disorder-induced mode, or D-mode. Conventionally, this mode stands for the vibration related to the K point of graphite Brillouin zone. Its frequency is also close to that of the Γ point optical phonon in diamond. In the second-order spectrum of graphite there is one main feature at $\sim 2700 \text{ cm}^{-1}$, historically denoted as D* or G' or 2D mode. The frequency of this mode is very close to twice that of D mode. The notation of 2D is used in this dissertation. The frequency of the D mode shifts to higher frequency with increasing excitation energy, and the 2D band shifts twice as much as the D band, confirming the 2D mode is an overtone of the D mode [92, 96]. This is due to double resonance process that links the phonon wave vectors to the electronic band structure. This process predicts that graphene has a single 2D peak. As number of layers increases, 2D band becomes more complicate, showing more features. Besides G, D and 2D peaks, there are also vibrational modes at $\sim 2450 \text{ cm}^{-1}$ and $\sim 3248 \text{ cm}^{-1}$.

Figure 3.2 shows the Raman spectra of the three samples shown in Figure 3.1, measured by 532 nm excitation laser. All the major peaks discussed above are observed in these spectra. The D peak, 1345 cm^{-1} , is only seen in CVD-grown sample, because it contains more defects which are from both growth and transfer processes. Besides D peak, a peak at 1620 cm^{-1} is observed which is denoted as D' [97]. In CVD-grown sample, both D and D' bands are activated by a single-phonon intervalley and intravalley scattering process through defects, respectively. The defects provide the missing momentum to satisfy momentum conservation in the Raman scattering [98, 99]. No D-band feature is observed in both mechanically exfoliated graphene and graphite, indicating they are of high quality or nearly defect-free. The two most intense features are the G peak and 2D peak. The G peak is due to the doubly degenerate zone center E_{2g} mode; whereas, the 2D band is the second order of zone-boundary phonons near K point, having the frequency of twice of the D band. For G peaks, the frequency is measured to be 1587.6 cm^{-1} for CVD-grown graphene, 1584.5 cm^{-1} for ME graphene, and 1581.5 cm^{-1} for graphite. The frequency of G band increases as the thickness decreases. For graphene the peak position of G band is very sensitive to doping effect [100]. Since the CVD-grown graphene has more adsorbed polymeric residues on top of the film than the ME sample, more doping could be introduced to the graphene layer causing a blueshift of G band. The full width at half maximum (FWHM) of the three samples are 18.8 cm^{-1} (CVD), 11.2 cm^{-1} (ME), and 15.0 cm^{-1} (graphite), respectively. The larger FWHM of CVD-grown graphene is due to its lower crystalline quality, such as defects and non-uniformity, which can significantly affect the crystal structure.

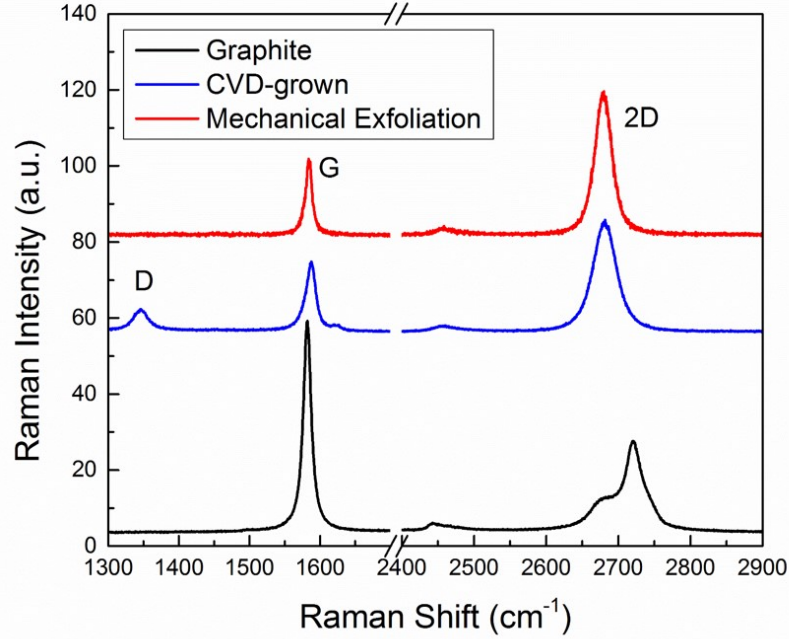


Figure 3.2: The Raman spectra of graphene and graphite.

As of 2D peak, both CVD-grown and ME graphene samples exhibit single symmetric peak at 2680.7 and 2679.6 cm^{-1} , respectively. However, graphite shows a clear doublet feature. The 2D peak in graphene is due to two phonons with opposite momentum in the highest optical branch near the K point, which is called double resonance (DR) process. The DR process links the phonon wave vectors to the electronic band structure. Within DR, Raman scattering is a process of fourth order involving four virtual transitions (as shown in Figure 3.3) [91]: (1) a laser induced excitation of an electron-hole pair indicated as $a \rightarrow b$ vertical transition; (2) electron-phonon scattering with an exchanged momentum q close to K ($b \rightarrow c$); (3) electron-phonon scattering with an exchanged momentum $-q$ ($c \rightarrow b$); (4) electron-hole recombination ($b \rightarrow a$). Thus, the DR condition is reached while the energy is conserved in these transitions. In single layer graphene only a single peak is observed that is corresponding to the phonon satisfying DR conditions with momentum $q > K$,

along the $\Gamma - K - M$ direction, whereas the other two possible DR phonons, with $q < K$ and $q \sim K$, give a much smaller contribution to the Raman intensity. As the layer number increases to 2 or more, more components within the 2D peak appear, which in principle is attributed to the splitting of the electronic bands rather than the splitting of the phonon branches. Because the splitting of the phonon branches theoretically calculated is much smaller than experimentally observed splitting of 2D Raman peak [91]. Thus, the doublet feature of 2D band is solely due to the splitting of electronic band structure. By fitting the 2D band of graphite with Lorentzian function, the frequencies of the two components, denoted as $2D_1$ and $2D_2$, are 2677.1 and 2721.8 cm^{-1} , respectively, and the splitting is 34.7 cm^{-1} .

Figures 3.4 and 3.5 show Raman mapping results of both ME and CVD-grown graphene samples, respectively. For ME graphene sample, both G and D intensity maps (Figure 3.4a,d) exhibit uniform distribution, except for the edge where the measured area of graphene is smaller than laser spot. The peak position variation of both bands is less than 1 cm^{-1} , so is the FWHM variation. All these data indicate that the ME graphene has an extremely high quality. It is worth noting that at the edge D peak is observed because the edge of the graphene flake is considered as defective. The uniformity of the mapping results of the ME sample suggests that the sample is free from the possible chemical contamination of the transfer process. Whereas, the mapping results of CVD-grown graphene is shown in Figure 3.5, revealing non-uniform distributions of peak position, intensity and FWHM. The maximum variations of G and 2D peak positions are 5.7 and 11.8 cm^{-1} , respectively. The extraordinarily large variation of the CVD-grown graphene is attributed to the defects in the film as well as the rippling introduced during transfer, showing a clear D peak feature as indicated in Figure 3.2.

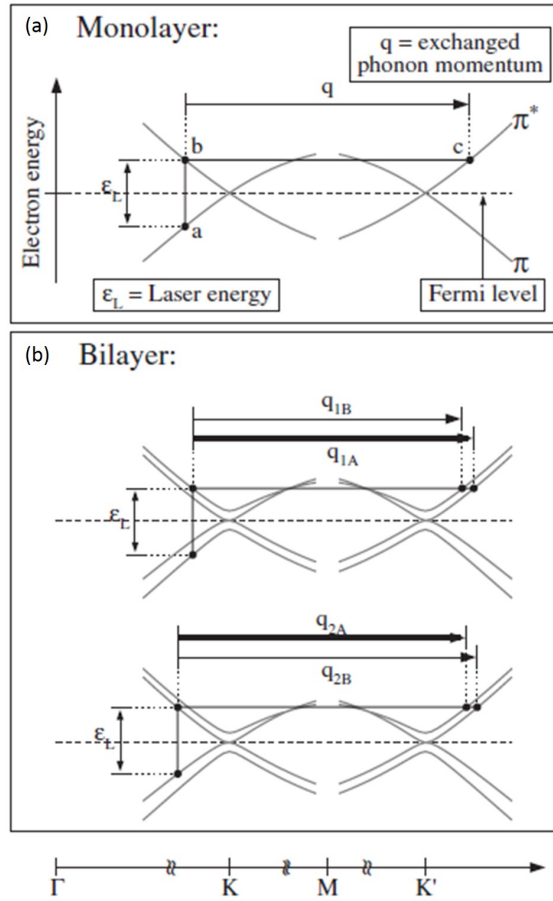


Figure 3.3: Double resonance for the 2D peak in (a) monolayer and (b) bilayer. Reproduced from Ferrari A. C. et al. [91].

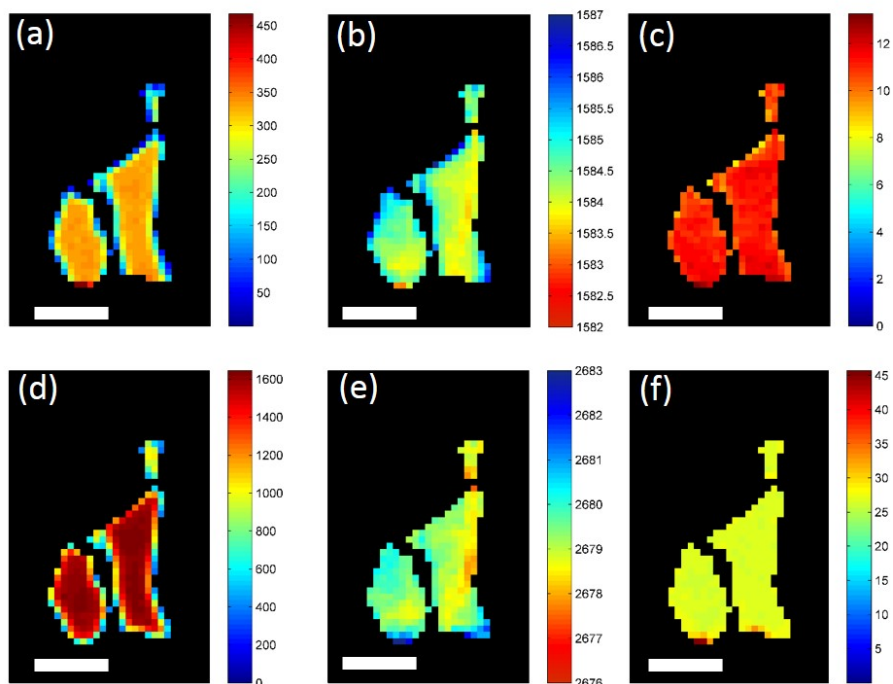


Figure 3.4: G and 2D band Raman mapping results of ME graphene sample. (a) and (d) The intensity maps of (a) G band and (d) 2D band. (b) and (e) The maps of Raman peak frequencies of (b) G band and (e) 2D band. (c) and (f) The maps of FWHM of (c) G band and (f) 2D band.

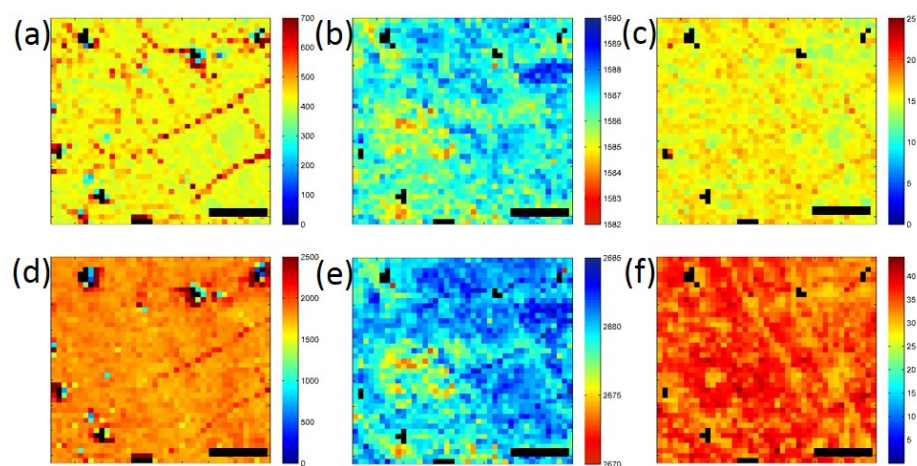


Figure 3.5: G and 2D band Raman mapping results of CVD-grown graphene sample. (a) and (d) The intensity maps of (a) G band and (d) 2D band. (b) and (e) The maps of Raman peak frequencies of (b) G band and (e) 2D band. (c) and (f) The maps of FWHM of (c) G band and (f) 2D band.

3.2 Temperature Dependent Measurements and Results

Like graphite, graphene is chemically inert in most case as well as good thermal stability up to several hundred °C without severe degradation. However, thermal treatment can cause graphene non-negligible changes in its material properties. As the annealing temperature goes up, graphene films that are held by SiO₂/Si substrate, as an example, undergoes in-plane compression and rippling due to conformal adhesion or thermal expansion difference between graphene and substrate. The annealing process can significantly change the structural and electronic properties of graphene, resulting in the charge carrier mobility of annealed graphene devices much lower than that of pristine devices [101]. Usually, the graphene samples are prepared by tapes or CVD. The polymeric adhesive residues are difficult to be removed completely even by annealing at high temperature.

There were a few temperature dependent Raman studies on graphene with the intent to obtain the temperature coefficients of the graphene Raman modes [102,103]. These studies were performed in a temperature region (typically below 200 °C) where the Raman frequency shifts appeared to be more or less linear. We have instead to investigate the temperature effects to much higher temperatures, to the limit of the material thermal degradation occurs. Raman spectroscopy in a broader temperature range can help to understand the influence of the residues and the changing 2D material/substrate bonding on the properties of graphene.

Temperature dependent Raman of all the three samples is performed in the range from room temperature to 400 °C for graphene samples and to 500 °C for graphite in a N₂-purged heating chamber. The laser excitation line is 532 nm with the power of ~1 mW. The temperature dependences of both G and 2D band frequencies are shown in Figure 3.6. For graphite, since 2D peak contains two components, Lorentzian

fitting has been applied to extract the individual temperature dependence of $2D_1$ and $2D_2$. Figure 3.7 shows the representative spectra of graphene samples and graphite at different temperatures.

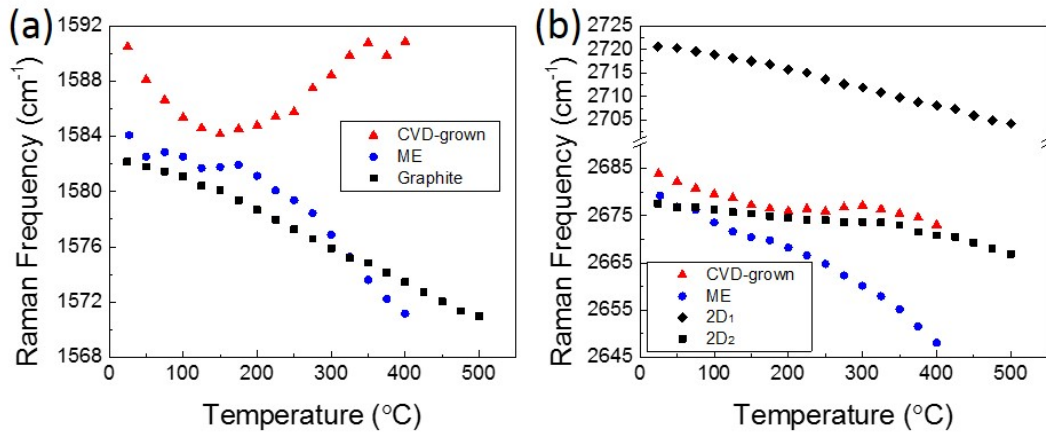


Figure 3.6: Temperature dependence of Raman frequencies of (a) G and (b) 2D bands for the two graphene samples and graphite.

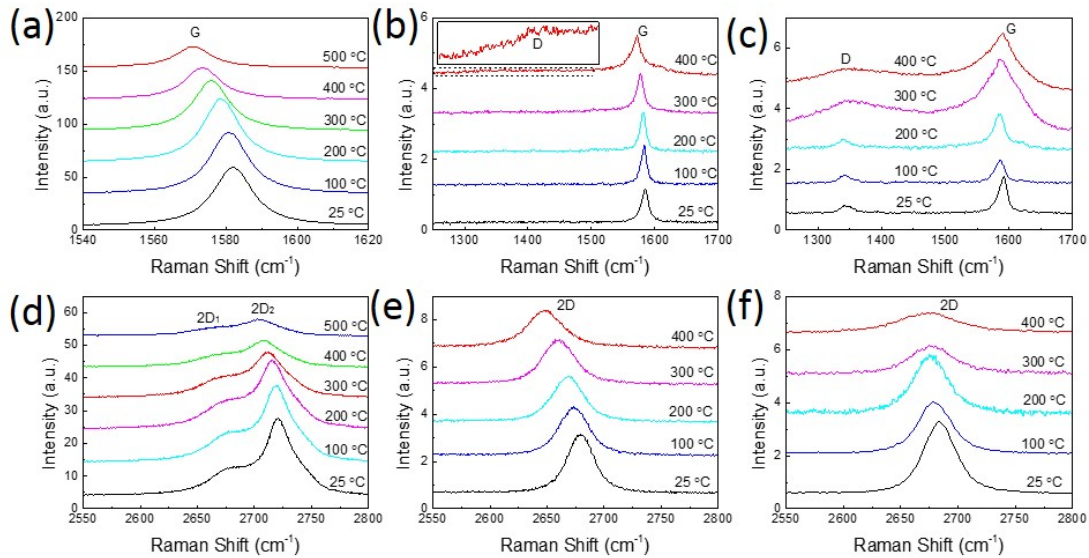


Figure 3.7: The representative Raman spectra at different temperatures for the two graphene samples and graphite. (a)-(c) G band spectra. (d)-(f) 2D band spectra.

Graphite, as the reference, exhibits more linear temperature dependence than the other two graphene samples. Empirically, the temperature dependence of Raman

shift is often described as:

$$\omega(T) = \omega_0 + \chi\Delta T, \quad (3.1)$$

where ω_0 is the frequency at RT, χ is the temperature coefficient, and ΔT is the temperature change relative to RT. Fitting the dependence with Eq.(3.1), the temperature coefficients are -0.025, -0.020, and -0.036 cm^{-1}/K for G, 2D₁, and 2D₂ bands, respectively. However, when temperature goes beyond 100 °C nonlinear effect occurs to both G and 2D bands, which is due to the anharmonic effect of phonons as discussed in Eq.(2.14). For ME graphene sample, the temperature dependence starts to become nonlinear when temperature is > 100 °C for both modes. The G band, which is in-plane vibration, is very susceptible to the surrounding environment, particularly the substrate. As a single-layer film, the morphology can be modified when the temperature increases, because the differential thermal expansion of graphene with respect to the substrate. Graphene has a negative in-plane thermal expansion coefficient of $(-8.0 \pm 0.7) \times 10^{-6} \text{K}^{-1}$ [21], while SiO₂ has a small positive thermal expansion coefficient of $\sim 0.5 \times 10^{-7} \text{K}^{-1}$. Thus, if there is significant bonding between graphene and substrate, with increasing temperature graphene film will undergo a tensile strain, as graphene tends to shrink while the substrate expand. As temperature reaches 100 °C, the strain reaches a critical point that the film slips on the surface of substrate and release the strain, resulting in a kink at ~ 175 °C in G-band temperature dependent curve. After the rearrangement of the graphene film, the temperature dependence tends to be linear again, but with a larger slope due to tensile strain. The bonding likely becomes stronger after the relaxation, thus, does not show another apparent kink. Similar nonlinear behavior is observed in 2D-band temperature dependence, showing a smaller kink at ~ 175 °C. Starting from the temperature of 300 °C, a peak appears at $\sim 1350 \text{ cm}^{-1}$ which is believed to be D peak, as shown in Figure 3.7b. In Figure 3.8a-b, the spectra before and after temperature-dependent Raman measurements are shown. The peak position of G band exhibits a blueshift from 1584.1 to

1588.7 cm^{-1} , while that of 2D band shows almost no shift after the annealing process. The blueshift of G band is due to the compressive strain originating from the difference in TEC between graphene and substrate. The FWHM broadens from 13.1 to 19.1 cm^{-1} for G band, and from 25.4 to 31.4 cm^{-1} for 2D band, respectively. Besides, the appearance of the broad D peak at RT after annealing indicates the increase of doping or defect level in the film, which might not originate from graphene itself but amorphous carbon generated from residual hydrocarbons of the tape at high temperature. This doping effect coupled with the morphology change of graphene film is the origin of the broadening and shift of both G and 2D bands after annealing.

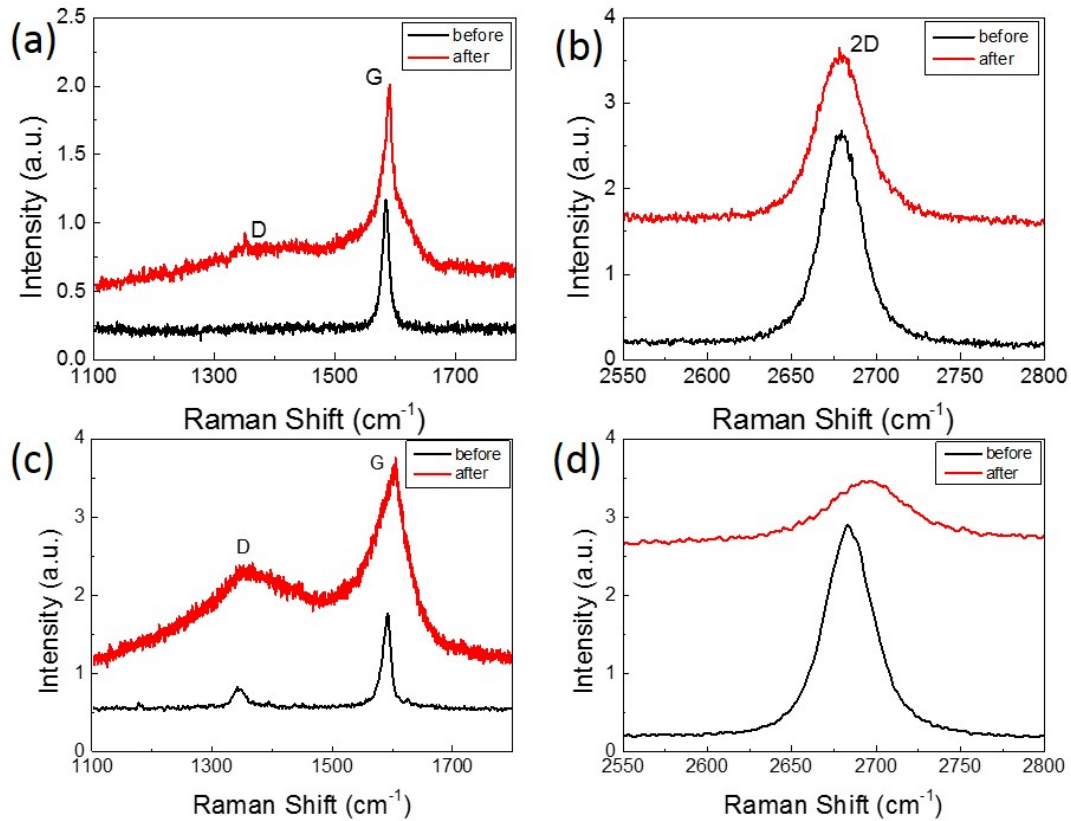


Figure 3.8: The spectra before and after temperature-dependent Raman measurement. (a)-(b) The Raman spectra of (a) G and (b) 2D bands before and after the measurements for the ME graphene sample. (c)-(d) The Raman spectra of (c) G and (d) 2D bands before and after the measurements for the CVD graphene sample.

For G band, the results of CVD-grown graphene sample show a super nonlinear temperature dependence, with a steeper redshift in Raman frequency than the graphite as temperature elevated to 150 °C and a strong bowing afterward. As discussed in ME graphene sample, the slip of graphene occurs when the strain reaches a critical point, which may cause the G peak to blueshift. However, since the density of polymer residues is higher in CVD-grown film than that in ME film, the D and G bands are extremely broad at high temperatures (Figure 3.7), which is due to doping caused by the residual hydrocarbons. Meanwhile, the doping from residues can also cause the blueshift of G band. With increasing temperature, the more decomposition of the residues is, the more doping would be introduced to the film, resulting in more blueshift in G band frequency. After the sample is cooled down to room temperature, the broad D and G peaks are still seen, as shown in Figure 3.8. As for 2D band, the temperature dependence shows an ‘S’-shaped curve, similar to that of ME graphene sample. The 2D band of CVD-grown graphene does not show as significant shift as that of ME graphene at elevated temperatures. Additionally, as the temperature rises, the changes of film morphology such as ripples will provide additional scattering of the near-K-phonons associated with 2D band, arising from the anharmonic phonon-phonon interaction [104]. Comparing the spectra of 2D band before and after annealing, the peak position shifts from 2683.9 to 2695.5 cm^{-1} while the FWHM increases from 30.7 to 57.3 cm^{-1} , which is also associated with the increasing density of doping or defects in the film.

3.3 Conclusions

In conclusion, temperature-dependent Raman spectroscopy has been applied to investigate the vibrational and thermal properties of graphene, prepared by either mechanical exfoliation or CVD, which is held by SiO_2/Si substrates. Graphite as the reference

shows the redshift of both G and 2D peaks. However, the temperature dependence of graphene samples exhibits nonlinear behavior. For the CVD-grown graphene, both G and D peaks become very broad after annealing, which are attributed to the hydrocarbonization of the polymeric residues mainly from the transfer process. The annealing process cause the residues to form amorphous carbon on the surface of graphene, resulting in the change of electronic structure, and hence the scattering process of phonons. Furthermore, as the temperature increases, the morphologic change of graphene, which arises from the difference in thermal expansion coefficients between graphene and substrate, is another important contribution to the shift of Raman frequency. As for ME graphene, since much less residues are introduced to the film, the extent of broadening of G and D peaks is smaller than that of CVD-grown graphene. Whereas, the change of film morphology still plays a significant role in the shift of G and 2D peaks. Therefore, though annealing provides an easy way to remove polymer residues on graphene, the leftover remains can significantly modify the electronic structure and further affect the performance of graphene-based devices. These observations suggest that the development of a polymer-free transfer technique is desirable, and the protection of graphene from further contamination after fabrication is necessary.

CHAPTER 4: TEMPERATURE DEPENDENCE OF RAMAN SCATTERING IN MONOLAYER AND BILAYER MoS_2

4.1 Fabrication and Characterization of MoS_2 Samples

4.1.1 Sample Fabrication

MoS_2 samples investigated have been prepared by two methods: mechanical exfoliation (from a purchased single crystal sample from SPI Supplies) and chemical vapor deposition (provided by Prof. Lin-you Cao's group at NCSU [105]). The 1L MoS_2 flake was mechanically exfoliated from nature crystalline bulk MoS_2 and transferred onto a silicon wafer covered by a 300-nm-thick thermal oxide (SiO_2) layer (Sample 1L-ME- SiO_2). The CVD-grown 1L and 2L samples were prepared on two types of substrates, SiO_2/Si and sapphire labeled as, respectively, 1L-CVD- SiO_2 , 1L-CVD-Sa, 2L-CVD- SiO_2 , and 2L-CVD-Sa. Originally the MoS_2 films were grown on sapphire wafers, and then transferred to SiO_2/Si wafers by scotch tape. A bulk MoS_2 sample was placed on SiO_2/Si substrate as reference. Figure 4.1 shows the optical images of all these samples.

4.1.2 Characterization of MoS_2 samples

Figure 4.2 shows an AFM image of the sample 1L-ME- SiO_2 , confirming the monolayer MoS_2 thickness to be ~ 0.7 nm. Besides AFM to determine the thickness or layer number of MoS_2 thin film, Raman spectroscopy is another powerful and nondestructive technique to not only determine the layer number by the Raman frequency of major

MoS₂ Raman modes, but also to investigate structural and electronic properties of MoS₂.

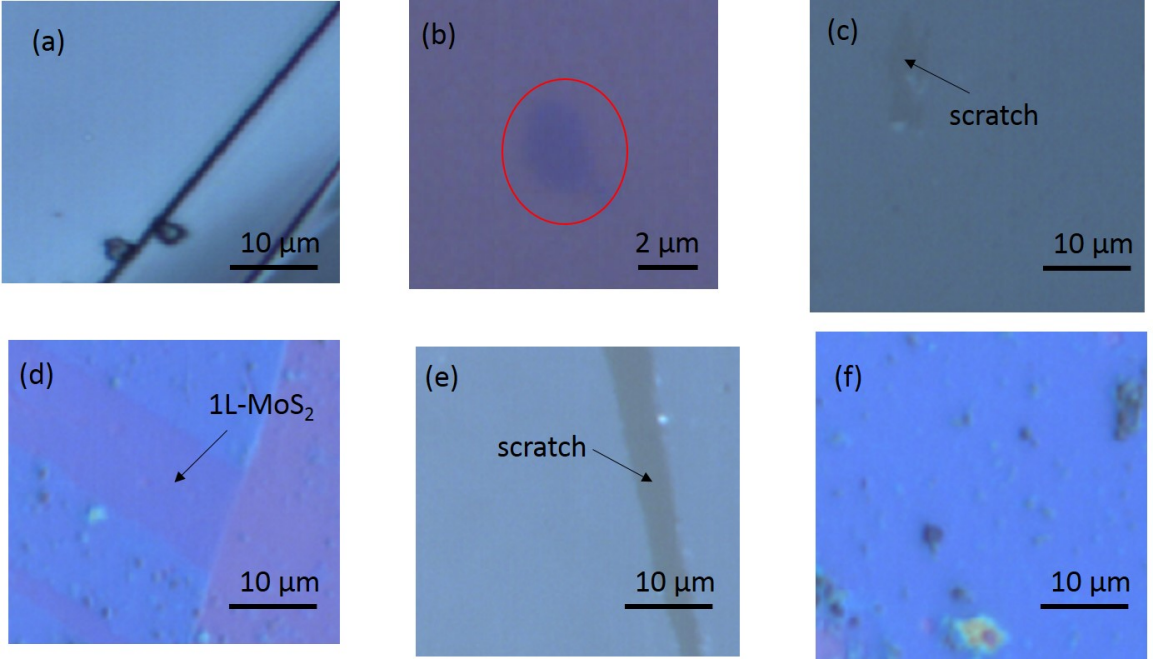


Figure 4.1: The optical images of MoS₂ samples. (a) Bulk MoS₂. (b) ME monolayer MoS₂ on SiO₂/Si – 1L-ME-SiO₂. (c) CVD-grown monolayer MoS₂ on sapphire – 1L-CVD-Sa. (d) CVD-grown monolayer MoS₂ transferred onto SiO₂/Si – 1L-CVD-SiO₂. (e) CVD-grown bilayer MoS₂ on sapphire – 2L-CVD-Sa. (f) CVD-grown bilayer MoS₂ transferred onto SiO₂/Si – 2L-CVD-SiO₂. Polymeric residues can be clearly seen.

A single-layer MoS₂ is formed by the arrangement of a triangular or simple hexagonal plane of Mo atoms sandwiched between two triangular layers of S atoms in a triangular prismatic fashion (Figure 4.3a). Bulk MoS₂ is a periodically stacked S-Mo-S layers through Van der Waals force. The space group of single layer MoS₂ is $P6m2$ (point group D_{3h}), and the four first-order Raman active modes at the center of Brillouin zone are 32 cm⁻¹ (E_{2g}^2), 286 cm⁻¹ (E_{1g}), 383 cm⁻¹ (E_{2g}^1), and 408 cm⁻¹ (A_{1g}), as illustrated in Figure 4.3b [42, 45]. The E_{2g}^2 mode arises from the relative motion between two MoS₂ layers, which will vanish in the single layer sample. The E_{2g}^1 mode is forbidden in back-scattering measurement on the basal plane perpendicular to the c axis. The E_{2g}^1 mode is attributed to the in-plane relative motion between the two S

atoms and the Mo atom, whereas the A_{1g} mode the out-of-plane vibration of two S atoms in opposite directions. Strictly speaking, the two active Raman modes E_{2g}^1 and A_{1g} (in D_{6h} for bulk MoS₂) should be assigned as E' and A'_1 in the monolayer MoS₂ (in D_{3h}) [106,107]. However, to see the evolution from the bulk to single-layer [45,108], the two modes are simply labelled as E_{2g}^1 and A_{1g} for all cases, as commonly done in the literature.

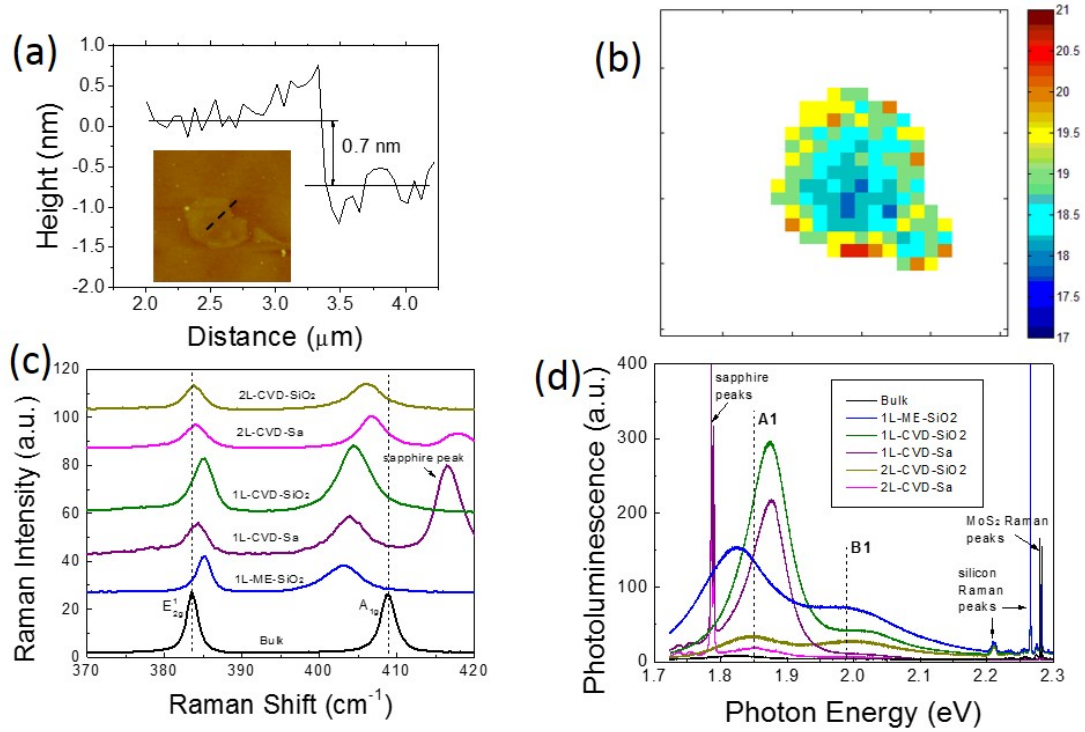


Figure 4.2: The characterizations of all the six MoS₂ samples. (a) AFM image of 1L-ME-SiO₂ showing the thickness of the film to be 0.7 nm. (b) The map of frequency difference between E_{2g}^1 and A_{1g} modes. (c)-(d) (c) Raman and (d) PL spectra of all the six samples.

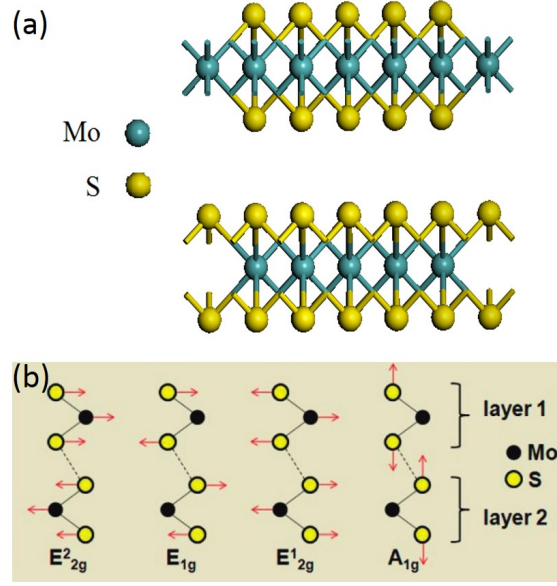


Figure 4.3: MoS₂ structure and Raman active modes. (a) Schematic model of MoS₂ structure. (b) Atomic displacements of the four Raman-active modes for the bulk MoS₂.

The room temperature Raman spectra of all the six samples in Figure 4.1 are shown in Figure 4.2c, measured with 532 nm laser at ~ 1 mW using the $100\times$ lens. The Raman frequency difference ($\Delta\omega$) between the E_{2g}^1 and A_{1g} modes can be correlated with the layer number [108]. For monolayer MoS₂, $\Delta\omega = 19$ cm⁻¹, for bilayer 22 cm⁻¹, and for the bulk 26 cm⁻¹ [108, 109]. $\Delta\omega$ is a better indicator for the layer number than the absolute ω value of each peak that is more sensitive to the strain. Theoretically, when the layer number increases, the interlayer van der Waals force in MoS₂ suppresses atom vibration, leading to higher force constants. Therefore, both E_{2g}^1 and A_{1g} modes are supposed to stiffen (blueshift) [110, 111]. The observed blueshift of A_{1g} mode with increasing layer number is consistent with the theoretical prediction. However, it is also found that the frequency of E_{2g}^1 peak decreases as the layer number increases, suggesting that interlayer van der Waals force plays a minor role while stacking-induced structure changes or long-range Coulombic interlayer interactions in multilayer MoS₂ may dominate the change of atomic vibration. Figure

4.2b shows the spatial variation of the frequency difference ($\Delta\omega$) of 1L-ME-SiO₂, and it is all found to be less than 20 cm⁻¹, indicating the film is indeed monolayer.

As is known, when the layer number of MoS₂ goes to monolayer, the band structure of MoS₂ transforms from indirect to direct [43]. It has also been reported that the PL of MoS₂ has two peaks that correspond to A (1.85 eV) and B (1.98 eV) exciton transitions, split by the spin-orbit coupling of the valence band. PL spectra of all these samples are shown in Figure 4.2d. For sample 1L-ME-SiO₂, the A and B transitions are, respectively, at 1.82 eV and 1.98 eV, for single-layer CVD samples 1.87 eV and 2.0 eV, and for bilayer CVD samples 1.85 eV and 1.99 eV. The precise excitonic bandgap value is in fact not known so far. The accepted values are approximately within the range of 1.8-1.9 eV [43,108,112–114] This situation is unfortunately general for monolayer or few layers TMDs. The variation of the PL peak positions of MoS₂ samples could be due to the interaction between the film and the substrate and possibly impurities and doping in the films. For MoS₂ films on SiO₂/Si substrate, it is generally believed that there is charge transfer between MoS₂ and substrate to form trions which has a lower energy than free excitons [115]. This could be another reason that 1L-ME-SiO₂ exhibits smaller energy of A-exciton emission. In general, the 1L MoS₂ samples show the strongest PL signal, while the bulk MoS₂ negligible, as expected due to the electronic band structure change.

4.2 Temperature Dependence of Raman Scattering

4.2.1 Temperature Dependent Raman Spectroscopy

The temperature dependences of both E_{2g}^1 and A_{1g} peak positions were performed in the range from room temperature (25 °C) to 500 °C, shown in Figure 4.4a-d. The upper temperature range in this work is substantially higher than those in the previous

works $< 250^\circ\text{C}$. The results of bulk MoS_2 are used as a reference. Empirically, the temperature dependence of Raman shift can be described by:

$$\omega(\Delta T) = \omega_0 + \chi_1\Delta T + \chi_2(\Delta T)^2 + \chi_3(\Delta T)^3, \quad (4.1)$$

where ω_0 is the frequency at room temperature, ΔT is the temperature change relative to room temperature, and χ_1 is the first-order temperature coefficient. The second (χ_2), third (χ_3) or higher order temperature effects are usually assumed to be small in the literature. In reality, the nonlinear effects are found to be quite significant for 1L or 2L MoS_2 even in a temperature range where the linear dependence might be expected to be adequate, for instance, below 200°C , depending on the substrate. Even for bulk MoS_2 , the nonlinearity occurs at around 200°C for both E_{2g}^1 and A_{1g} , though rather weak, but nevertheless evident in our data.

It is perhaps reasonable to assume that the temperature shift for a free standing few-layer MoS_2 should be rather close to that of the bulk material, despite the difference in the absolute position. Therefore, to show more clearly the substrate effect, we can take the temperature shifts of the bulk sample as references. Figure 4.4e-h plot the difference in the Raman frequency shifts between the thin film sample and the bulk, $\delta\omega(\Delta T) = |\omega(\Delta T) - \omega_0|_{thin\,film} - |\omega(\Delta T) - \omega_0|_{bulk}$, for E_{2g}^1 and A_{1g} and for 1L and 2L samples. Below we discuss separately E_{2g}^1 and A_{1g} to examine the effects of two types of substrates.

(1) E_{2g}^1 : For both the 1L and 2L samples, as shown in Figure 4.4a,c, and Figure 4.4e,g, the E_{2g}^1 mode exhibits relatively weak nonlinearity or in general appears to be close to the temperature dependences of the bulk sample. The temperature dependences of the deviations from the bulk mode are qualitatively similar for the same type of substrate: 1L-CVD-Sa and 2L-CVD-Sa vs. 1L-CVD-SiO₂ and 2L-CVD-SiO₂,

which is more apparent in Figure 4.4e,g, due to subtle difference in the film-substrate coupling (to be discussed later). The deviations of 1L-ME-SiO₂ are somewhat different from the other samples, as shown in Figure 4.4e.

(2) A_{1g} : For both 1L-ME-SiO₂ and 1L-CVD-SiO₂, as shown in Figure 4.4b,f, the temperature dependence of A_{1g} mode is drastically different from that of the bulk, showing strong nonlinearity starting at temperature near 100 °C and an overall 'S' shape dependence. The Raman spectra of 1L-ME-SiO₂ at a few representative temperatures are shown in Figure 4.5. The FWHM of A_{1g} mode is 5.7 cm⁻¹ at room temperature, increasing to a maximum of 10.3 cm⁻¹ at around 125 °C, then it decreases to 6.3 cm⁻¹ when the temperature reaches 500 °C, whereas the FWHM of E_{2g}^1 mode increases from 2.2 cm⁻¹ at room temperature monotonically to 4.8 cm⁻¹ at 500 °C. However, 1L-CVD-Sa shows only small deviation from the bulk dependence, with an average slope of -0.0159 cm⁻¹/K by using linear fitting, up to 500 °C, then an obvious change occurs, becoming nearly flat with a slope of -0.0027 cm⁻¹/K. As for the 2L samples, Figure 4.4d,h, similar to 1L-CVD-SiO₂, 2L-CVD-SiO₂ exhibits more significant deviation from the bulk sample than 2L-CVD-Sa when temperature < 400 °C. For 2L-CVD-Sa, the slope changes significantly when $T > 400$ °C from -0.0162 cm⁻¹/K to -0.0102 cm⁻¹/K. Again, one may notice that the temperature dependences of the deviations from the bulk mode are qualitatively similar for the same type of substrate: 1L-CVD-Sa and 2L-CVD-Sa vs. 1L-CVD-SiO₂ and 2L-CVD-SiO₂, which is more apparent in Figure 4.4f,h.

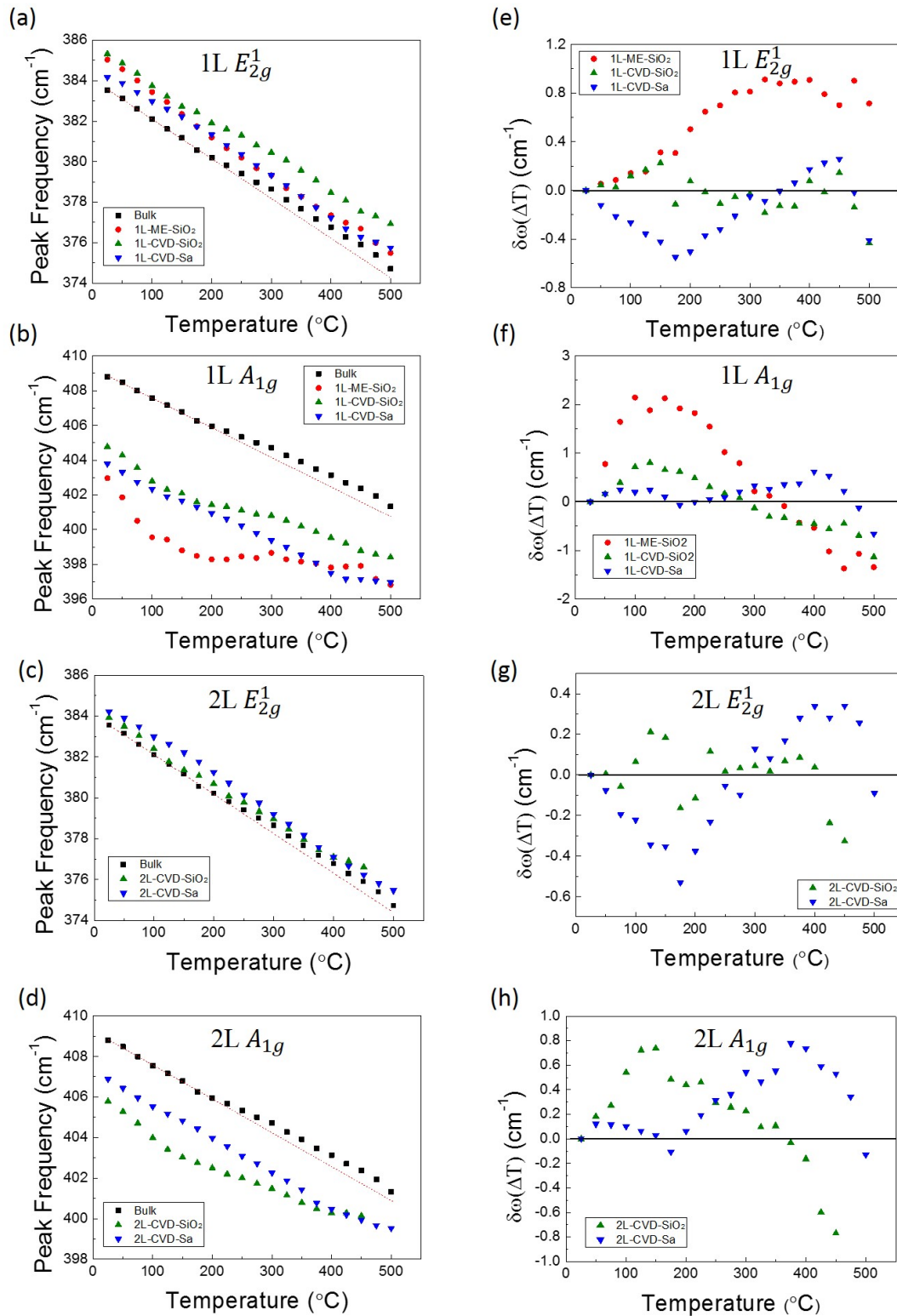


Figure 4.4: The temperature dependence of E_{2g}^1 and A_{1g} modes for all six samples. (a)-(d) Temperature dependence of Raman frequencies of E_{2g}^1 and A_{1g} modes in bulk and all other 1L and 2L samples. (e)-(h) The Raman frequency deviation of 1L and 2L MoS₂ relative to bulk MoS₂ as the reference.

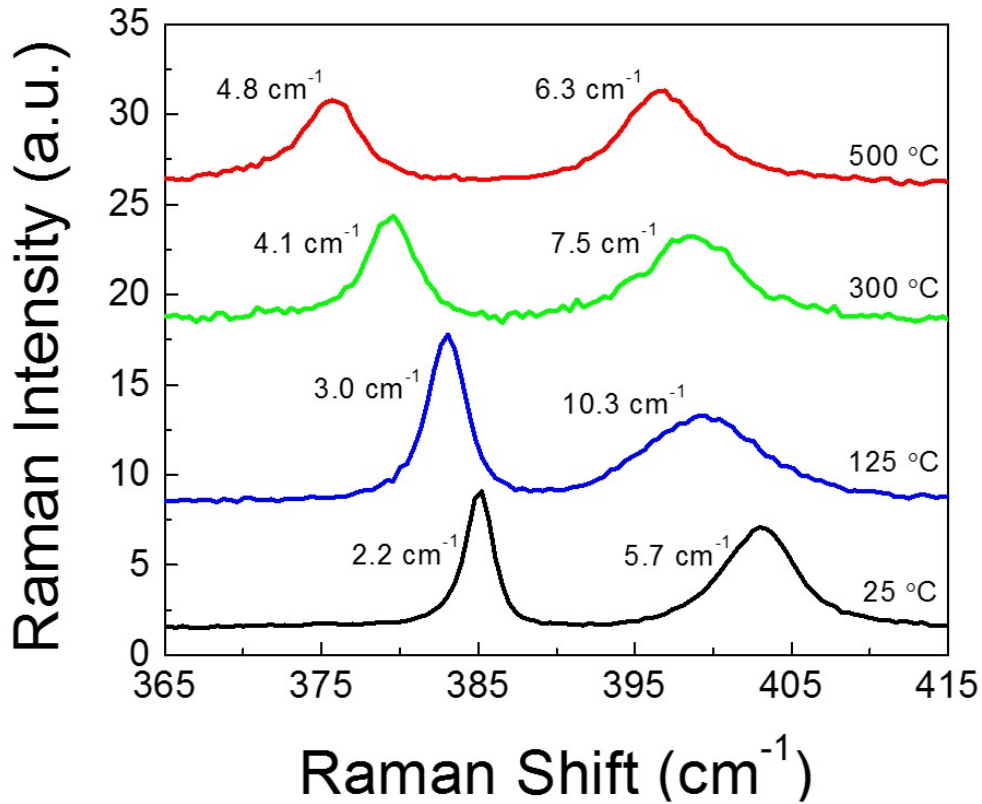


Figure 4.5: Representative Raman spectra of 1L-ME-SiO₂ sample at selected temperatures. The FWHM of E_{2g}^1 and A_{1g} are labelled next to the peaks.

Visually from Figure 4.4a-d, the A_{1g} mode shows more nonlinearity than the E_{2g}^1 mode. Qualitatively similar results have been observed in graphene: the peak position of G band, an in-plane vibrational mode, is less susceptible to the substrate influence than an out-of-plane vibration mode ~ 861 cm⁻¹ [102, 116]. Similarly it is reasonable to expect that in MoS₂ the in-plane mode (E_{2g}^1) will be less affected by the interaction between film and substrate than the out-of-plane mode (A_{1g}). Thus, it is not difficult to understand that the E_{2g}^1 mode typically shows more linear temperature dependent Raman shift than A_{1g} mode for both 1L and 2L samples. The difference between the SiO₂ and sapphire substrate also indicates that the coupling between the film and substrate depends on the substrate type and/or how the film and substrate

is bonded.

The temperature dependent data of all the samples are fitted to a third order polynomial function according to Eq.(4.1), with the coefficients listed in Table 4.1. The linear temperature coefficients of E_{2g}^1 and A_{1g} in bulk MoS₂ are $\chi_1 = -0.0221 \pm 8.9 \times 10^{-4}$ cm⁻¹/K and $-0.0197 \pm 8.9 \times 10^{-4}$ cm⁻¹/K, respectively. Bulk MoS₂, as the reference, can be treated as a stacking of single-layered MoS₂ films, and each layer has the same properties. With increasing temperature, all layers expand with the same rate without introducing any strain, leading to a nearly linear redshift of the Raman peak position for both E_{2g}^1 and A_{1g} modes. Although the interlayer coupling has led to significant frequency shifts for the two modes between 1L and bulk, the changes in temperature coefficients are expected to be relatively small. For the E_{2g}^1 mode, the first-order temperature coefficients (χ_1) of SiO₂ samples, both 1L and 2L, are close to that of bulk MoS₂, while those of the sapphire samples are much smaller. For A_{1g} , all the SiO₂ samples yield much larger χ_1 's than that of bulk MoS₂, while sapphire samples are close to bulk MoS₂. Our results for the films on SiO₂/Si are contradicting to or significantly different from those reported in the literature, because the improved data accuracy allows to examine the nonlinear effect that was neglected.

Table 4.1: Temperature coefficients of bulk, 1L and 2L samples with polynomial fitting to third order.

	χ_1	χ_2	χ_3	
E_{2g}^1	bulk	$-0.0221 \pm 8.9 \times 10^{-4}$	$2.12 \times 10^{-5} \pm 4.4 \times 10^{-6}$	$-2.94 \times 10^{-8} \pm 6.1 \times 10^{-9}$
	1L-ME-SiO ₂	-0.0241 ± 0.0015	--	--
	1L-CVD-SiO ₂	-0.0217 ± 0.0017	$2.04 \times 10^{-5} \pm 8.4 \times 10^{-6}$	$-2.68 \times 10^{-8} \pm 1.2 \times 10^{-8}$
	1L-CVD-Sa (till 425 °C)	$-0.0143 \pm 5.7 \times 10^{-4}$	$-1.44 \times 10^{-5} \pm 3.4 \times 10^{-6}$	$7.71 \times 10^{-9} \pm 5.6 \times 10^{-9}$
	2L-CVD-SiO ₂ (till 400 °C)	-0.0233 ± 0.0018	$3 \times 10^{-5} \pm 1.1 \times 10^{-5}$	$-4.61 \times 10^{-8} \pm 2 \times 10^{-8}$
	2L-CVD-Sa (till 425 °C)	$-0.0135 \pm 8.4 \times 10^{-4}$	$-2.54 \times 10^{-5} \pm 5.0 \times 10^{-6}$	$2.93 \times 10^{-8} \pm 8.2 \times 10^{-9}$
	bulk [117]	-0.0147		
	1L ME SiO ₂ Ref. [118]	-0.0179		
	2L ME SiO ₂ [118]	-0.0137		
	Few layers [119]	-0.0132		
A_{1g}	bulk	$-0.0197 \pm 8.9 \times 10^{-4}$	$2.49 \times 10^{-5} \pm 4.4 \times 10^{-6}$	$-3.53 \times 10^{-8} \pm 6.1 \times 10^{-9}$
	1L-ME-SiO ₂	-0.0626 ± 0.0038	$2.11 \times 10^{-4} \pm 1.7 \times 10^{-5}$	$-2.34 \times 10^{-7} \pm 2.1 \times 10^{-8}$
	1L-CVD-SiO ₂	-0.0301 ± 0.0023	$8.15 \times 10^{-5} \pm 1.1 \times 10^{-5}$	$-1.00 \times 10^{-7} \pm 1.6 \times 10^{-8}$
	1L-CVD-Sa (till 425 °C)	-0.0199 ± 0.0012	$3.10 \times 10^{-5} \pm 7.2 \times 10^{-6}$	$-5.77 \times 10^{-8} \pm 1.2 \times 10^{-8}$
	2L-CVD-SiO ₂ (till 400 °C)	-0.0310 ± 0.0018	$8.56 \times 10^{-5} \pm 1.2 \times 10^{-5}$	$-1.16 \times 10^{-7} \pm 2.0 \times 10^{-8}$
	2L-CVD-Sa (till 425 °C)	-0.0160 ± 0.0014	--	--
	bulk [117]	-0.0123		
	1L ME SiO ₂ Ref. [118]	-0.0143		
	2L ME SiO ₂ [118]	-0.0189		
	Few layers [119]	-0.0123		

Because all the SiO₂ samples were produced by mechanical exfoliation with the scotch tape, including transferred MoS₂ films, it is possible that wrinkles or ripples were introduced to the films, resulting in a considerable strain in the film. Figure 4.6 gives the spatial maps of the Raman frequencies of E_{2g}^1 and A_{1g} modes for mechanically exfoliated single-layer MoS₂ film on SiO₂/Si (1L-ME-SiO₂) at room temperature. The maps demonstrate that the frequency of A_{1g} show a larger variation than that of E_{2g}^1 , indicating that the morphology of the film impacts the Raman frequency of A_{1g} more than that of E_{2g}^1 . On the other hand, both 1L and 2L MoS₂ films were originally grown on sapphire. It has been reported, for graphene, the possibility of forming bonds between mechanically exfoliated graphene and substrate is quite low; however, such bonds are possible with high-temperature growth. It is reasonable to believe that

the CVD growth of MoS₂ films at the temperature higher than 800 °C could produce somewhat stronger bonding between the MoS₂ film and sapphire substrate than in the case of transferred film. With increasing temperature, the chemical bonding would influence the in-plane vibration, giving rise to a damping of Raman frequency redshift to E_{2g}^1 mode at the low temperature region, as manifested on the reduced magnitude of χ_1 for the CVD-grown MoS₂ films on sapphire. Furthermore, the film-substrate coupling leads to the sign changes for both χ_2 and χ_3 compared to the bulk for the E_{2g}^1 mode of the on-sapphire samples. In contrast, mechanically transferred MoS₂ films on SiO₂/Si do not form the chemical bonding between film and substrate other than van der Waals force, leading to the temperature dependence of Raman shift or χ_1 of the E_{2g}^1 mode similar to bulk MoS₂. However, the MoS₂ films on SiO₂/Si are more likely to be affected by the changes in the film morphology such as wrinkles and ripples when temperature increases, due to thermal expansion coefficient mismatch between MoS₂ and SiO₂. These changes of morphology in turn will have a large impact on out-of-plane vibration (A_{1g}), causing not only the nonlinear effect of temperature coefficient but also the large deviation of χ_1 from bulk MoS₂ for the SiO₂/Si samples. As for the sapphire samples, the chemical bonding restricts the MoS₂ film from morphology change, and the coupling with the substrate has a relatively small influence on the A_{1g} mode. Therefore, we can conclude that the morphology of MoS₂ films plays a significant role in temperature dependence of A_{1g} mode, which leads to the large and highly non-linear deviation from the bulk, while the bonding between film and substrate introduces weaker effects, in similar magnitudes, to both E_{2g}^1 and A_{1g} modes on their temperature induced Raman shifts.

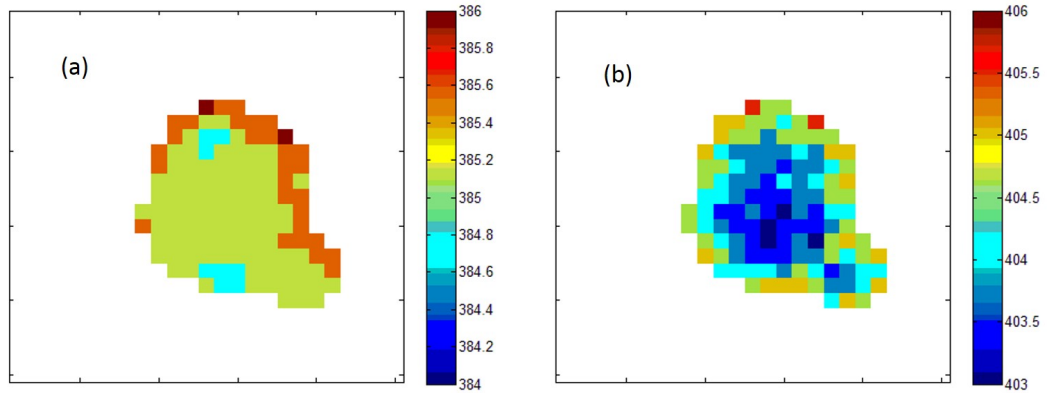


Figure 4.6: Spatial maps ($6\mu m \times 6\mu m$) of the Raman frequencies of (a) E_{2g}^1 and (b) A_{1g} modes for 1L-ME-SiO₂ sample, and the unit is cm⁻¹.

The integrated Raman intensity for both E_{2g}^1 and A_{1g} modes has been found to decrease in all CVD-grown samples when T is greater than 400 °C, possibly due to the decomposition of MoS₂ films. The thermal decomposition temperature for most samples including bulk is somewhere > 800 °C, except for 2L-CVD-SiO₂ being near 450 °C. For all CVD-grown MoS₂ films on sapphire, no Raman signal is detectable when the temperature reaches 575 °C, indicating the decomposition of MoS₂ films.

The Raman spectrum does not recover at room temperature after reaching the maximum temperature. For 1L-ME-SiO₂, the main change is that the frequency difference between A_{1g} and E_{2g}^1 modes increases by 2.5 cm⁻¹, as shown in Figure 4.7. In addition, their peak intensities decrease. There are at least two possible reasons: (1) the strain or morphology has changed, as expected, (2) the sample might be partially oxidized or decomposed. Similar results have been reported for graphene [120].

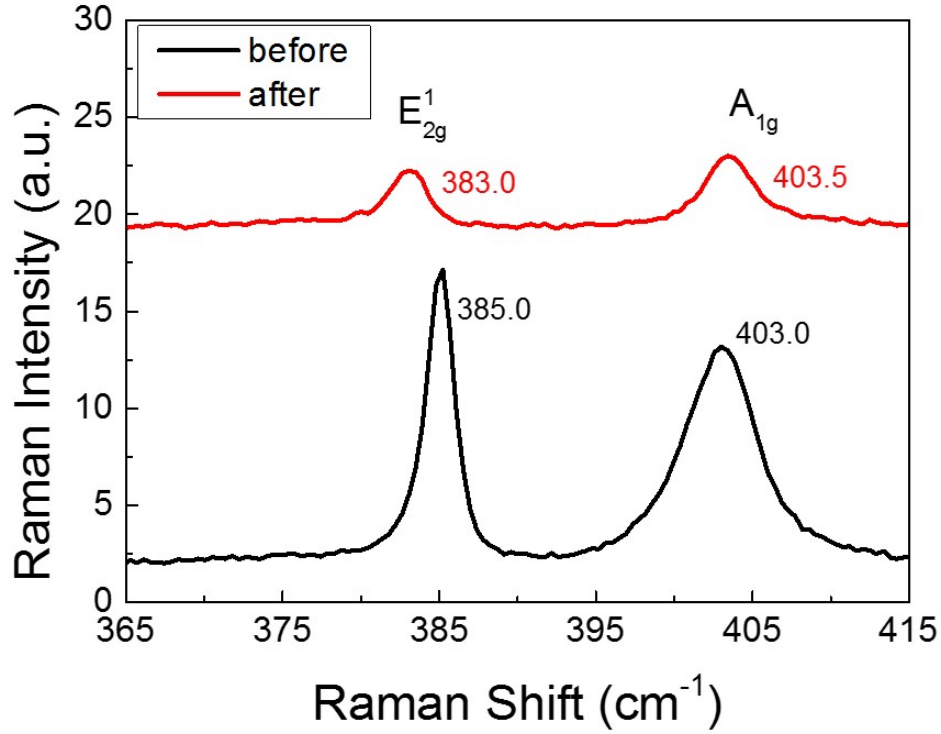


Figure 4.7: Raman spectra collected before and after temperature-dependent Raman measurements.

4.2.2 Simulation for Temperature Dependence of Raman Shift

As Eq.(2.14) shows, the intrinsic temperature dependence of the Raman shift can be divided into thermal expansion of the lattice ($\Delta\omega_E$) and an anharmonic effect ($\Delta\omega_A$) which causes the change of phonon self-energy. In addition, thermally induced strains due to thermal expansion coefficient mismatch ($\Delta\omega_M$) between MoS₂ film and substrate should be considered. Thus, the measured frequency change can be written as

$$\Delta\omega(T) = \Delta\omega_E(T) + \Delta\omega_A(T) + \Delta\omega_M(T), \quad (4.2)$$

where the term $\Delta\omega_M$ can be expressed as

$$\Delta\omega_M(T) = \beta \int_{25^\circ\text{C}}^T (\alpha_{sub}(T) - \alpha_{MoS_2}(T)) dT, \quad (4.3)$$

where β is the biaxial strain coefficient, α_{sub} and α_{MoS_2} are the thermal expansion coefficients of substrate and MoS₂, respectively. With increasing temperature, both MoS₂ and SiO₂ expand but at different rates, resulting in strain in the MoS₂ thin films. Since the thermal expansion coefficient of MoS₂ is larger than that of SiO₂, the strain in the film will be compressive. When the strain reaches a critical point the MoS₂ film tends to slip on the surface of the substrate as well as change the film morphology. For 1L-ME-SiO₂ sample, this process takes place at $\sim 100^\circ\text{C}$ where there is an obvious slope transition of A_{1g} frequency shift. As a result, defects may be introduced in the MoS₂ film such as the breakdown of Mo-S bonds and the slow decomposition of the film, showing a broadening of A_{1g} Raman peak (Figure 4.5).

Eq.(4.3) assumes that the film and substrate is in coherent strain, which is likely invalid for the transferred film. For bulk MoS₂, there is no thermal expansion coefficient mismatch between MoS₂ layers, so that the third term is zero. Therefore, using Eq.(2.14) the Raman shift of bulk MoS₂ can be simulated. To simulate the contribution of thermal expansion of the lattice ($\Delta\omega_E$) from Eq.(2.15), the Grüneisen parameters of both E_{2g}^1 and A_{1g} modes for bulk MoS₂ are $\gamma(E_{2g}^1) = 0.21$ and $\gamma(A_{1g}) = 0.42$, respectively. The in-plane and out-of-plane thermal expansion coefficients for bulk MoS₂ can be derived from expressions as below [121]:

$$\alpha_a(T) = \left(\frac{0.6007 \times 10^{-5} + 0.6958 \times 10^{-7}T}{a} \right) \left(\frac{1}{^\circ\text{C}} \right) \quad (4.4a)$$

$$\alpha_c(T) = \left(\frac{0.1064 \times 10^{-5} + 1.5474 \times 10^{-7}T}{c} \right) \left(\frac{1}{^\circ\text{C}} \right) \quad (4.4b)$$

where a and c are the lattice constants of MoS₂ in Å. They are calculated to be $2.48 \times 10^{-6}/^\circ\text{C}$ and $9.14 \times 10^{-6}/^\circ\text{C}$, respectively, for in-plane and out-of-plane thermal expansion coefficients at room temperature. The second term of right-handed side in Eq.(2.14) is expressed as Eq.(2.18a), which is called “self-energy” shift due to anharmonic coupling of multiple phonons. The coefficients A and B can be estimated by fitting the rest frequency shift after subtracting the contribution of thermal expansion of the lattice. The fitting parameters of A and B for both E_{2g}^1 and A_{1g} modes are listed in Table 4.2. Figure 4.8 shows the simulated Raman shifts of both E_{2g}^1 and A_{1g} modes for bulk MoS₂ with good agreement to experimental results. The results show that the pure thermal expansion effect is relatively small, and the self-energy contribution dominates the redshift.

Table 4.2: The fitting parameters A and B for both E_{2g}^1 and A_{1g} modes used in three- and four-phonon coupling model.

bulk MoS ₂	A (cm ⁻¹)	B (cm ⁻¹)
E_{2g}^1	-3.05835	0.04204
A_{1g}	-5.68777	0.26566

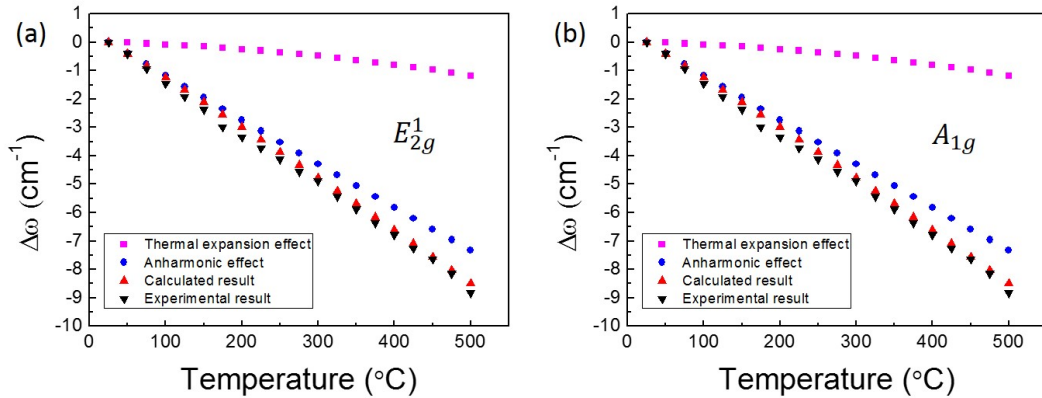


Figure 4.8: The modeling of temperature dependent Raman shift. The model of temperature dependent Raman shift relative to room temperature including the contributions of thermal expansion effect of lattice and anharmonic effect as compared to experimental results of bulk MoS₂ for (a) E_{2g}^1 and (b) A_{1g} modes.

4.2.3 Full Width at Half Maximum (FWHM)

Figure 4.9 shows the temperature dependent FWHM of both E_{2g}^1 peak and A_{1g} peak for all samples, by fitting to a Lorentzian lineshape function. Bulk MoS₂ has room-temperature FWHMs of 1.6 and 2.2 cm⁻¹, respectively, for E_{2g}^1 and A_{1g} . Other samples have greater FWHMs, indicating that the film-substrate coupling and defects existing in these samples may have caused the peak broadening. The FWHM of E_{2g}^1 mode, in general, increases linearly with increasing temperature. However, the A_{1g} mode does not show a monotonic dependence but with a maximum linewidth in the middle of the temperature range. As it is discussed above, the mismatch of thermal expansion coefficients between MoS₂ films and substrates gives rise to changes of morphology e.g. wrinkles or ripples, consequently leading to a significant change of the temperature coefficients of A_{1g} mode. For all 1L and 2L samples, the FWHM of A_{1g} reaches the maximum when the realignment process occurs. For instance, the anomaly of temperature dependent Raman shift of 1L-ME-SiO₂ takes places at the temperatures starting from ~ 100 °C, while the FWHM reaches the maximum at 100 °C and then starts to decrease afterward. This gives an additional illustration that the change of the morphology by the thermal expansion coefficient mismatch can affect the out-of-plane vibrational mode more than the in-plane mode when the temperature reaches a critical value.

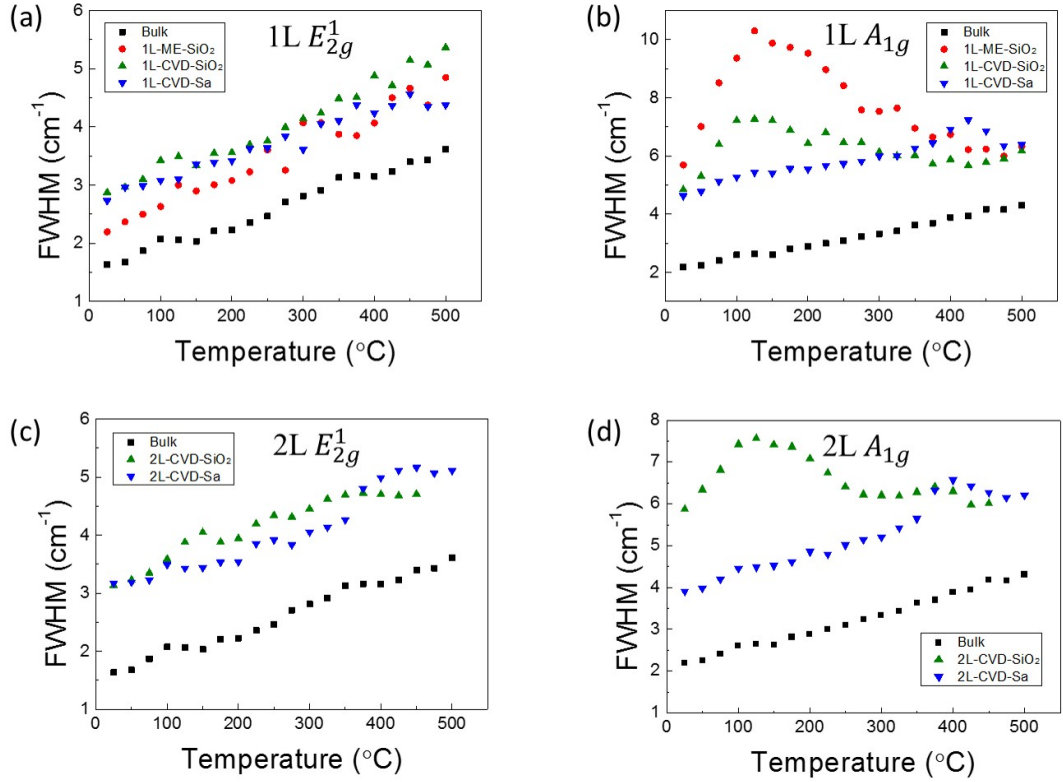


Figure 4.9: Temperature dependence of FWHM of E_{2g}^1 and A_{1g} modes in bulk and all other 1L and 2L samples.

4.3 Annealing Effect on Monolayer MoS₂ Film Transferred on SiO₂/Si Substrate

The morphology plays a significant role in the properties of MoS₂ films, and the morphologic variation of the film in a very thin film like a monolayer typically results in variation of strain in the film. It has been well studied both theoretically and experimentally that the strain in the two-dimensional material can be detected through the shift of its phonon modes using micro-Raman spectroscopy. For monolayer MoS₂, E_{2g}^1 mode is sensitive to the strain, while A_{1g} mode shows weaker strain dependence but it is also sensitive to doping in the film [122]. Besides using E_{2g}^1 shift as an indicator of the strain, the bandgap exhibits sensitive response to the strain applied in MoS₂ film, which can be used as another method to extract the strain distribution in the

film. In addition to strain effect, the doping effect is another key element that affects the properties of monolayer MoS₂, which can be analyzed by the shift of A_{1g} mode as well as the photoluminescence spectrum. The origin of doping for monolayer MoS₂ is considered to be the defects in the film and the charge transfer between the substrate and the film [114, 123].

Comparing the temperature dependence of monolayer MoS₂ films on SiO₂ and sapphire substrates, for A_{1g} mode, the nonlinear dependence of SiO₂ samples, as we discussed above, is quite possibly attributed to the morphologic change with increasing temperature, while, for E_{2g} mode, the smaller temperature coefficient of sapphire samples is due to the bonding at the interface of the substrate and the film. The temperature-dependent Raman measurements can be considered as an annealing process for the samples. Since the annealing can significantly change the morphology of the film as well as the bonding between the substrate and the film, one may ask: “would the temperature dependence be different if annealing the films for a second round?” In our previous temperature dependent studies, in order to understand the temperature dependences of the material properties in the full temperature range up to the decomposition temperature, we tended to bring the sample to the highest possible temperature at which the data could be practically taken. Thus, at the end of the measurement, the sample was damaged. However, as mentioned above, the morphology change was occurring along the process of varying temperature, which is effectively an annealing process. In this section, we report the temperature dependent study of MoS₂ monolayer by repeating the heating cycle, but each time only increasing the temperature to a “saf” level.

Monolayer MoS₂ film was originally grown on sapphire by CVD and then transferred onto Si substrate coated with 300 nm thick SiO₂ using polystyrene (PS) [124]. Figure 4.10a shows the optical image of the MoS₂ film with its AFM image in Fig-

ure 4.10b. The thickness is measured to be ~ 1 nm, indicating it is monolayer. The larger thickness of this transferred monolayer than the previous ME sample suggests a larger morphologic variation of this sample. Wrinkles and cracks can be seen in optical image Figure 4.10a. Wrinkles, as one typical morphology feature in a two-dimensional material, can manifest as local variation in strain. In order to further confirm whether the film is monolayer, the mapping of frequency difference between A_{1g} and E_{2g}^1 modes over an area of $20 \mu\text{m} \times 20 \mu\text{m}$ (marked square in Figure 4.10a) is shown in Figure 4.10c, with a maximum of 19.2 cm^{-1} , indicating the film overall is monolayer. The strip of relatively larger frequency difference in the map matches to a wrinkle in the film.

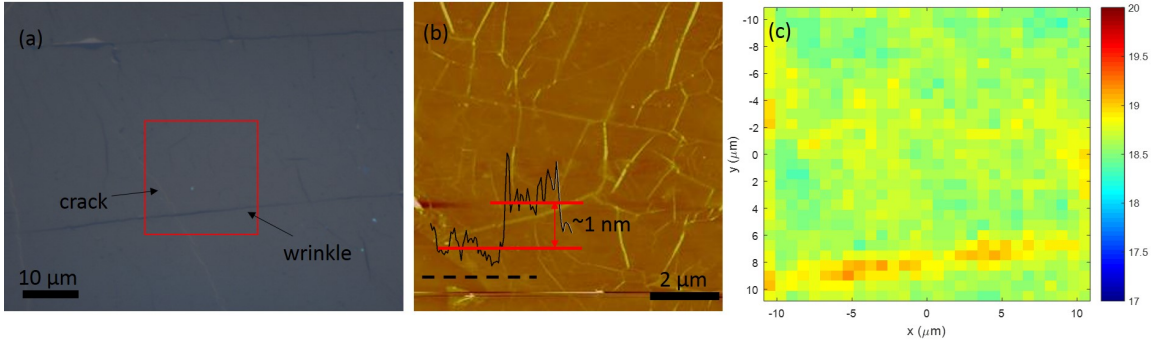


Figure 4.10: The optical image and characterizations of the monolayer MoS_2 film transferred onto SiO_2/Si substrate. (a) Optical image, (b) AFM image, (c) Map of frequency difference $\Delta\omega$ between E_{2g}^1 and A_{1g} modes in the red-squared area.

Figure 4.11 presents the Raman and PL mapping results at room temperature before annealing the film using spatial resolved micro-Raman and PL spectroscopy. Laser power of ~ 1 mW at 532 nm and $50\times$ lens were used. The mapping data of Raman intensity (Figure 4.11a-b) show overall uniform intensity distribution over the film except for around the crack with smaller intensity and along the wrinkle with higher intensity. However, the PL intensity mapping shows more significant variation of $\sim 20\%$ (Figure 4.11c). Raman and PL peak position mapping results are shown in Figure 4.11d-f, with maximum shifts of $\sim 0.6 \text{ cm}^{-1}$ for E_{2g}^1 mode, $\sim 0.7 \text{ cm}^{-1}$

for A_{1g} mode, and ~ 12 meV for PL, respectively. The deformation potentials for Raman modes and bandgap under biaxial strain have been estimated to be ~ 4.7 cm $^{-1}/\%$ for E_{2g}^1 , ~ 1.8 cm $^{-1}/\%$ for A_{1g} , and ~ 80 meV/ $\%$ for bandgap, respectively [125]. Thus, the corresponding strain difference in the film, using the maximum difference in the peak position, can be estimated to be $\sim 0.13\%$ for E2g, $\sim 0.39\%$ for A_{1g} , and $\sim 0.15\%$ for PL, respectively. The non-uniform strain distribution, reflected in the E_{2g}^1 frequency fluctuation, indicates the rippling of the film. However, the estimated strain difference from A_{1g} mode is much larger than that from E_{2g}^1 mode and PL, indicating that the doping effect plays a significant role in monolayer MoS $_2$ film. By comparing the peak position mapping of E_{2g}^1 and PL peak positions, the blue-circled (red-circled) area with relatively higher (lower) frequencies in E_{2g}^1 mode, which are expected to be under relatively larger compressive (tensile) strain, also exhibit higher (lower) PL energies, reflecting as lower (higher) PL intensity. This phenomenon can be explained by the relocalization of photo-induced excitons which tend to diffuse to lower bandgap regions before recombining. In contrast, areas with relative larger tensile strain have lower bandgap energies, thus trapping excitons and generating stronger PL locally (Figure 4.11c).

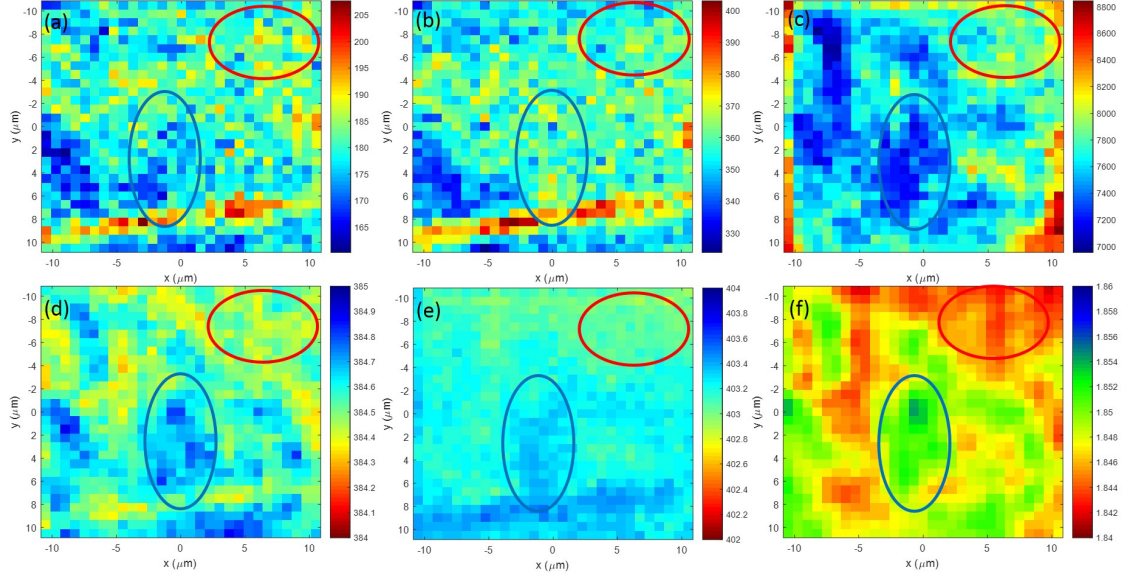


Figure 4.11: The Raman and PL mapping results of the monolayer MoS₂ film. (a)-(c) The intensity maps of E_{2g}^1 , A_{1g} and PL intensities. (d)-(e) The maps of peak positions of E_{2g}^1 , A_{1g} and PL.

Single-point temperature-dependent Raman measurements were carried out in the temperature range from room temperature to 305 °C with the step of 20 °C, with the same setup as those of previous MoS₂ samples. The sample point was selected from the central area. The first-cycle temperature dependence of both Raman modes of the monolayer MoS₂ film is shown in Figure 4.12a-b, with several representative spectra at different temperatures shown in Figure 4.12c. As expected, both E_{2g}^1 and A_{1g} modes, in general, exhibit redshift in their frequencies with increasing temperature. The E_{2g}^1 mode shows a very linear temperature dependence while the A_{1g} mode highly nonlinear, in good agreement with the results of previous MoS₂ samples. The temperature dependence of E_{2g}^1 mode is fitted by Eq.(3.1) and that of A_{1g} mode is fitted by Eq.(4.1) up to the third order, and the temperature coefficients are listed in Table 4.3. As discussed earlier, the nonlinear temperature dependence of A_{1g} mode is attributed to the change of film morphology, while E_{2g}^1 mode is not sensitive to morphology. With increasing temperature, the film tends to change its morphology due

to the mismatch of thermal expansion coefficient (TEC) between the SiO₂ substrate and MoS₂ monolayer. The TEC of SiO₂ is $\sim 0.5 \times 10^{-6} K^{-1}$ at room temperature, much smaller than monolayer MoS₂ ($\sim 7 \times 10^{-6} K^{-1}$ at RT), thus, its thermal expansion with increasing temperature is much smaller than that of MoS₂. Therefore, the strain within the small measured spot tends to accumulate with increasing temperature, and eventually goes beyond the confinement of van der Waals force, resulting in the change of the morphology of the film.

Table 4.3: Temperature coefficient of E_{2g}^1 and A_{1g} modes in two temperature cycles.

		First cycle	Second cycle
E_{2g}^1	χ	$-0.0192 \pm 3.2 \times 10^{-4}$	$-0.0183 \pm 8.6 \times 10^{-5}$
A_{1g}	χ_1	-0.0390 ± 0.0035	-0.0198 ± 0.0014
	χ_2	$6.97 \times 10^{-5} \pm 2.4 \times 10^{-5}$	$-5.74 \times 10^{-6} \pm 9.8 \times 10^{-6}$
	χ_3	$-3.69 \times 10^{-8} \pm 4.8 \times 10^{-8}$	$4.17 \times 10^{-8} \pm 2.0 \times 10^{-8}$

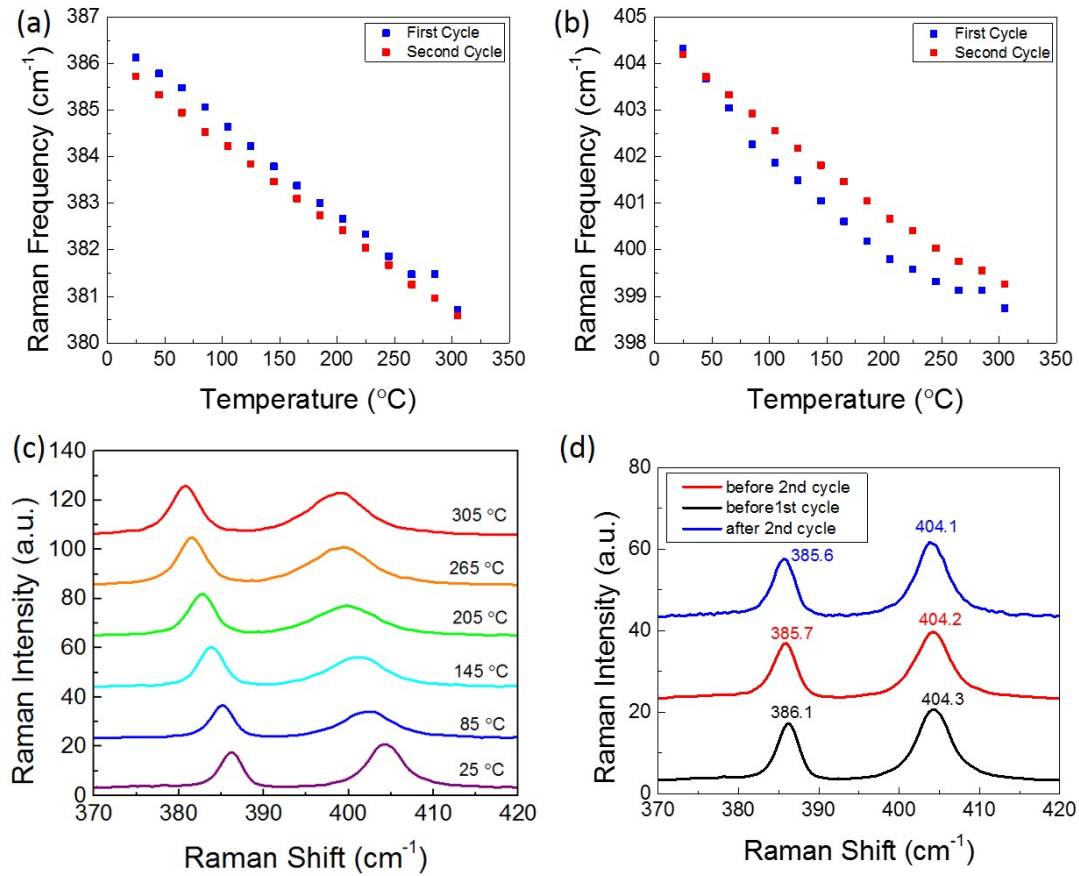


Figure 4.12: The temperature dependence of Raman spectroscopy of monolayer MoS₂ up to 305 °C. (a)-(b) The temperature dependences of (a) E_{2g}^1 and (b) A_{1g} modes in the first and second heating cycles. The first cycle is in solid blue square, and the second solid red circle. (c) Representative Raman spectra at different temperatures. (d) The Raman spectra at room temperature before the first-cycle heating, and before and after second-cycle heating.

On the other hand, the morphology of the film varies with increasing temperature, leading to the change of mechanical coupling of MoS₂ film with SiO₂ substrate. With increasing temperature, the charge transfer between the film and the substrate tends to increase as the contact of the MoS₂ film with the substrate becomes more uniform and close. Since A_{1g} mode is known to be sensitive to doping effect, the stronger charge transfer leads to larger shift of A_{1g} frequency, leading to the initial faster redshift (up to 100 °C) of the A_{1g} frequency. After the film's morphology

becomes more uniform and stable at higher temperatures, the redshift rate of A_{1g} frequency gradually slow down. In addition, the PS residues left on the film during transfer process, though will be eliminated with increasing temperature, may still introduce extra doping into the film to change the temperature dependence of A_{1g} mode. Therefore, the first-cycle annealing process modifies the morphology of the film and gets rid of the polymer residues from transfer process.

Figure 4.12a-b show the second-cycle temperature dependence of the E_{2g}^1 and A_{1g} modes at the same spot as the first cycle, after the sample is annealed at 305 °C for 30 minutes and then cooled down back to RT. Similar to the results of first-cycle measurements, the E_{2g}^1 mode shows a linear temperature dependence, while the A_{1g} remains nonlinear, but the extent of nonlinearity is smaller than that of the first cycle. The results of E_{2g}^1 and A_{1g} modes are fitted with Eq.(3.1) and Eq.(4.1), and their temperature coefficients are listed in Table 4.3. For E_{2g}^1 mode, the temperature coefficient in the second cycle becomes slightly smaller than that in the first cycle, which is attributed to the change of strain, i.e., the bonding has become stronger, in the film after the first-cycle annealing of the film. With the first-cycle annealing, the morphology has been modified, resulting in not only the doping concentration change but also the strain distribution in the film. Figure 4.12d shows the RT Raman spectra acquired before the first- and second-cycle annealing, respectively. The intensity shows very little change. The E_{2g}^1 frequency after the first cycle is slightly smaller than that before the first cycle (0.4 cm⁻¹ change), indicating that the strain at this location becomes more tensile after the first-cycle annealing. The A_{1g} frequency remains nearly the same. In the second cycle of temperature dependent measurements, the overall redshift of E_{2g}^1 mode becomes less, and hence smaller temperature coefficient. For A_{1g} mode, only a small nonlinear temperature dependence is observed, especially at relatively high temperatures, and its first-order temperature coefficient is almost halved compared to the first-cycle temperature dependent measurements.

As discussed in first-cycle annealing, the morphology the film has been modified and rearranged to a more stable condition, so the second-cycle annealing will not change the film morphology significantly further. The Raman spectrum after second-cycle annealing, shown in Figure 4.12d, almost shows no changes compared to that after first-cycle annealing, which further confirms our assumption.

Comparing the temperature dependences of these two-cycle annealing on the transferred MoS₂ sample with as-grown MoS₂ film on sapphire, the temperature coefficients of E_{2g}^1 mode from both cycles are larger than those of sapphire samples. As the smaller temperature coefficient of second cycle is attributed to the improved bonding between the substrate and the film, the as-grown monolayer MoS₂ on sapphire, whose bonding in between is much stronger than transferred samples, exhibits even smaller temperature coefficient. For A_{1g} mode, the nonlinear behavior of temperature dependence is quite similar to those previously measured transferred samples, either 1L or 2L, which has been proposed to the morphologic change of film with increasing temperature. However, the extent of nonlinearity decreased in the second cycle, and the Raman spectrum of measured spot showed no significant change before and after the annealing process. These evidences prove that the morphology of the MoS₂ film can be modified through annealing and becomes stable afterwards.

After annealing at 305 °C for one hour and then cooling down to RT, Raman and PL mapping were performed, and the results are shown in Figure 4.13a-d for mapping data of Raman and PL peak positions (Figure 4.13a-c) and PL intensity (Figure 4.13d). The variations of Raman and PL peak positions are found to be ~ 1 cm⁻¹ for E_{2g}, ~ 0.7 cm⁻¹ for A_{1g} , and ~ 15 meV for PL over the MoS₂ film, which corresponds to the variations in strain as $\sim 0.21\%$ for E_{2g}, $\sim 0.39\%$ for A_{1g} , and $\sim 0.19\%$ for PL, respectively. The strain difference over the mapped area becomes larger after two cycles of annealing due to the morphologic change of the film as we

discussed above. Interestingly, the PL intensity map, as shown in Figure 4.13d, is not exactly following the anti-correlation relation between the peak energy and intensity. For instance, the PL energies of location 1 and 2 (labelled in Figure 4.13c) are higher than surrounding areas, in accord with the higher E_{2g}^1 frequency in location 1 and 2 (the higher frequency is, the lower tensile strain); however, the PL intensity in location 1 is higher than that in surrounding areas while location 2 lower. Therefore, this cannot be simply explained by one mechanism of either strain or doping. Both locations undergo relatively blueshift in E_{2g}^1 frequency, suggesting less tensile strain. However, the A_{1g} frequency in location 1 is smaller than that in location 2 (Figure 4.13b), indicating that the doping concentration in location 1 is higher than that in location 2. In other words, after the rearrangement of film morphology after two cycles of annealing, the mechanical coupling of the MoS₂ film with the substrate varies over the film as well as the doping concentration. The concentration in location 2 is lower than that in location 1. Thus, though the PL energy in location 2 is higher than surrounding area, the lower doping concentration still leads to higher PL intensity. Whereas, the lower PL intensity in location 1 can be either explained by funnel effect or high doping concentration that quenches PL. The PL spectra from locations 1 and 2 (Figure 4.13e) show that the full width at half maximum (FWHM) of the PL spectrum at location 2 is 26 nm, smaller than location 1 which is 35 nm, suggesting lower doping concentration in location 2.

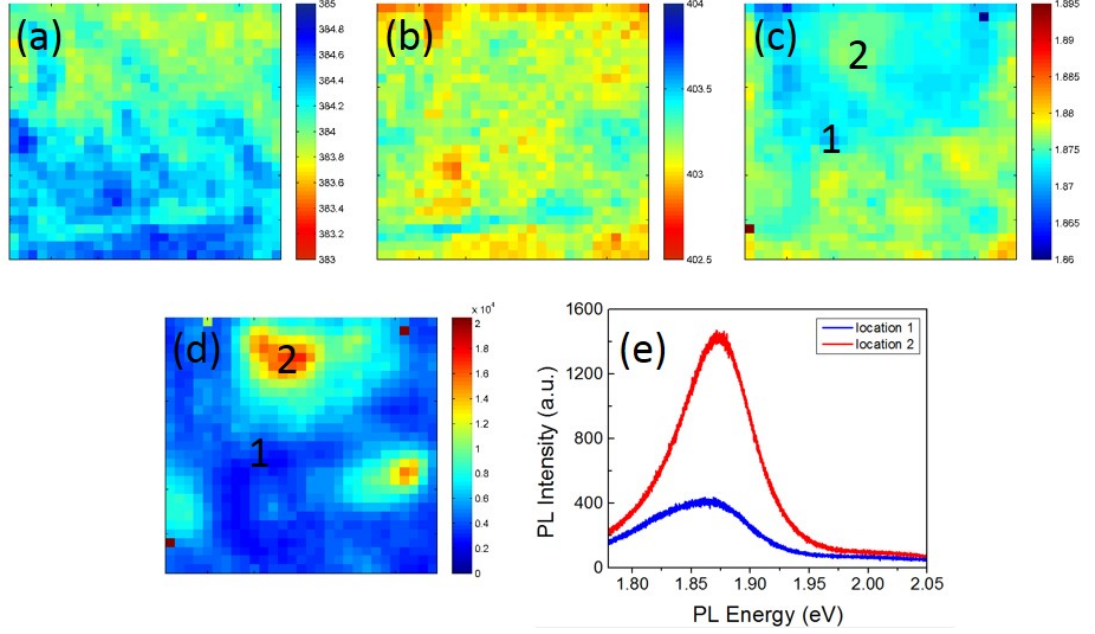


Figure 4.13: The PL and Raman mapping results after the second-cycle heating. (a)-(b) The maps of Raman frequencies of (a) E_{2g}^1 and (b) A_{1g} modes. (c) The map of PL peak position. (d) The intensity map of PL. (e) PL spectra of location 1 and 2 labelled in c.

4.4 Conclusions

In summary, temperature-dependent Raman studies were performed to investigate the vibrational properties of the in-plane E_{2g}^1 and out-of-plane A_{1g} modes of single- and bi-layer MoS_2 samples prepared by three methods: (1) as grown by CVD on sapphire substrate, (2) initially grown on sapphire substrate, then transferred onto SiO_2/Si substrate, and (3) ME samples placed on SiO_2/Si substrate, in a temperature range of 25-500 °C. Bulk MoS_2 has also been measured to serve as the references, with the first-order temperature coefficients of the Raman frequency shifts given as $\chi_1(E_{2g}^1) = -0.0221 \pm 8.9 \times 10^{-4} \text{ cm}^{-1}/K$ and $\chi_1(A_{1g}) = -0.0197 \pm 8.9 \times 10^{-4} \text{ cm}^{-1}/K$, respectively, for the E_{2g}^1 and A_{1g} mode. The thermal decomposition temperature is found to be approximately 575 °C for CVD-grown films on sapphire. The film-substrate coupling affects the temperature dependence of Raman frequency, intensity,

and linewidth for both E_{2g}^1 and A_{1g} modes in the 1L and 2L MoS₂. The impact depends on the substrate type and/or film-substrate binding mechanism. For the CVD grown film on the original sapphire substrate with likely chemical bonding between them, the film-substrate coupling significantly reduces the linear temperature coefficients of the Raman shift of the E_{2g}^1 mode to $-0.0143 \pm 5.7 \times 10^{-4} \text{ cm}^{-1}/K$ for 1L and $-0.0135 \pm 8.4 \times 10^{-4} \text{ cm}^{-1}/K$ for 2L, but has no or small effect on the A_{1g} mode, with $-0.0199 \pm 0.0012 \text{ cm}^{-1}/K$ for 1L and $-0.0160 \pm 0.0014 \text{ cm}^{-1}/K$ for 2L. For the transferred film on SiO₂/Si substrate, originally grown on sapphire by CVD, for the E_{2g}^1 mode, the temperature coefficients were found to be very close to the bulk value as $-0.0217 \pm 0.0017 \text{ cm}^{-1}/K$ for 1L and $-0.0233 \pm 0.0018 \text{ cm}^{-1}/K$ for 2L; but for A_{1g} mode, they increase substantially to $-0.0301 \pm 0.0023 \text{ cm}^{-1}/K$ for 1L and $-0.0310 \pm 0.0018 \text{ cm}^{-1}/K$ for 2L. The substrate effects are most pronounced for the A_{1g} mode, showing as stronger nonlinearity on the temperature shift of the Raman frequency and non-monotonic temperature dependence of the Raman linewidth. Similar or even stronger effects were observed on a mechanically exfoliated 1L film from a bulk single crystal.

To further understand the substrate effect on the MoS₂ films, two cycles of temperature-dependent Raman measurements were performed on the same spot of a transferred MoS₂ monolayer on SiO₂/Si substrate. In the first cycle of annealing, both E_{2g}^1 and A_{1g} modes show the similar temperature dependence as other transferred samples studied earlier, including A_{1g} exhibits extremely nonlinear dependence. Whereas, after the second cycle the temperature dependence becomes more linear with respect to that in the first cycle. In contrary to A_{1g} mode, the temperature dependence of E_{2g}^1 mode in both annealing cycles is quite linear. By comparing the mapping data before and after annealing, evident changes of the film morphology has been observed, which is due to the thermal expansion coefficient difference between monolayer MoS₂ and substrate.

These results suggest that for the mechanically transferred thin film, due to the mismatch in thermal expansion between the film and substrate, the temperature change can lead to significant changes in the thin-film morphology as a result of realignment of the film on the substrate, which can be most easily probed by the temperature dependence of the A_{1g} mode associated with the out-of-plane atomic vibration. Temperature dependent Raman study provides an efficient tool for investigating the coupling between the 2D material and substrate either with chemical or mechanical bonding.

Based on the analyses on the results of different samples, we suggest that the most accurate linear Raman temperature coefficients for a hypothetical free-standing monolayer MoS₂ should be: for the E_{2g}^1 mode, $-0.0217 \pm 0.0017 \text{ cm}^{-1}/K$, obtained from a transferred CVD sample; and for the A_{1g} mode, $-0.0199 \pm 0.0012 \text{ cm}^{-1}/K$, obtained from an as-grown CVD sample on sapphire, which is supported by $-0.0198 \pm 0.0014 \text{ cm}^{-1}/K$, obtained by a transferred CVD sample after annealing. These values are practically the same as the bulk values within the error bars.

CHAPTER 5: TEMPERATURE DEPENDENCE OF RAMAN AND PL IN MONOLAYER WS₂

5.1 Fabrication and Characterization of WS₂ Samples

5.1.1 Sample Fabrication

The techniques of growing large-area single crystalline monolayer WS₂ film and transferring it onto a secondary substrate make the investigation of temperature dependent Raman scattering of monolayer WS₂ possible. Five samples were prepared by both mechanical exfoliation and chemical vapor deposition: (a) “1L-SiO₂” is a monolayer WS₂ film grown on Si substrate coated with 300 nm SiO₂; (b) “1L-SA-TRF” is a triangular-shaped monolayer WS₂ film, grown on sapphire substrate; (c) “1L-SA-FILM” is a large area monolayer WS₂ film grown on sapphire substrate; (d) “1L-TRAN-SiO₂” is a transferred monolayer WS₂ film originally grown on sapphire and then transferred onto SiO₂/Si substrate; (e) “Bulk-SiO₂” is a thick layer of WS₂ (> 20 layers) on the same SiO₂/Si substrate as “1L-SiO₂”. All samples were prepared by our collaborators at NCSU. Figure 5.1 shows the optical images of the five samples (the “bulk” sample is on the same substrate as “1L-SiO₂”).

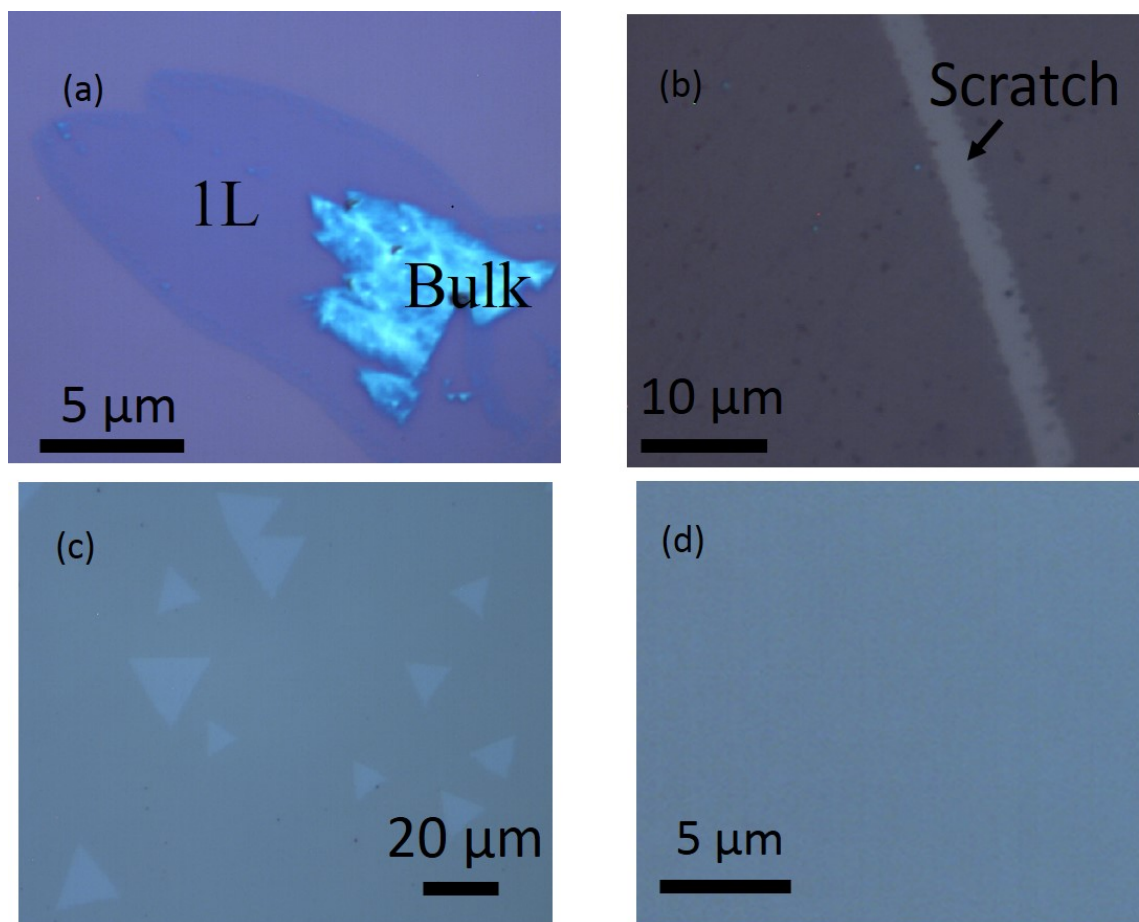


Figure 5.1: The optical images of monolayer WS_2 samples. (a) CVD-grown monolayer WS_2 on $\text{SiO}_2/\text{Si} - 1\text{L-SiO}_2$ accompanied by bulk MoS_2 - “bulk”- SiO_2 . (b) CVD-grown monolayer WS_2 transferred onto $\text{SiO}_2/\text{Si} - 1\text{L-TRAN-SiO}_2$. (c) CVD-grown monolayer WS_2 triangles on sapphire - 1L-SA-TRI. (d) CVD-grown monolayer WS_2 film on sapphire - 1L-SA-FILM.

5.1.2 Characterization of WS_2 samples

To determine the thickness of WS_2 films, an AFM image is shown in Figure 5.2a confirming that the thickness is ~ 0.7 nm, i.e., monolayer. Similar to MoS_2 , Raman spectroscopy, as a nondestructive and powerful technique, can be used to determine the layer number of WS_2 thin films. Bulk WS_2 studied here has the same crystal structure as MoS_2 studied in the previous chapter, and belongs to the same point group symmetry of $D3h$. Figure 5.2b shows the Raman spectra of all the five samples,

measured by 441.6 nm laser excitation ($\sim 150 \mu W$). Two major peaks, E_{2g}^1 and A_{1g} , are observed, which correspond to the in-plane and out-of-plane vibration modes (the inset of Figure 5.2b). The E_{2g}^1 mode involves the in-plane motion of W + S atoms and A_{1g} the out-of-plane motion of two S atoms. For monolayer WS_2 , their values are $\sim 355 \text{ cm}^{-1}$ and $\sim 417 \text{ cm}^{-1}$, respectively [126]. The frequency difference between these two modes has been shown to be a simple signature to determine the layer number of WS_2 . In Figure 5.2b, the frequency difference between E_{2g}^1 and A_{1g} modes is 61.7 cm^{-1} for 1L- SiO_2 , and 65 cm^{-1} for “bulk” WS_2 . Note that the E_{2g}^1 frequency of the bulk is overall lower than that of monolayer samples, while A_{1g} higher. This is due to the interlayer interactions same as MoS_2 . Within the monolayer samples, the variation of the frequencies of both E_{2g}^1 and A_{1g} modes is an effect of the substrate (i.e. strain) and doping. More discussions will be given in the next section. When using near-resonant 532 nm laser excitation, very rich Raman features appear, in particular a very strong second-order peak 2LA(M) sitting close to E_{2g}^1 peak, as shown in Figure 5.2c. A Lorentzian fitting procedure is applied to deconvolute 2LA(M) and E_{2g}^1 components.

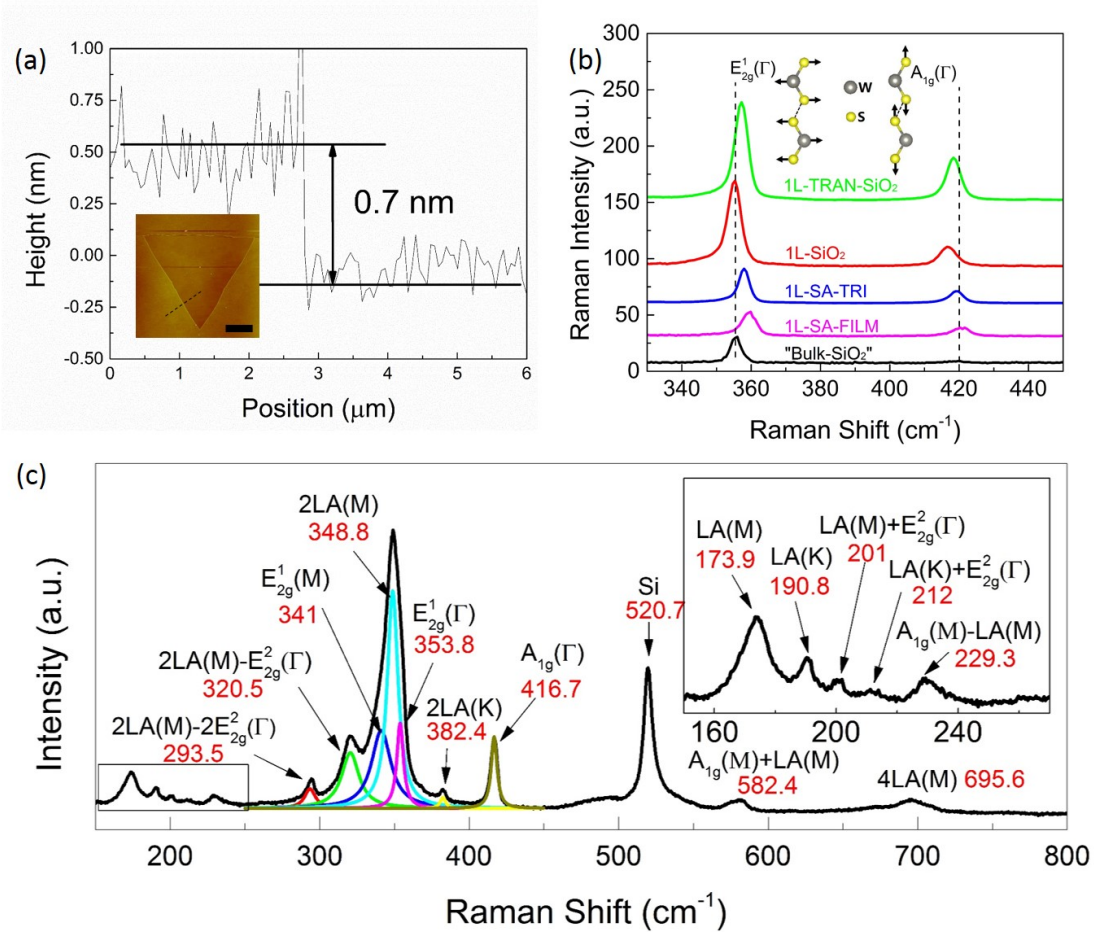


Figure 5.2: The characterizations of all WS₂ samples. (a) The AFM image of 1L WS₂ triangle on sapphire (1L-SA-TRI) showing the thickness is ~ 0.7 nm. (b) Raman spectra of all the WS₂ samples collected with 441.6 nm laser. The inset shows the atomic displacements for the two major Raman modes E_{2g}^1 and A_{1g} . (c) A Raman spectrum collected with 532 nm laser.

Figure 5.3 shows the comparison of Raman spectra under both 532 nm and 441.6 nm laser excitation for all the four monolayer samples as well as the “bulk” WS₂. Under 441.6 nm excitation, the two on-sapphire samples show comparable Raman intensities, whereas the 1L-SiO₂ sample shows lower signal by a factor of 2-3, but the transferred sample 1L-TRAN-SiO₂ has the strongest signal, ~ 3 times of the on-sapphire samples. Under 532 nm excitation, the most striking observation from comparing the four 1L samples lies in that that signals of the on-SiO₂ samples, both

as-grown and transferred, are substantially stronger than those of the other two on-sapphire samples, in particular the 1L-SiO₂ is stronger by over a factor of 10-20, and 1L-TRAN-SiO₂ by a factor of 3-5. Comparing the three as-grown samples, we observe an anti-correlation between the resonant and off-resonant signals, i.e., stronger resonant signal under 532 nm excitation corresponding to weaker off-resonant signal under 442 nm excitation. The transferred film on SiO₂ shows the strongest off-resonant signal, about 10 times of the as-grown sample on the same type of substrate, but about a factor of 3 weaker under near resonant excitation. Clearly, it is not possible to explain the variations among these samples simply by the variations in sample quality. These comparisons offer the first indication of the substrate as well as film-substrate bonding dependence of the 2D-WS₂ film, and more than one mechanisms at work for these substrate effects. The relative intensities of different samples at the two excitation wavelengths are summarized in Table 5.1.

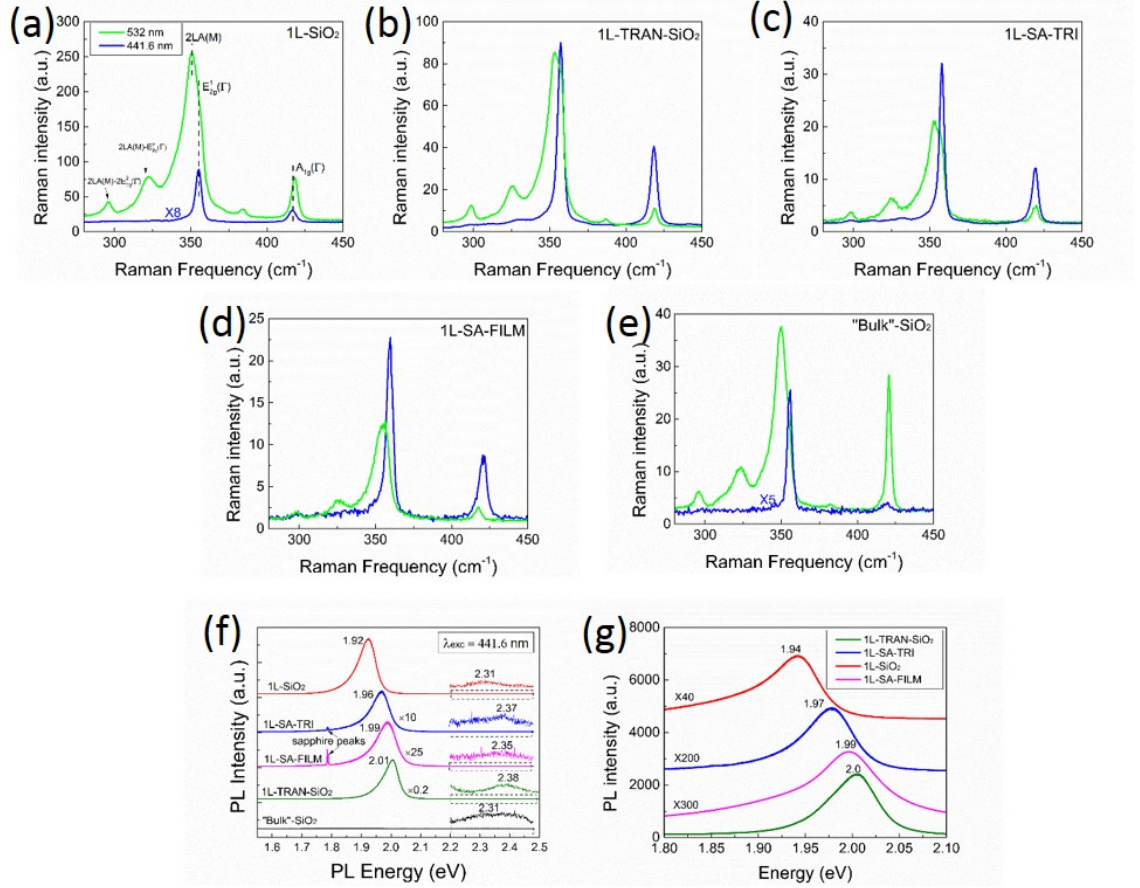


Figure 5.3: The comparison of Raman spectra collected with 441.6 nm and 532 nm lasers. (a)-(f) Raman and PL of all five WS₂ samples with excitation wavelengths of 441.6 nm (blue line) and 532 nm (green line). (f)-(g) PL with (f) 441.6 nm and (g) 532 nm excitation.

Table 5.1: Relative intensities of Raman and PL of four monolayer WS₂ samples measured by two excitation wavelengths: 532 nm and 441.6 nm. For each column, the weakest intensity serves as unity reference.

	532 nm		441.6 nm	
	Raman	PL	Raman	PL
1L-SiO ₂	20	7.5	1.0	25
1L-TRAN-SiO ₂	7.3	300	10	125
1L-SA-TRI	1.7	1.5	3.3	2.5
1L-SA-FILM	1.0	1.0	2.3	1.0

Figure 5.3f-g shows PL spectra of all the WS₂ samples measured with 441.6 and 532 nm laser. Monolayer WS₂ has two interband transitions near the bulk direct transitions at the *K* point due to spin-orbit splitting of the valence band, assigned as A exciton (~ 2.0 eV) and B exciton (~ 2.38 eV). The variation of the PL peak position is likely due to the strain effect which is introduced during growth process. The PL intensity of 1L-TRAN-SiO₂ is much stronger than 1L-SiO₂ by approximately a factor of 5, which is opposite to the relative intensity in Raman where 1L-SiO₂ is much stronger. The small bandgap shift should not significantly affect PL intensity, because of typically weak variation of absorption strength with wavelength. There are two known major effects influencing the intensity of band edge PL emission: (1) doping, and (2) optical interference effect. The stronger bonding for the as-grown sample seems to quench the PL relative to the transferred sample with weaker bonding to the otherwise same SiO₂ substrate. However, the PL intensities of the on-SiO₂ samples are in general much stronger than the on-sapphire samples, for instance, by as much as 125 times between 1L-TRAN-SiO₂ and 1L-SA-FILM. The major PL intensity reduction for the on-sapphire samples could be due to non-radiative recombination via substrate. Additionally, the interference effect of the thin-layer SiO₂ could slightly enhance the light absorbed by the WS₂ film and the collection efficiency. The relative PL intensities are summarized in Table 5.1. In short, the SiO₂ substrate seems to offer much stronger PL than sapphire substrate for either excitation wavelength. These observations illustrate the fact that the film-substrate interaction could be rather complex.

The great enhancement of Raman intensity, especially 2LA(M), can be explained by the resonant Raman effect. The B-exciton energy, ~ 2.35 eV, is very close to the energy of green laser that is 2.33 eV. In this case, resonant Raman occurs, which can

be described by the equation below [127]:

$$I(E_L) = K \left| \frac{\langle f | H_{e-r} | b \rangle \langle b | H_{e-ph} | a \rangle \langle a | H_{e-r} | i \rangle}{(E_L - E_g - i\Gamma_a)(E_L - E_{ph} - E_g - i\Gamma_b)} \right|^2, \quad (5.1)$$

where $I(E_L)$ is the Raman scattering intensity, and K is a constant; $\langle i \rangle$ is the initial state, $\langle a \rangle$ and $\langle b \rangle$ are two intermediate states, $\langle f \rangle$ is the final state; H_{e-r} and H_{e-ph} are the Hamiltonians of the radiation of the light and the electron-phonon coupling, respectively; E_L is the energy of the incident light, E_g is the energy of the electronic transition, and E_{ph} is the phonon energy; Γ_a and Γ_b are the damping constants related to the lifetimes of the two intermediate states $\langle a \rangle$ and $\langle b \rangle$, respectively. The first term in the denominator of Eq.(5.1) reflects the resonance of the incoming photon with the B exciton transition energy, the second term of the outgoing photon involving the phonon energy. The B-exciton PL emission energy of 1L-SiO₂ at 2.31 eV is the closest to the laser energy among the four 1L samples. The strongest resonant Raman signal from this sample suggests that the incoming electronic resonant plays the dominant role. The resonant effect was shown to become progressively weaker with reducing the excitation wavelength. Although between the two on-SiO₂ samples the Raman intensity difference under 532 nm excitation could be explained by the difference in proximity to the resonance condition due to the B exciton energy level difference (2.31 vs. 2.38 eV), the Raman intensity difference under 441.6 nm could be caused by another mechanism that is yet to be determined. One possibility could be the difference in charge transfer or doping related to the difference in the film/substrate bonding.

5.2 Temperature Dependence of Raman Scattering

The temperature dependent Raman study was reported for a 1L mechanically exfoliated (ME) WS₂ from 77 to 623 K with the temperature coefficients of both E_{2g}^1 and A_{1g} modes being $-0.006\text{cm}^{-1}/\text{K}$, although the data were apparently nonlinear in temperature. The high temperature Raman studies were carried out for the four 1L WS₂ samples as well as “bulk” WS₂ from RT to 500 °C. Figure 5.4a shows the temperature dependent Raman spectra of 1L-SiO₂. For both E_{2g}^1 and A_{1g} modes, the Raman frequency decreases with increasing temperature. In addition, the intensity of 2LA(M) decreases drastically as the temperature rises, because the bandgap redshift detunes the laser energy from resonance. Empirically, the temperature dependence of Raman shift, same as MoS₂, can be described by Eq.(3.1). It is noted that for both sapphire samples, one of sapphire Raman peaks at 417 cm⁻¹ overlaps with WS₂ A_{1g} peak. Thus, the spectrum of the sapphire substrate was taken at each temperature and carefully subtracted to yield the WS₂ Raman spectrum, as illustrated in Figure 5.5.

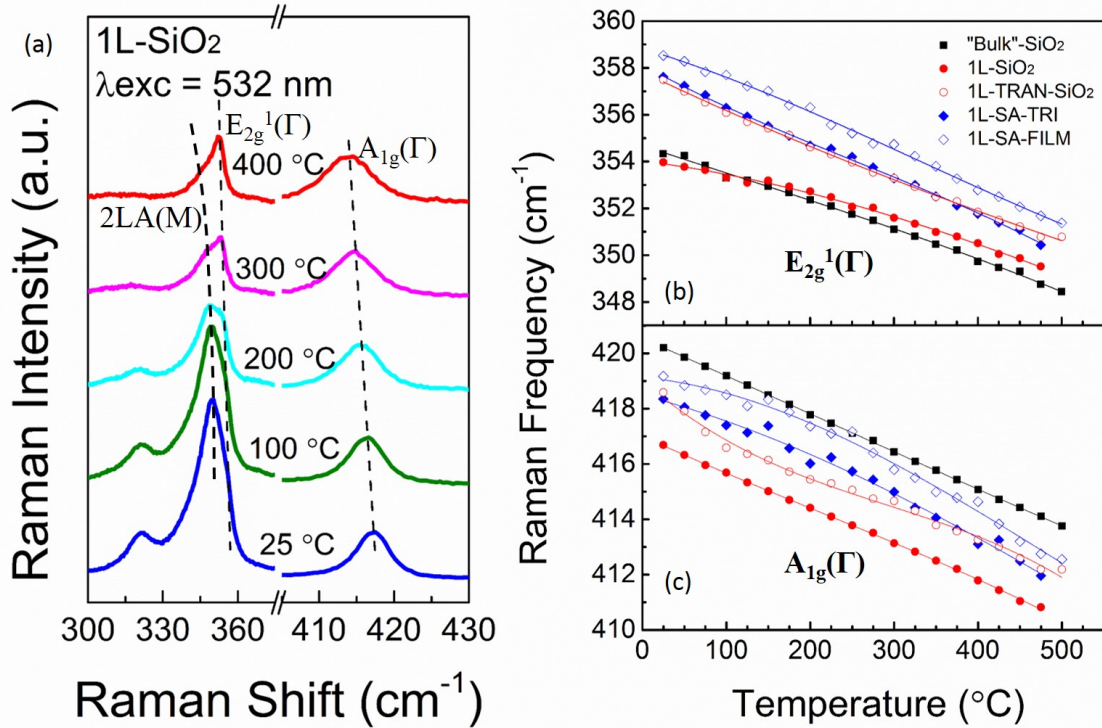


Figure 5.4: Temperature dependence of Raman spectroscopy of all the WS₂ samples. (a) Representative Raman spectra of 1L-SiO₂ sample at different temperatures. (b)-(c) Temperature dependence of Raman frequencies of (b) E_{2g}¹(Γ) and (c) A_{1g}(Γ) modes in “bulk” and 1L samples. The solid lines are fitting results using Eq.(4.1).

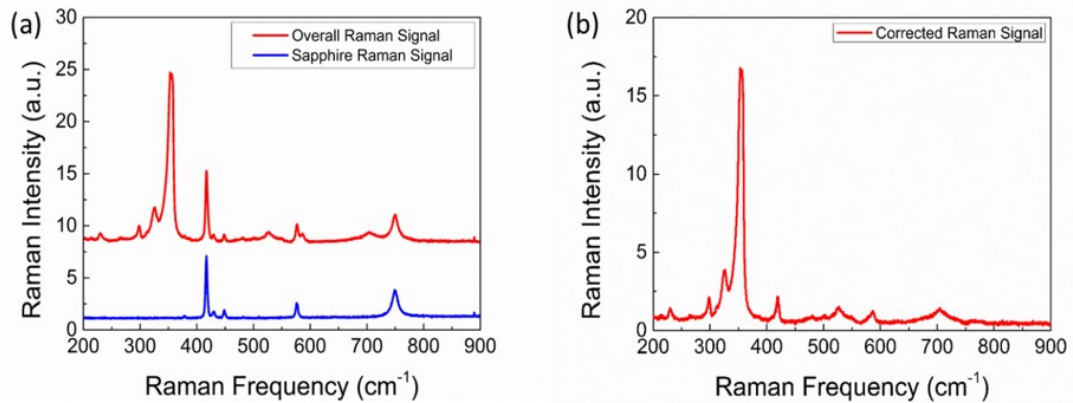


Figure 5.5: The baseline correction of Raman signal from WS₂ monolayer on sapphire. (a) Measured Raman spectra from 1L-SA-TRI (red) and sapphire substrate (blue), respectively, at room temperature. (b) Corrected Raman signal by subtracting Raman signal of sapphire from the overall Raman signal.

The change in Raman frequency ($\Delta\omega$) of WS₂ samples with increasing tempera-

ture can be expressed by Eq.(4.2) with the three contributions from $\Delta\omega_E$, $\Delta\omega_A$ and $\Delta\omega_M$. Figure 5.4 shows the temperature dependence of Raman frequency for both E_{2g}^1 and A_{1g} modes in all the five samples. As a rough practice, one could consider both E_{2g}^1 and A_{1g} exhibiting linear redshifts with increasing temperature. However, the clearly observable differences in slope among the samples and the subtle non-linearity reflect the intricate film-substrate interaction.

For E_{2g}^1 , the study on MoS₂ in the previous chapter indicates that the transferred sample shows the least substrate effect on this in-plane mode. Thus, we may take 1L-TRAN-SiO₂ as an approximate reference for a free-standing 1L WS₂. In fact, as shown in Figure 5.4b, the temperature dependence of this sample is very similar to the strain free bulk MoS₂, showing a weak non-linear effect at high temperature. Other than the small variations in frequency, the temperature shifts of the two on-sapphire samples are very similar to that of the 1L-TRAN-SiO₂, indicating relatively small strain in the epitaxial film and weak bonding to the substrate. However, the slopes for the two as-grown samples on SiO₂ are substantially smaller than that of 1L-TRAN-SiO₂. As suggested by the RT-PL data mentioned above, 1L-SiO₂ is under significant tensile strain at RT, manifesting as the lowest Raman frequency among all the samples. Thus, the third term in Eq.(4.2) becomes significant. The TEC of WS₂ is about one order of magnitude higher than that of SiO₂. With increasing temperature, the WS₂ film expands faster than SiO₂, which in turn results in a release of tensile strain in the WS₂ film. The strain release gives rise to a blue shift that compensates the intrinsic red shift given by the first and the second terms in Eq.(4.2), resulting in an apparent smaller temperature coefficient than 1L-TRAN-SiO₂ and sapphire samples. This is also largely true for the thicker sample, “bulk”-SiO₂, because it is not thick enough to allow the WS₂ to fully relax at RT, which explains why its temperature coefficient is higher than that of 1L-SiO₂ but lower than the other samples. However, for 1L-SA-TRI and 1L-SA-FILM, because the difference of TEC’s between sapphire

and WS_2 is relatively small, no significant strain is generated in the films when cooled down to RT.

For A_{1g} , the previous study on MoS_2 indicates that this out-of-plane mode is particularly sensitive to the morphology of the film (e.g., mesoscopic scale mechanical buckling and chemical residues associated with the transferred film), and very strong non-linearity was observed for the transferred film. As shown Figure 5.4c, the strongest non-linearity is observed for the transferred film 1L-TRAN- SiO_2 , although not as drastic as reported for a ME MoS_2 film on SiO_2 . The two as-grown samples on SiO_2 exhibit rather good linearity and with very close slopes. Because the strain induced frequency shift is much smaller for A_{1g} ($-1.7\text{cm}^{-1}/\%$ from the DFT calculation) than E_{2g}^1 , the release of the tensile strain with increasing temperature partially offsets the intrinsic steeper slope in the initial part, which yields a nice linear dependence for the whole temperature range. Therefore, the intrinsic temperature coefficient for a free standing monolayer or bulk WS_2 is expected to be rather close to (but slightly larger) that of 1L- SiO_2 or “bulk”- SiO_2 , respectively. The results for the two on-sapphire samples are somewhat more perturbed by the substrate than the on- SiO_2 samples. For the transferred sample, increasing temperature improves bonding with the substrate (e.g., through burning out the chemical residues introduced during the film transfer), thus enhances the charge transfer (n-type doping) from the substrate to the film, leading to the phonon frequency red shift. This effect may explain the accelerated red-shift in 1L-TRAN- SiO_2 below 100°C . With increasing temperature further, thermally activated non-radiative recombination, as revealed by temperature dependent PL results (see next section), tends to deplete the carriers, which slows down the red-shift. Above 250°C , the temperature dependence approaches that of a free-standing film. This finding suggests that thermal annealing could have significant impact to electronic mobility of a transferred monolayer TMD film, but not in a simple way. On one hand, it improves the film morphology, which could help the

mobility; on the other hand, it enhances the bonding to the substrate, which could lead to carrier depletion to the substrate or effectively shorten the carrier lifetime, and thus be detrimental to the mobility. This insight might explain some reports suggest that the epitaxial TMD film has lower carrier mobility than the transferred film [128], while reversed observations have also been reported [129]. This observation could provide guidance for identifying the optimal thermal annealing process to achieve desirable properties in device applications. The linear fitting results of the temperature coefficients for all the samples are listed in Table 5.2.

Table 5.2: Temperature coefficients of bulk and 1L WS₂ samples.

	$E_{2g}^1(\text{cm}^{-1}/K)$	$A_{1g}(\text{cm}^{-1}/K)$
“Bulk”-SiO ₂	$-0.0124 \pm 2 \times 10^{-4}$	$-0.0136 \pm 4 \times 10^{-5}$
1L-SiO ₂	$-0.0100 \pm 3 \times 10^{-4}$	$-0.0130 \pm 9 \times 10^{-5}$
1L-TRAN-SiO ₂	$-0.0142 \pm 1 \times 10^{-4}$	$-0.0124 \pm 4 \times 10^{-4}$
1L-SA-TRI	$-0.0154 \pm 3 \times 10^{-4}$	$-0.0140 \pm 3 \times 10^{-4}$
1L-SA-FILM	$-0.0155 \pm 2 \times 10^{-4}$	$-0.0143 \pm 6 \times 10^{-4}$

Finally we note that the integrated Raman intensities for both E_{2g}^1 and A_{1g} modes have been found to decrease dramatically when the temperature $> 475^\circ\text{C}$, presumably due to the decomposition of WS₂ films. Upon returning to room temperature, the films usually cannot return to the initial states. For the 1L-SiO₂ sample, the Raman intensities of the two phonon modes decrease by $\sim 40\%$; however, their peak positions remain almost the same as before, indicating that the bonding between the substrate and film for the CVD-grown samples is fairly robust and not altered significantly by the “annealing” process. For the transferred sample, similar to the transferred MoS₂ films, both Raman intensities and positions showed significant changes, indicating that the heating process modifies the bonding between the film and substrate, and thus the strain distribution over the film. The Raman spectra

before and after temperature-dependent Raman measurements are shown in Figure 5.6.

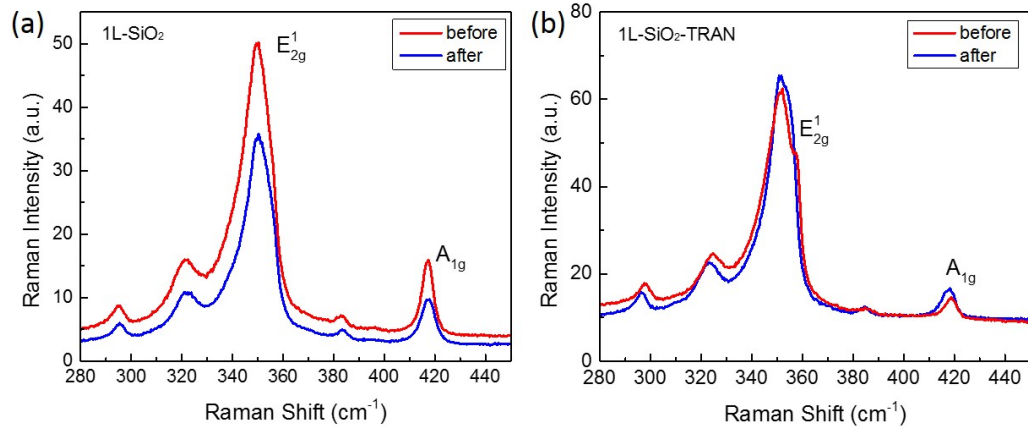


Figure 5.6: The Raman spectra before and after temperature-dependent Raman measurements for samples (a) 1L-SiO₂ and (b) 1L-SiO₂-TRAN.

5.3 Temperature Dependence of PL

The temperature dependence of PL are investigated for 1L-SiO₂ and 1L-SA-TRI samples, with a few representative PL spectra of each shown in Figure 5.7a-b. The peak energies as a function of temperature are plotted in Figure 5.7c. Similar to the trends observed in Figure 5.4b for the Raman shifts of E_{2g}^1 , the PL peak energy shift for 1L-SiO₂ is significantly slower than 1L-SA-TRI, due to the release of the built-in tensile strain for the former. The reduced slope for 1L-SA-TRI at very high temperature (> 300 °C) is due to increasingly significant thermal population of the higher states in the bands. The integrated PL intensities are shown in Figure 5.7d, showing thermal activated temperature quenching, starting approximately from room temperature. For 1L-SA-TRI, the well-known emission of Cd³⁺ centers from the sapphire substrate has been subtracted. Usually, the intensity of PL with increasing temperature can be fitted by Eq.(2.21) with one activation energy, which is suitable

for the SiO₂ sample. However, for the sapphire sample, two activation energies are needed, thus the Eq.(2.21) can be modified as:

$$I(T) = \frac{I_0}{1 + A_1 \exp(-E_{a1}/k_B T) + A_2 \exp(-E_{a2}/k_B T)}, \quad (5.2)$$

where E_{a1} and E_{a2} are the activation energies of the thermal quenching processes, and A_1 and A_2 are constants. For the SiO₂ sample, $A_2 = 0$. The fitting results are: for 1L-SiO₂, $E_{a1} = 0.40 \pm 0.01$ eV; for 1L-SA-TRI, $E_{a1} = 0.20 \pm 0.01$ eV and $E_{a2} = 1.51 \pm 0.06$ eV, respectively, with the fitting curves shown in Figure 5.7d. Temperature induced PL quenching in semiconductors is typically resulting from direct or indirect thermally activated non-radiative recombination processes associated with defects or impurities through emission of phonons. Activation energies as large as these values are unusual, which is largely because PL study is rarely performed in the temperature range much higher than RT to assess the potential process with such a large activation energy. At this stage, our understanding about defects and impurities in these 2D materials is very limited, thus, speculating the physical origins of these thermal quenching processes is premature. However, we would like to point out an important issue that could be particularly important to the 2D materials, that is, the interfacial effect involving carrier exchange between the 2D film and substrate through a thermal activation process. In fact, the magnitudes of the activation energies are comparable to the possible energy barriers between the film and substrate. Theoretical modeling based on first-principles techniques is needed to understand the film-substrate interaction that has yielded the effects reported here for electronic and vibration properties of the 2D materials.

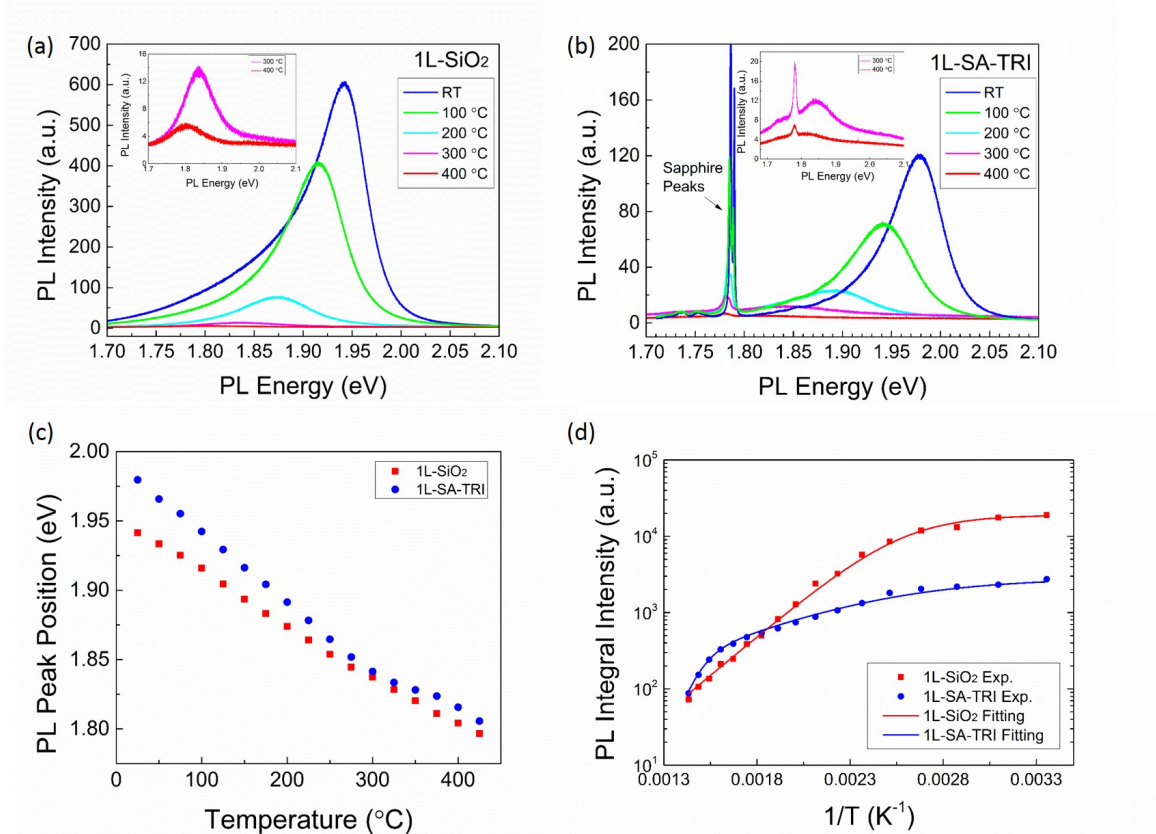


Figure 5.7: Temperature dependence of PL. (a)-(b) Representative PL spectra of (a) 1L-SiO₂ and (b) 1L-SA-TRI at particular temperatures. (c) Temperature dependence of PL peak energy for 1L-SiO₂ and 1L-SA-TRI samples. (d) Integral PL intensity of 1L-SiO₂ and 1L-SA-TRI at different temperatures.

5.4 Spatial Resolved Study on As-grown Monolayer WS₂ Triangles

In general, strain and doping are the two major causes to tune the optical properties of WS₂ monolayer, reflecting as the variation of Raman and PL spectroscopy. However, the origin of the induced strain and doping is most likely due to the growth and transfer processes. Similar to graphene, for transferred WS₂ samples, the transfer process introduces polymeric residues on top of the films, which can significantly dope the films, and hence modify the electronic properties. For CVD-grown samples, the quality of monolayer WS₂ depends on the precise control of growth conditions such as pressure, temperature, precursors, cooling rate and so on. Generally speaking, the

CVD-grown samples are more defective than ME samples. The defects from growth process are another origin of doping. Furthermore, the interaction of monolayer WS_2 with the substrates, such as strain and charge transfer, plays a very important role in the optical properties of WS_2 monolayer as well.

WS_2 monolayers were originally synthesized on sapphire by CVD with the sulfurization of WO_3 precursors at a temperature of $\sim 300^\circ\text{C}$, involving the expanding and thinning of WS_{2+x} flakes and eventually forming large monolayer WS_2 triangles (in the order of $10\ \mu\text{m}$). One can envision that the sulfurization process varies dramatically within the mostly monolayer triangle, because the growth time varies over the triangle where the center area is longer while the edge shorter. Thus, the value of x may differ from one area to another, which can be either positive or negative. As a result, this could cause defects and structural deformation over the triangle. Moreover, it is reasonable to believe that the chemical bonding between the WS_2 film and substrate at the center area is stronger than that at the edge, because the growth or reaction time at the center area is longer. This spatial variation of the bonding strength can be the cause of non-uniform strain distribution over the triangle as well as doping concentration.

Figure 5.8 presents high spatial resolution Raman and PL mapping of the WS_2 triangle shown in Figure 5.1c, using 441.6 nm laser that is off-resonant with the B exciton bandgap to avoid the resonant Raman effect. The Raman mapping data of both E_{2g}^1 and A_{1g} modes show weak intensity variation, less than 10%, over the triangle, with the interior region being stronger (Figure 5.8a-b). In contrast, the PL intensity mapping of the A exciton, as shown in Figure 5.8c, exhibits more significant variations, particularly in the regions near the edges with an average intensity about 10 times of the center. Figure 5.8g shows representative PL spectra from 4 locations (edge, general, center, and apex areas) labelled in Figure 5.8a. They differ not only

in intensity but also in peak energy.

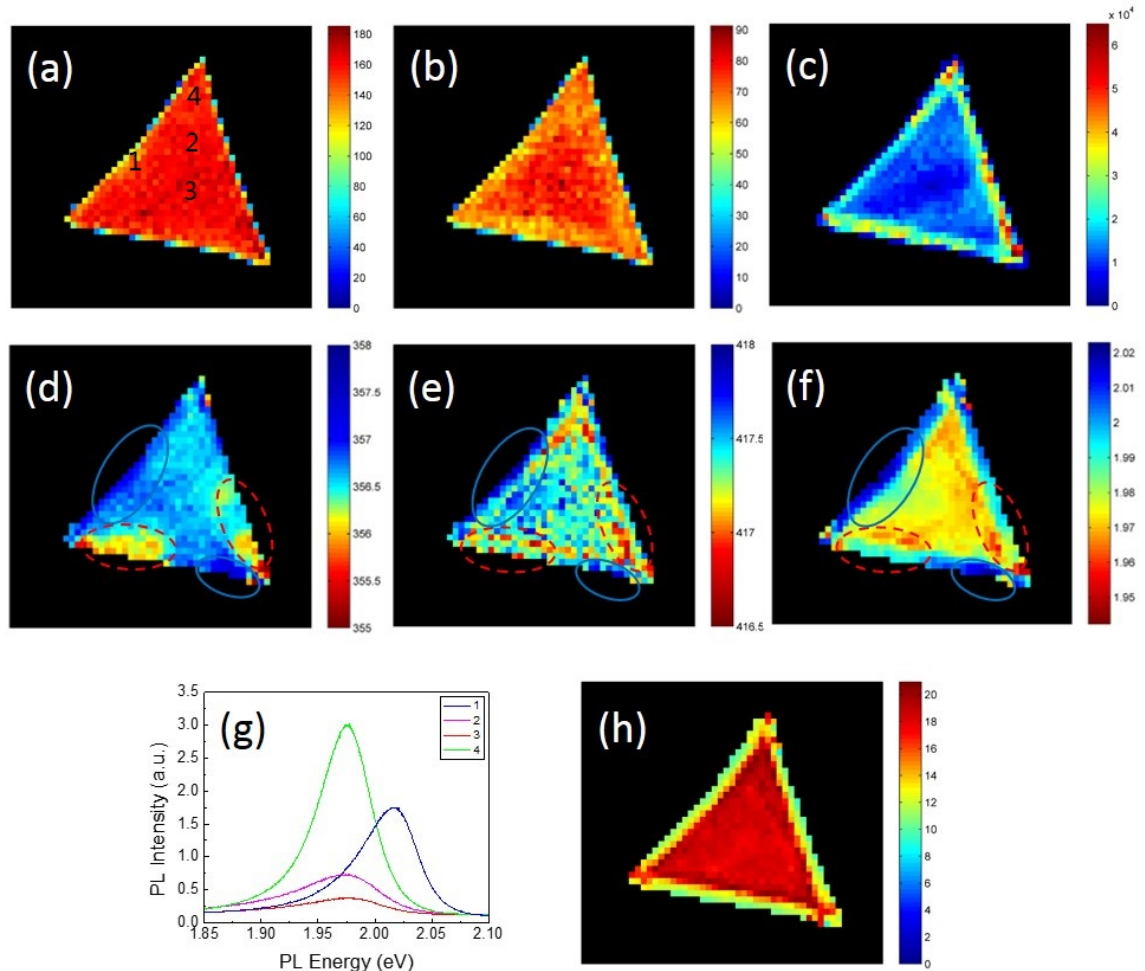


Figure 5.8: The Raman and PL mapping results of the monolayer WS₂ triangle on sapphire. (a)-(c) Intensity maps of (a) E_{2g}^1 mode, (b) A_{1g} mode, and (c) PL of the WS₂ triangle. (d)-(f) Maps of peak position of (d) E_{2g}^1 mode, (e) A_{1g} mode, and (f) PL. (g) PL spectra of locations 1-4. (h) PL width map of the WS₂ triangle.

It is known that strain and doping effects play significant but distinctly different roles on Raman frequencies of E_{2g}^1 and A_{1g} modes. Under tensile strain both modes are expected to show a redshift, but more for E_{2g}^1 mode (i.e., with a larger deformation potential). Meanwhile A_{1g} modes is more sensitive to the doping effect due to the symmetry of conduction band edge state in monolayer WS₂, resulting in stronger electron-phonon coupling and thus more significant redshift or softening of A_{1g} mode.

Figure 5.8d-e show the mapping data for the Raman frequencies of both E_{2g}^1 and A_{1g} modes. The regions with solid blue ellipses exhibit more blueshift than others, while dashed red ones more redshift. By examining the two regions, a maximum frequency difference of E_{2g}^1 is measured to be ~ 2.3 cm-1 and $A_{1g} \sim 1.5$ cm-1. Similar to Raman, PL is susceptible to strain and doping effects as well. The mapping of PL peak position (Figure 5.8f) shows a maximum difference in peak energy of ~ 75 meV.

All these variations in peak positions and intensities of both Raman and PL cannot be explained simply by just one mechanism. However, here we propose that the variations of peak positions over the triangle may primarily arise from the variation in the epitaxial strain that is introduced during growth process. The film grown on sapphire tends to be under tensile strain due to the difference in thermal expansion between the film and the substrate. During the expanding phase of the growth, it is quite possible that the strain distribution over the large triangle will not be uniform due to the geometry of the film and interaction with the substrate. This non-uniform strain, i.e. localized strain, can explain the variations of Raman frequencies of both E_{2g}^1 and A_{1g} modes, as well as the PL peak position.

To estimate quantitatively the strain induced in the film, we carried out density functional theory (DFT) calculations for the strain dependent bandgap and phonon frequencies for uniform strain. The results are shown in Figure 5.9. The deformation potentials for uniform tensile strain are respectively 4.4 cm-1/%, 1.7 cm-1/%, and 140 meV/% for E_{2g}^1 , A_{1g} , and band gap E_g , respectively. Using the calculated deformation potentials and experimentally measured shifts, the values of maximum strain difference over the triangle are estimated from E_{2g}^1 mode to be $\sim 0.53\%$, and from PL $\sim 0.54\%$, which match very well with each other. However, from A_{1g} mode the estimated strain would be $\sim 0.88\%$, implying that strain might not be the only mechanism for the redshift. Therefore, we suggest that the doping effect in the film

might contribute partially to the redshift of A_{1g} .

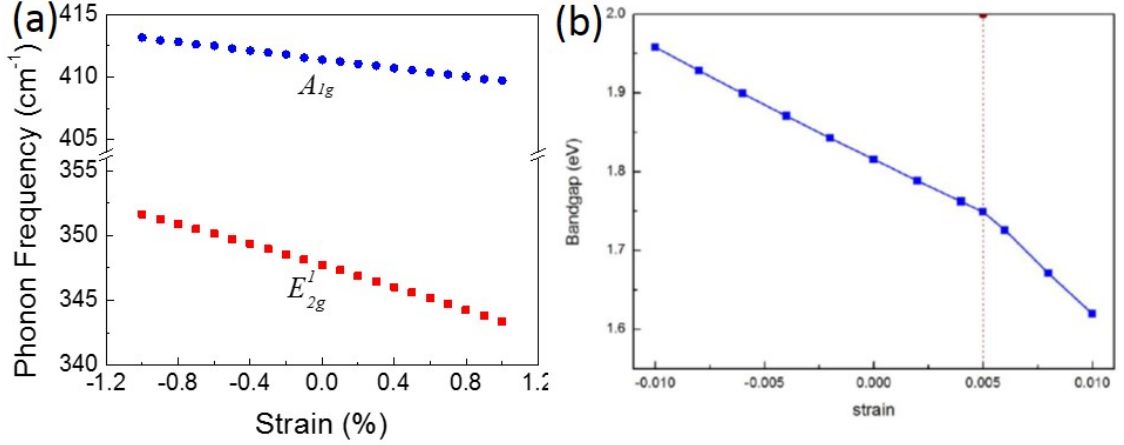


Figure 5.9: DFT calculation of strain-induced Raman and PL shifts. (a) DFT-calculated phonon shift as a function of strain for E_{2g}^1 and A_{1g} modes. (b) The band gap of monolayer WS_2 as a function of uniform strain.

Monolayer TMDs are intrinsically n-type doped due to substrate charge transfer and intrinsic structural defects such as mono-sulfur vacancy (VS) and di-sulfur vacancy (VS2) which are originated from growth process. These sulfur vacancies have been directly observed by scanning transmission electron microscopy (STEM) in monolayer MoS_2 and WS_2 . They are expected to behave as in-gap levels which may quench the band edge PL. The n-type doping caused by shallow donors will lead to the formation of side bands with emission energy lower than that of the neutral exciton and thus the broadening of the overall PL linewidth. However, the distribution of doping concentration over one individual WS_2 triangle is not uniform as a result of the perturbations during the growth process. As we mentioned above, defects are formed during growth, which are mainly sulfur vacancies, and hence n-type doping. Doping or defect, as is known, is one of the origins of PL quenching. In Figure 5.8f, the PL intensities of central area are weaker than those of apex and edge areas. In order to further explain this non-uniform distribution, the spatial variation of the overall PL linewidth is shown in Figure 5.8h, revealing that the linewidth at the edge area

is the smallest over the WS₂ sample. Because a smaller linewidth indicates a lower doping/defect concentration, the linewidth distribution suggests that at the edge area the doping concentration is smaller than the central area. On the other word, the central area is more defective. The better quality, consequently, is one of the reasons of the higher PL intensity at the edge, as shown in Figure 5.8g. Another origin of higher PL intensity at the edge is the less charge transfer between the film and the substrate. On the surface of sapphire, the surface states originating from the Al-O bond terminates and dangling bonds take over, conventionally whose charge density could be very high. Electrons are subjected to be trapped in these surface states, because the Fermi levels of sapphire and WS₂ are supposed to be at the same height in an equilibrium state. Therefore, the photo-generated electrons in PL measurements of WS₂ film will lift up the Fermi level of WS₂, forming a positive potential between the surface states and the WS₂ film. As a result, the electrons tend to escape from WS₂ film to substrate, hence the quenching of PL. Due to the fact that shorter growth time at the edge area results in weaker bonding at the interface between sapphire and WS₂ than those at the central area, it is reasonable to believe that the charge transfer at the edge is weaker, and consequently the radiative recombination rate at the edge is higher or the PL is stronger. In short, besides strain effect to cause the shift of PL peak position, the doping effect from impurities and the charge transfer between substrate and WS₂ film are the reasons to cause the variation of PL quantum yield.

In order to further investigate the effects of strain and doping/defects mentioned above on the properties of WS₂, WS₂ triangles were transferred to a silicon wafer coated with 300 nm thick SiO₂ layer. Holes of different diameters were etched into the wafer. As the optical image is shown in Figure 5.10a, a hole of $\sim 14 \mu\text{m}$ in diameter was covered by a WS₂ triangle. The PL intensity mapping of the WS₂ triangle is shown in Figure 5.10b. The PL intensity of the suspended region is more than that of the supported region by a factor of 2-10. This enhancement cannot

be simply explained by an increase of the optical absorption cross section, because the Raman intensity, which has the optical absorption cross section, shows a small decrease (Figure 5.10f). Figure 5.10c-d shows mapping images of PL peak energy and E_{2g}^1 frequency. Both PL peak energy and E_{2g}^1 frequency at suspended region, in general, exhibit a redshift with respect to those at supported region, suggesting that the suspended WS_2 undergoes tensile strain. The maximum difference of PL energy and E_{2g}^1 frequency between supported and suspended regions is ~ 45 meV and ~ 2.0 cm^{-1} , which correspond to the strain of $\sim 0.34\%$ and $\sim 0.45\%$, respectively. The difference between the two estimated strain values can be due to the doping effect in the film.

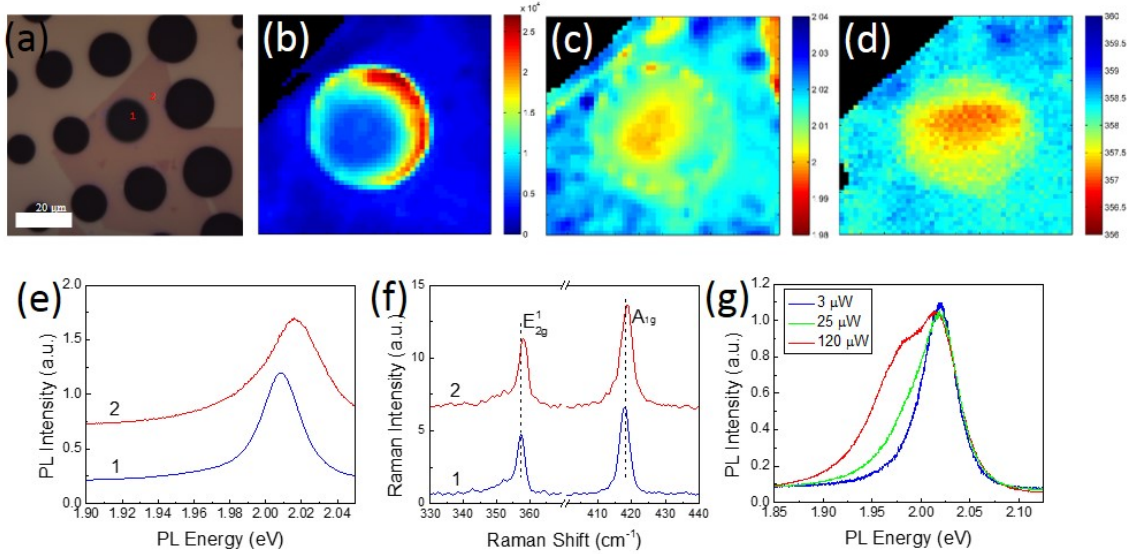


Figure 5.10: The optical characterizations of WS_2 triangles after transferred. (a) Optical image of the transferred WS_2 on SiO_2/Si substrate etched with holes. (b) PL intensity map of an area of $24\mu\text{m} \times 24\mu\text{m}$. (c)-(d) The maps of peak position of (c) PL and (d) E_{2g}^1 mode. (e)-(f) PL and Raman spectra of locations 1 and 2. (g) Laser power dependence of PL.

Figure 5.10e-f show the PL and Raman spectra of locations 1 and 2 labelled in Figure 5.10a. The PL peak energy and the E_{2g}^1 frequency of location 2 are 2.017 eV and 356.8 cm^{-1} , respectively. The PL peak energy difference between locations 1 and 2 is 8 meV, corresponding to a strain difference of 0.06%, while the E_{2g}^1 frequency 0.7

cm⁻¹ to 0.16%. The origin of the discrepancy of strain values could be the doping effect. One source of doping is the intrinsic impurities and the polymeric residues from growth and transfer processes, which could significantly modify the electronic bands of WS₂ monolayer, at either suspended or supported regions. However, at supported region the charge transfer between the film and the substrate becomes more significant than the influence from impurities and residues, leading to the quenching of photo-generated free carriers and hence lower PL intensity. Meanwhile, due to the charge transfer the doping in supported region is higher than that in suspended region, which usually leads to narrowing in band gap energy, i.e. redshift in PL peak energy. Therefore, the real band gap of location 2 can be re-estimated by the strain difference extracted from E_{2g}^1 mode, which is 2.031 eV (610.5 nm). Moreover, a side peak with a lower energy is observed in most PL spectra, which can be assigned as A⁻ trion peak rather than defect or impurity. Because the lower-energy peak increases with increasing power which confirms that this peak is correlated to A⁻, as shown in Figure 5.10(g). The dissociation energy of A⁻ with respect to A can be tuned by varying the power of the 532 nm excitation. With increasing power the trion dissociation energy increases due to the increase in carrier density, i.e. Fermi energy. For the spectra in Figure 5.10(g), the trion dissociation energy is estimated to be ~43 meV at the laser power of 120 μ W, while it decreases with decreasing power, e.g. to ~24 meV at the power of 3 μ W.

5.5 Conclusions

In conclusion, Raman and PL spectroscopies have been used to investigate the interplay of strain, doping and defects of CVD as-grown and transferred CVD-grown WS₂ monolayers. High-temperature PL and Raman studies were also performed on CVD-grown epitaxial monolayer WS₂ on SiO₂/Si and sapphire substrates. The in-

teraction between the 2D film and substrate was shown to depend on substrate type for the as-grown samples and film-substrate bonding between the as-grown and the transferred samples. At RT, the PL intensity of monolayer WS₂ on SiO₂ was found to be much stronger than that on the sapphire substrate under both 532 and 441.6 nm excitation. The TEC mismatch between the thin-film and SiO₂/Si substrate generated a significant amount of strain after the film was cooled down to RT, manifesting itself as a bandgap shift, strong intensity modification in resonant Raman scattering, and large non-linearity in the temperature coefficient of the vibration mode frequency. The effects were minimal for the sapphire substrate. These effects, which are associated with the built-in strain, are inherent properties of the directly grown 2D films. However, this depended upon the specific substrate used. A significant difference existed in the states of the built-in strain between the directly grown and the transferred films, even on the same type of substrate. The in-plane vibration mode, E_{2g}^1 , was more sensitive to the strain effect, whereas the out-of-plane vibration mode, A_{1g} , was more sensitive to the film-substrate bonding or the film morphology. Because of the strong electron-phonon coupling of the A_{1g} mode as dictated by symmetry, a transferred film without proper thermal annealing was expected to have an inferior carrier mobility. The intrinsic temperature coefficients for the E_{2g}^1 and A_{1g} modes in monolayer WS₂ were determined to be: $\chi(E_{2g}^1) = -0.0142 \pm 2 \times 10^{-4} \text{ cm} - 1/K$, derived from the transferred film on SiO₂; and $\chi(A_{1g}) = -0.0130 \pm 9 \times 10^{-5} \text{ cm} - 1/K$ (lower bound), derived from the as-grown film on SiO₂. These values were somewhat smaller than the corresponding ones in MoS₂: $\chi(E_{2g}^1) = -0.0221 \pm 9 \times 10^{-4} \text{ cm} - 1/K$, and $\chi(A_{1g}) = -0.0197 \pm 9 \times 10^{-5} \text{ cm} - 1/K$. For all other cases, the temperature coefficients were affected by the substrate to different extents, but this effect was most severe for the film grown on SiO₂ with $\chi(E_{2g}^1) = -0.0100 \pm 3 \times 10^{-4} \text{ cm} - 1/K$. Therefore, the temperature-dependent Raman investigations provided an effective tool for investigating the epilayer-substrate interaction. Additionally, high-temperature PL

studies on monolayer WS₂ revealed thermal quenching processes with large activation energies of $E_{a1} = 0.40 \text{ eV}$ for the film grown on SiO₂ and $E_{a1} = 0.20 \text{ eV}$ and $E_{a2} = 1.51 \text{ eV}$ for the film grown on sapphire.

With mapping technique of Raman and PL spectroscopy, the strain distribution over the monolayer WS₂ triangle has been examined nondestructively. Through DFT simulation, the maximum difference in strain within a single triangle has been estimated quantitatively to be of $\sim 0.53\%$ based on the shift of E_{2g}^1 mode for CVD-grown WS₂ film on sapphire. The main origin of the strain is the difference in TEC between WS₂ and the supporting sapphire substrate. During the cooling-down process of the growth, this difference of TEC in between introduces the strain to the film, which is observed to be non-uniform. In conjunction with PL mapping, similar maximum strain difference has been estimated to $\sim 0.54\%$ based on the shift of PL peak energy. Besides the strain effect, the effects of both doping and defects, which are from the growth and transfer processes, play significant roles in PL, resulting in the suppression of A-exciton peak for both CVD-grown and transferred WS₂ samples. In particular, the suspended WS₂ film shows more than 10 times stronger PL intensity than the supported WS₂ film, suggesting the involvement of charge transfer between the substrate and the film. Moreover, the A-trion peak accompanied by A-exciton emission has been observed, with a dissociation energy of $\sim 43 \text{ meV}$ at the laser power of $120 \mu\text{W}$.

CHAPTER 6: TEMPERATURE DEPENDENCE OF RAMAN SCATTERING IN THIN-FILM BLACK PHOSPHORUS

6.1 Black Phosphorus Sample Preparation and Its Anisotropic Effects

6.1.1 Sample Preparation and Characterization

High-quality black phosphorus (BP) crystals were purchased from Smart-Elements. BP flakes were obtained by mechanical exfoliation onto a silicon substrate coated with a 300 nm SiO₂ layer. Since BP is very sensitive to ambient environment, the sample was transferred into a heating chamber purging with nitrogen (N₂) gas for temperature dependent Raman measurements. The flow rate of N₂ was low enough not to cause sample cooling. After Raman measurements were finished, tapping mode AFM was carried out to determine the thickness of exfoliated BP flakes. Figure 6.1a-d shows the optical images of four exfoliated samples, labelled as S1-S6. An AFM image containing samples S1 and S2 is also shown in Figure 6.1e, and the thickness of S1 is measured to be ~ 25 nm while that of S2 ~ 10 nm (~ 20 layers). Samples S5 and S6 are in the same flake, but S5 is suspended on a hole etched into SiO₂ substrate. The diameter of the hole is 10 μm . The thickness of samples S5 and S6 is ~ 70 nm, determined by AFM.

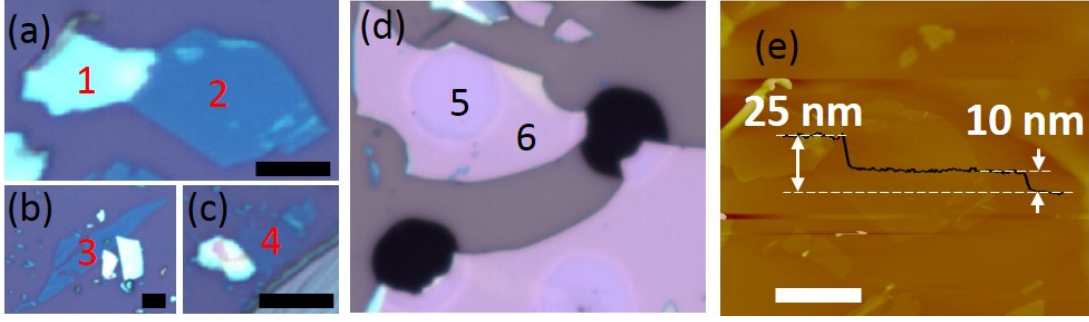


Figure 6.1: Optical images and an AFM image of BP films.

The unit cell of black phosphorus has four phosphorus atoms, and the space group of bulk BP is D2h. There are 12 lattice vibrational modes at Γ point, which can be expressed as following:

$$\Gamma = 2A_g + B_{1g} + B_{2g} + 2B_{3g} + A_{1u} + 2B_{1u} + 2B_{2u} + B_{3u}, \quad (6.1)$$

among which six modes are Raman-active, two A_g (including A_g^1 and A_g^2), one B_{1g} , one B_{2g} , and two B_{3g} . However, only A_g^1 (out-of-plane mode), B_{2g} (in-plane mode along zigzag), and A_g^2 (in-plane mode along armchair) modes can be detected by Raman with back-scattering geometry according to symmetry selection rule (Figure 6.2a). The Raman spectra of S1-S4 samples, measured with the same laser power of $\sim 150 \mu\text{W}$ at room temperature, are shown in Figure 6.2. Three typical Raman peaks corresponding to A_g^1 , B_{2g} , and A_g^2 are observed with their peak positions at ~ 362 , ~ 439 , and $\sim 467 \text{ cm}^{-1}$, respectively. These peaks are fitted with Lorentzian function. According to the intensity of silicon peak at 520 cm^{-1} , we can determine the thickness order of the four samples: $S1 > S2 > S3 > S4$, indicating the thicknesses of S3 and S4 are $< 10 \text{ nm}$. Using the intensities of Si peak, we are able to estimate the thickness of S3 to be $\sim 6 \text{ nm}$ and S4 $\sim 3 \text{ nm}$. The peak position of A_g^2 mode shows a blueshift in frequency with decreasing thickness, while that of A_g^1 mode a redshift, and B_{2g} mode almost no change. This thickness dependence of Raman frequency

in BP is similar to that of TMDs where in-plane mode shows a blueshift and out-of-plane mode redshift, which is attributed to the changes in interlayer interaction with thickness. Interestingly, their Raman intensities do not vary monotonically with thickness, with S2 exhibiting the strongest Raman intensity. This anomalous thickness-dependent behavior can be explained by optical interference with the model used in graphene and MoS₂. The simulated results show that the film of ~ 20 layers exhibits the strongest Raman signal over a thickness range of 1-100 layers, which is in reasonably good agreement with experimental results (Figure 6.2b).

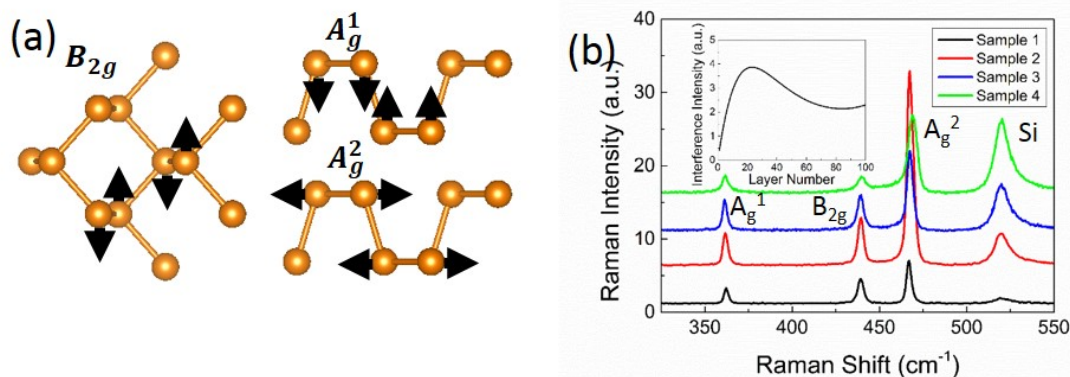


Figure 6.2: Raman spectra of all the BP samples. (a) Three major Raman modes of BP. (b) Raman spectra of all the four BP samples. The inset is a simulation of interference effect as a function of BP thickness.

6.1.2 Anisotropic Effect of Raman Spectroscopy

Due to the puckered honeycomb structure of BP, BP exhibits an unusual anisotropic nature in its multitudinous properties that are expected to show angle-dependence. Among them, angle-resolved polarized Raman spectroscopy is a convenient and non-destructive method to identify the crystalline orientation of BP. According to the symmetry selection rule, only A_g^1 , B_{2g} , and A_g^2 modes can be detected when the incident laser perpendicular to the sample surface. The Raman tensors of these three

modes are listed as following:

$$\mathcal{R}(A_g) = \begin{pmatrix} a & 0 & 0 \\ 0 & b & 0 \\ 0 & 0 & c \end{pmatrix}, \quad \mathcal{R}(B_{2g}) = \begin{pmatrix} 0 & 0 & e \\ 0 & 0 & 0 \\ e & 0 & 0 \end{pmatrix}, \quad (6.2)$$

A_g^1 and A_g^2 modes have the same expression of Raman tensor but with different values of a , b and c . As shown in Figure 6.3a, x and z are the crystal orientation, and e_i and e_s are the polarization vectors of incident laser and scattered light, respectively, which are parallel with each other in our experiment setup. The angle θ that is between the laser polarization vector (e_i) and the armchair direction (z) can be tuned by rotating the sample. The laser is incident along y direction and its polarization is in xz plane. Thus, in the parallel polarization configuration, the vectors e_i and e_s can be written as:

$$e_i = \begin{pmatrix} \sin \theta & 0 & \cos \theta \end{pmatrix}, \quad e_s = \begin{pmatrix} \sin \theta \\ 0 \\ \cos \theta \end{pmatrix}. \quad (6.3)$$

According to Eq.(2.9) the intensity of a given Raman mode, I , is proportional to $|e_i \cdot \mathcal{R} \cdot e_s|^2$; therefore, the Raman intensity of A_g (including A_g^1 and A_g^2) and B_{2g} modes under parallel polarization configuration can be written as:

$$\begin{aligned} I(A_g) &\propto (a \sin^2 \theta + c \cos^2 \theta)^2, \\ I(B_{2g}) &\propto (e \sin^2 2\theta)^2. \end{aligned} \quad (6.4)$$

Apparently, when the armchair direction is parallel to the laser polarization direction ($\theta = 0^\circ$), A_g mode shows local maximum intensities (c^2 or a^2), while B_{2g} mode is forbidden. When $\theta = 45^\circ$, B_{2g} mode reaches its maximum, and over 360° there are four maxima of the same intensity with a period of 90° .

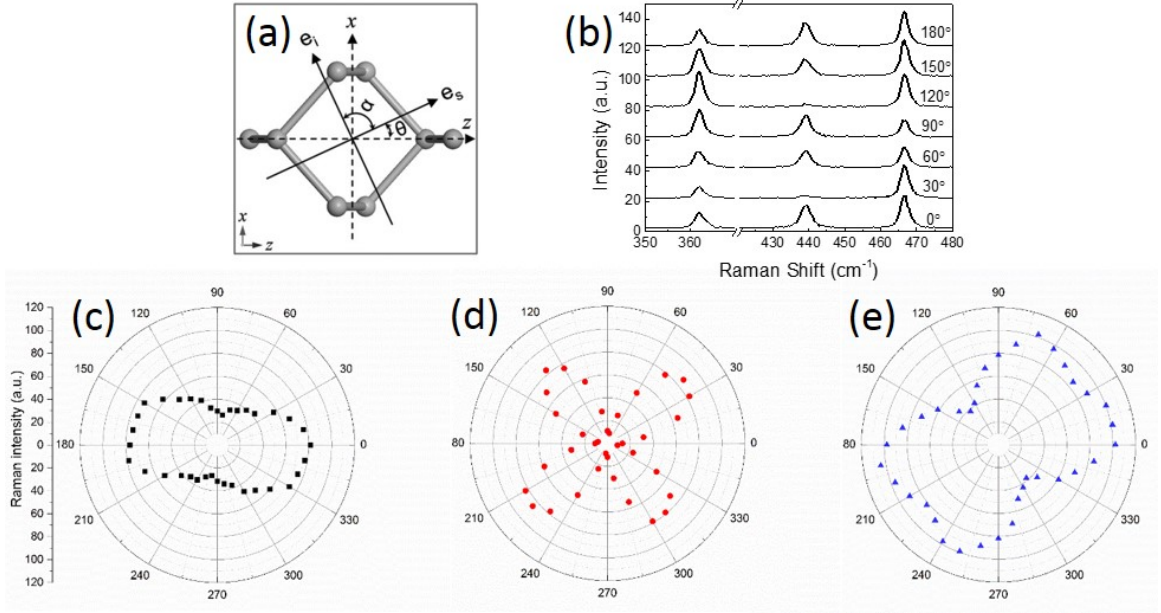


Figure 6.3: Anisotropic nature in Raman spectroscopy of BP. (a) The configuration in the polarized Raman measurements. (b) Representative Raman spectra of BP film with different polarization angle. (c) Polar plots of the Raman intensities for the three Raman modes.

Figure 6.3b shows the polarized Raman spectra of BP samples S5 at different angles of θ from 0° to 180° under parallel polarization configuration. At $\theta = 0^\circ$, both A_g^1 and A_g^2 modes exhibit a maximum intensity while B_{2g} mode is forbidden. The intensity of B_{2g} mode increases and two A_g modes become weaker as θ approaches 45° . After going through 45° , the intensity of B_{2g} mode starts to decrease while those of A_g modes increase and reach second maximum at $\theta = 90^\circ$. This cycle repeats four times as the sample rotates from 0° to 360° . To reveal this behavior, the polar plots of the fitted peak intensities of all the three Raman modes as a function of sample rotation angle θ are shown in Figure 6.3c-e. It can be clearly seen that different Raman modes show different periodic variation of their intensities over 360° rotation. The results match the calculated Raman intensity in Eq.(6.4) quite well. For B_{2g} mode, as expected there are four maxima with same intensity. It is worth noting that, for A_g^2 mode, there are two different local maxima, which is attributed to the different

values of a and c in the Raman tensor. The value of a has been measured greater than that of c , thus the A_g^2 mode reaches a relative smaller local maximum intensity when the x direction (zigzag) is along with the laser polarization direction. When the sample is rotated 90° , where the z direction (armchair) is parallel to the laser polarization direction, a relatively larger local maximum intensity of A_g^2 mode can be obtained. Therefore, with the results of angle-resolved Raman spectroscopy, the optical anisotropic nature of BP has been demonstrated, and most importantly, the crystalline orientation of the sample can be identified rapidly and nondestructively.

6.2 Temperature Dependence of Raman in BP

Temperature dependent Raman measurements were carried out on all the six samples for temperature up to 325°C . With increasing temperature, all Raman modes are expected to show a significant redshift, as shown in Figure 6.4 with representative spectra of S2 and S4 at different temperatures, respectively. The temperature dependence of A_g1 , B_{2g} and A_g2 Raman frequencies are plotted in Figure 6.4a-c, and fitted by Eq.(3.1). As discussed earlier, the change of Raman frequency with temperature can be caused by various anharmonic effects demonstrated by Eq.(4.2).

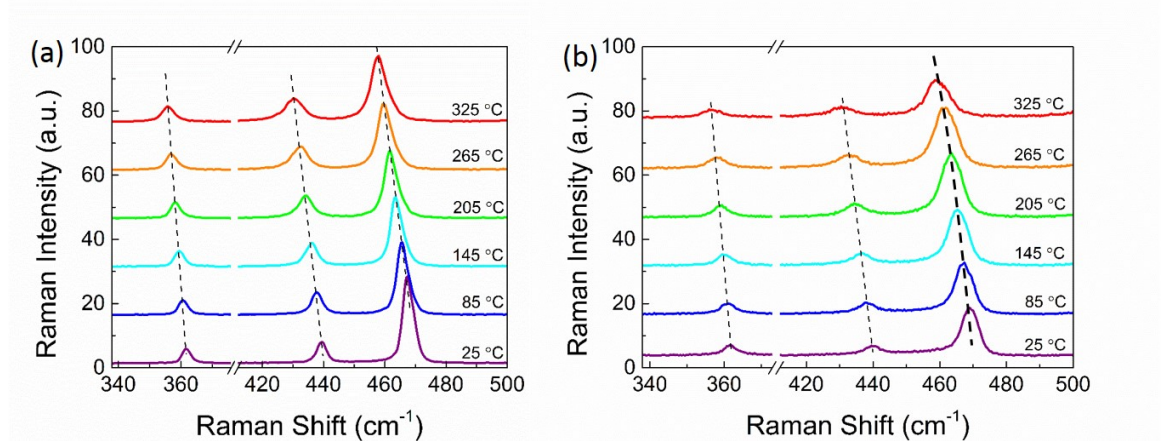


Figure 6.4: Representative Raman spectra for (a) S2 and (b) S4 at different temperatures.

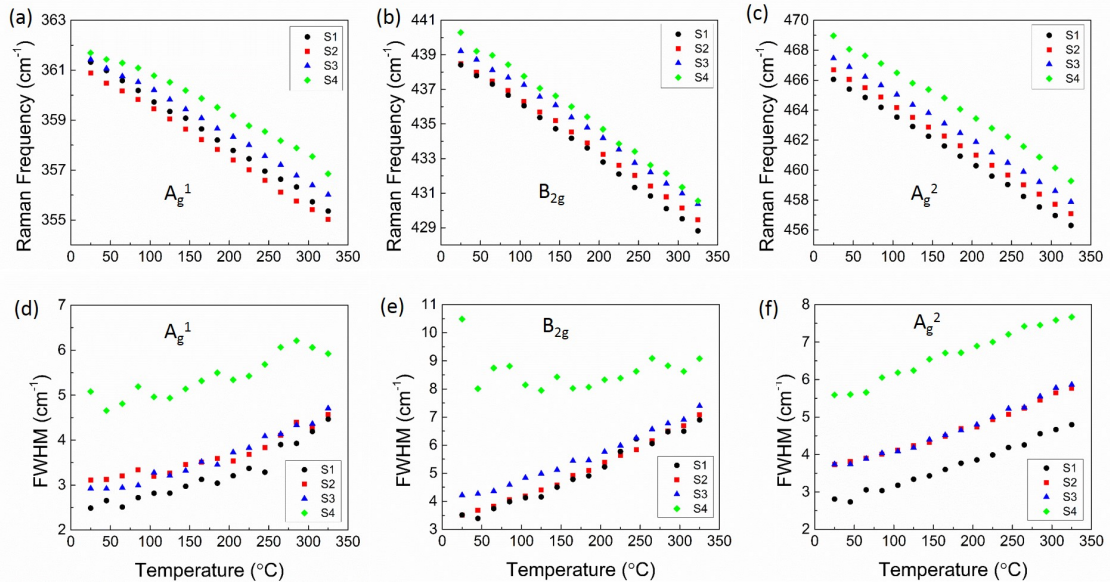


Figure 6.5: Temperature-dependent Raman spectroscopy of all the four BP samples. (a)-(c) Temperature dependences of Raman frequencies of (a) A_g^1 , (b) B_{2g} and (c) A_g^2 modes over a temperature range from RT to 325 °C in samples S1-S4. (d)-(f) Temperature dependences of FWHMs of (d) A_g^1 , (e) B_{2g} and (f) A_g^2 modes in all the four samples.

The temperature coefficients of all the six samples are listed in Table 6.1. Comparing the temperature coefficients of samples S1-S4, the temperature coefficients of all the three modes in general decrease with decreasing thickness. As the thickness decreases, the BP film is more sensitive to its environment, such as substrate, which could lead to modifications of its intrinsic properties. All the four BP samples are held by SiO_2/Si substrate with relatively weak bonding, and the thermal expansion coefficient (TEC) of SiO_2 is much smaller than that of BP. The TEC's of exfoliated BP flakes along armchair and zigzag directions are $93.2 \times 10^{-6}/^\circ\text{C}$ and $90.3 \times 10^{-6}/^\circ\text{C}$, respectively. With increasing temperature, the difference of TEC between the film and the substrate will introduce compressive strain to the film, which effectively reduce the intrinsic thermal expansion of lattice hence the redshift of Raman frequency. With increasing thickness, this effect tends to become weaker. Thus, the thicker film like S1 is less susceptible to the substrate effect, leading to larger temperature coeffi-

cients than other thinner samples. Additionally, it is quite possible that ripples were introduced to BP films during the transfer process, showing a non-planar morphology especially when the film becomes thinner. The morphologic variation of the film, in particular for very thin film, is the main origin of the strain. The non-uniform morphology of the film can affect the temperature dependence significantly on both in-plane and out-of-plane vibrational modes, showing nonlinear temperature dependence. Among the four BP samples, all the three modes of the thinnest sample S4 clearly exhibit stronger nonlinear temperature dependence than the other three samples. The nonlinear temperature dependence of S4 originates from the rearrangement of the film morphology as the strain due to the TEC difference between the film and the substrate changes with increasing temperature. For thicker films, the morphology is expected to be more planar than other samples; thus, the temperature dependence is more linear.

The full width at half maximum (FWHM) of all the three modes increases with increasing temperature as shown in Figure 6.5d-f. At RT, the FWHM increases with decreasing thickness of BP film. For S4, the FWHM is almost double of other three samples. For instance, the FWHM's of S1 and S4 for Ag1 mode are 2.5 and 5.1 cm^{-1} , respectively. This behavior can be explained by the effect related to variation in film morphology as discussed above. On increasing the thickness of the films, the effect of substrate is getting weaker and film morphology more uniform, hence smaller FWHM. For each individual sample, with increasing temperature the FWHM increases. The broadening of Raman peaks typically involves the decay of an optical phonon into two acoustic phonons with the conservations of both momentum and energy. However, the strain induced by the TEC mismatch coupled with the morphology inhomogeneity may also contribute to the broadening of Raman linewidth. It is worth noting that the decomposition of BP films is observed to occur at $\sim 350^\circ\text{C}$ in N_2 environment, manifested as a major reduction in Raman intensity and the sublimation of BP under

visual observation.

Table 6.1: Temperature coefficients of Ag1, B2g and Ag2 modes of samples S1-S4, suspended and supported BP flakes.

	$A_g^1(\text{cm}^{-1}/K)$	$B_{2g}(\text{cm}^{-1}/K)$	$A_g^1(\text{cm}^{-1}/K)$
Sample 1 (25 nm)	-0.0198	-0.0323	-0.0327
Sample 2 (10 nm)	-0.0198	-0.0304	-0.0324
Sample 3 (6 nm)	-0.0182	-0.0300	-0.0320
Sample 4 (3 nm)	-0.0158	-0.0315	-0.0312
Suspended (70 nm)	-0.0220	-0.0344	-0.0349
Supported (70 nm)	-0.0191	-0.0312	-0.0318

6.3 Thermal Conductivity of BP

In order to investigate the influence of substrate effect on temperature dependence, the temperature dependent Raman of S5, which is suspended, is compared to that of S6 that is supported. Figure 6.6a shows Raman spectra collected from the suspended (center of the hole) and supported regions at RT. Two noticeable differences are observed: (1) all the three modes in the suspended region are redshifted compared to supported region, due to heating as a result of lower thermal conductivity; (2) the Raman intensity of suspended region is smaller than that of the supported region, due to an optical interference effect. The temperature dependence of the three Raman modes is shown in Figure 6.6b-d, and the temperature coefficients are listed in Table 6.1. The temperature coefficients of all the three modes in suspended region are greater in magnitude than those in supported region by $\sim 0.003 \text{ cm}^{-1}/K$ ($\sim 10\text{-}15\%$). The difference cannot be explained by the residual laser heating effect, because the additional redshift induced by laser heating will not increase (but likely reduce) with increasing temperature. However, with increasing temperature the supported BP film

experiences compressive strain due to the TEC difference, leading to a blueshift which reduces the redshift caused by heating. For the suspended film, the potential strain caused by the larger thermal expansion of BP could be released through sagging of the film around the edge of the hole, resulting in a nearly strain-free state in the suspended region.

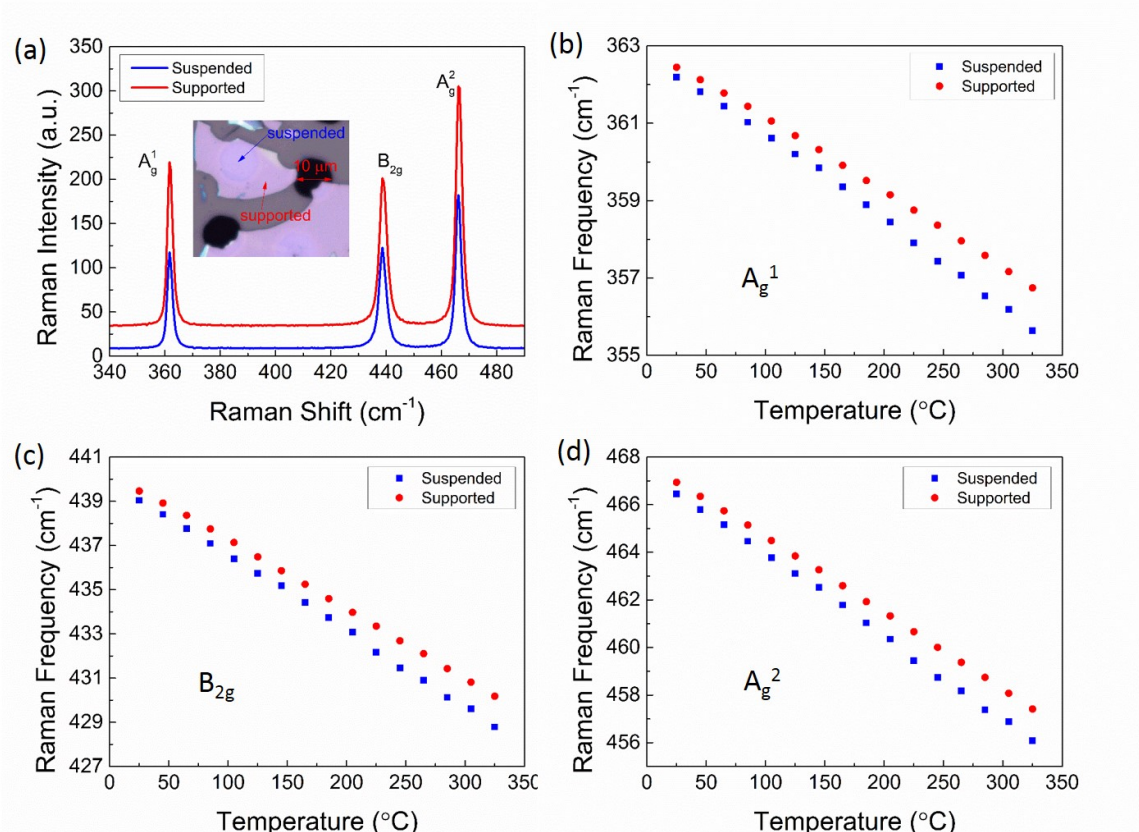


Figure 6.6: Temperature-dependent of Raman spectroscopy of the BP flake in Figure 6.1d. (a) Raman spectra collected from suspended (blue) and supported (red) regions; inset: optical image of suspended BP flake. (b)-(d) Temperature dependences of Raman frequencies of (b) A_g¹, (c) B_{2g} and (d) A_g² modes in suspended and supported regions.

Even though the laser power used is as low as possible not to damage the BP films, it will heat up the sample to cause a temperature rise. Laser power dependent Raman studies are utilized to estimate this temperature rise. The changes in the Raman spectra of suspended BP with different laser powers are shown in Figure

6.7a. With increasing power, the peak positions of all the three modes redshift, indicating the local temperature rises. The frequency shifts are shown in Figure 6.7b-d, exhibiting that the slopes of the suspended region for all the three modes are larger than those of supported region by a factor of ~ 2.2 and the slope $\partial\omega/\partial P$ of A_g^1 mode is much smaller than those of the other two modes. The power used in the temperature-dependent Raman measurements was ~ 0.5 mW, so we can calculate the temperature increase ΔT by the expression: $\Delta T = \Delta P \cdot (\partial\omega/\partial P)/(\partial\omega/\partial T)$, where ΔP is the highest laser power used and $\partial\omega/\partial T$ the temperature coefficient. The temperature increases in suspended and supported regions are estimated to be ~ 22 and ~ 12 °C at $P = 0.5$ mW, respectively.

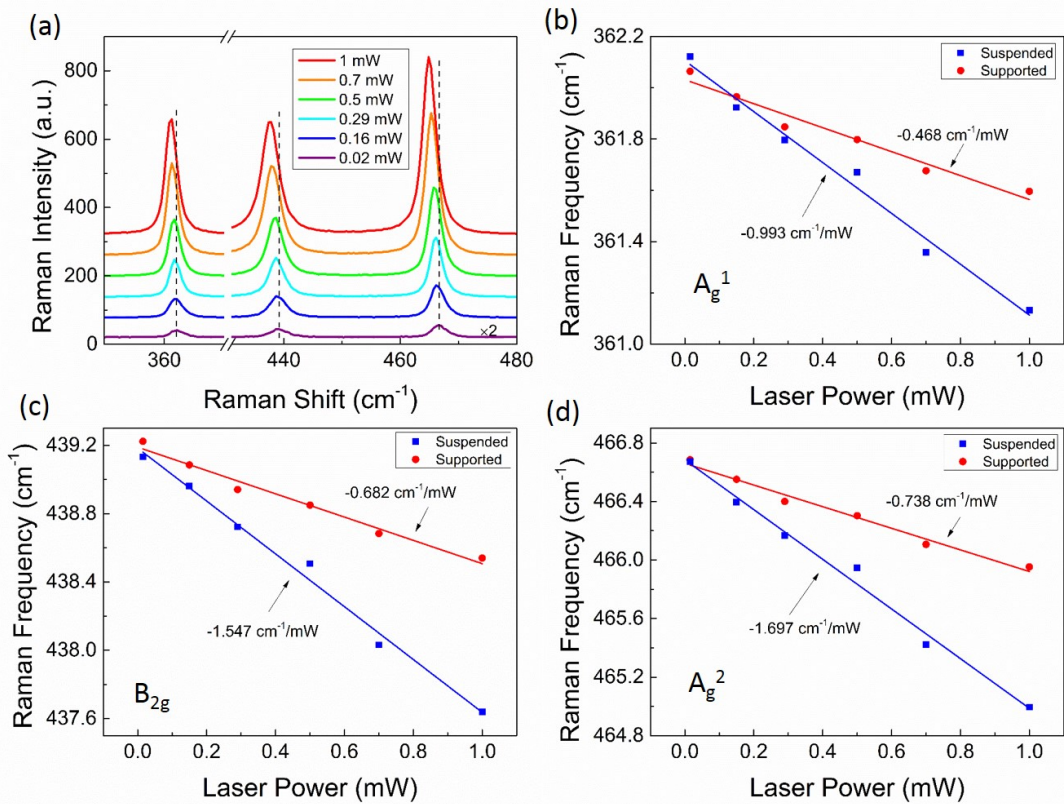


Figure 6.7: Laser power dependence of Raman spectroscopy for the BP flake in Figure 6.1d. (a) Raman spectra collected with different laser powers in suspended region. (b)-(d) Laser power dependences of Raman frequencies of (b) A_g^1 , (c) B_{2g} and (d) A_g^2 modes in suspended (blue) and supported (red) regions, including linear fits of experimental data.

Finally, using the temperature and power dependent results obtained above, we can estimate the average thermal conductivity of BP. Because of the anisotropic nature of BP, the thermal conductivities are expected to be different between the zigzag armchair direction as k_{zig} and k_{arm} , and the average thermal conductivity can be viewed as $k = \sqrt{(k_{zig}k_{arm})}$. Considering the thermal diffusion through an enclosed cylindrical surface in the suspended region, the average thermal conductivity can be evaluated approximately using the formula below that has been developed for 2D materials:

$$k = f\chi \frac{1}{2\pi h} \left(\frac{\partial\omega}{\partial P} \right)^2, \quad (6.5)$$

where χ is the Raman temperature coefficient, h the thickness of the film, and f a reduction factor due to incomplete absorption of laser power. To the first order approximation, $f = g(1 - R)[1 - \exp(-\alpha h)]$, where g , R , and α are interference enhancement factor, reflectance of the BP top surface, and absorption coefficient of BP, respectively, which are all polarization dependent due to anisotropy. The crystalline orientation was determined by analyzing polarized Raman data, and the angle between the laser polarization and the zigzag direction was found to be $\sim 30^\circ$. The absorption coefficients and reflectance values were estimated for 532 nm with polarization in zigzag and armchair directions to be $\sim 5.5 \times 10^4 \text{ cm}^{-1}$ and $\sim 1.6 \times 10^5 \text{ cm}^{-1}$, $\sim 43.5\%$ and $\sim 44.4\%$, respectively. Thus, the f 's are estimated to be 0.23 and 0.21 for suspended and supported BP, respectively. Therefore, for the suspended region, the estimated average thermal conductivities are 16.1, 16.2, and 15.0 W/mK, using the parameters of Ag1, B2g and Ag2, respectively. These values, averaged to $k_{susp} = 15.8 \text{ W/mK}$, are in reasonable agreement with $k_{arm} \sim 20 \text{ W/mK}$, $k_{zig} \sim 40 \text{ W/mK}$ reported for BP thicker than 15 nm. For the supported region, strictly speaking, Eq.(6.5) is not applicable. However, we may treat the substrate effect as a surface modification to the film, and still use the equation to get an effective thermal conductivity. The results are 27.6 (Ag1), 30.9 (B2g), and 29.1 W/mK (Ag2), respectively,

and the average $k_{supp} = 29.2$ W/mK. Although the thermal conductivity of SiO₂, ~ 1.4 W/mK, is much larger than N₂ ~ 0.025 W/mK, it is still much smaller than that of BP. The significant enhancement in thermal conductivity seems to suggest that the supporting substrate plays a more subtle role than merely as a medium with a different thermal conductivity, for instance, the interface charges might significantly affect the thermal conductivity. This higher thermal conductivity at supported region can also explain the smaller temperature rise under high laser power in the supported region compared to suspended region. The obtained thermal conductivities for BP films are comparable to those for TMDs, but significantly smaller than graphene. The observed substrate effect is also applicable to other 2D materials.

6.4 Conclusions

Angle-resolved Raman spectroscopy reflects the anisotropic nature of BP, which can be used as a non-destructive technique to determine the crystalline orientation. Temperature-dependent Raman scattering has been carried out to investigate the temperature effects in thin black phosphorus films with varying thickness prepared by mechanical exfoliation on SiO₂/Si substrate. It has been found that the temperature dependence of the BP thin film is sensitive to the film thickness, showing a decreasing temperature coefficient with decreasing thickness. This behavior is attributed to the interaction of the film with substrate as well as the morphology distortion of the film. By studying a suspended film of 70 nm, an average thermal conductivity is estimated to be 15.8 W/mK for BP. Furthermore, substrates can significantly affect the heat dissipation of the BP film, which yields a much larger effective thermal conductivity 29.2 W/mK. This work indicates that substrate can significantly impact the properties of the BP film, and the extent depends on the specific material property of interest for a given thickness.

CHAPTER 7: CONCLUSIONS

At a first glance, all the 2D materials exhibit very different properties in comparison to their bulk forms, and they are promising candidates for a variety of applications, such as miniature flexible devices. However, for most applications if not all, these 2D materials are supported by substrates. Since their thicknesses are of atomic dimension, their properties are extremely subject to be tuned by the substrates. For example, the PL of supported WS₂ monolayer quenches drastically comparing to that of suspended one, which is attributed to the charge transfer between the film and the substrate. Besides, the films are susceptible to have the morphologic variation laterally, resulting in the non-uniform film morphology, i.e. the difference in their optical and electric properties from spot to spot. Practically, there are two popular ways to fabricate 2D material that are mechanical exfoliation with scotch tape and chemical vapor deposition. But the polymeric residues from the production processes are attached to the films, which in most cases degrades the performance of the films. Even though annealing is used to remove the residues, there are still residual hydrocarbons left behind that can significantly change the properties of the films.

The overlaying theme of this dissertation is to understand the vibrational properties of these 2D materials and how the interaction of the 2D materials with their supporting substrates. In order to investigate these properties, Raman and PL spectroscopies at and above room temperature are applied to the 2D films. Four layered materials, graphene, MoS₂, WS₂ and black phosphorus, were studied with temperature-dependent Raman spectroscopy. With the temperature dependence of

their major Raman modes, we were able to look into the vibrational properties of these 2D materials, and further to examine their temperature effect on the morphology of the films supported by different substrates. Furthermore, temperature-dependent PL spectroscopy reveals the change of band gap with temperature as well the intensity quench due to the doping effect and the defect levels of 2D materials.

(A) Graphene

The main focus of graphene is to investigate how the polymeric residues affects the vibrational properties of D, G and 2D bands of graphene within a temperature range from RT to 400 °C. We have found that the annealing of graphene could not remove the polymeric residues but leave behind hydrocarbons on the top of graphene. The Raman spectrum of graphene after annealing exhibited a broadening of both D and G bands, whose features are very similar to those of amorphous carbon. The amorphous carbon originated from those polymeric residues at elevated temperature. Additionally, the nonlinear temperature dependence observed in both ME and CVD-grown graphene samples indicates the possible slippage of graphene relative to the substrate as well as the change of the film morphology.

(B) MoS₂

MoS₂ samples prepared by both CVD and ME on different substrates were investigated with temperature-dependent Raman spectroscopy. The main observations of Raman response of these samples at elevated temperature were that the temperature coefficients of in-plane E_{2g}^1 mode for CVD-grown monolayer MoS₂ were smaller than ME samples, while the out-of-plane A_{1g} mode showed stronger nonlinearity of its temperature dependence. With respect to the difference between the two sample fabrication techniques, the CVD-grown MoS₂ are bound to the substrates stronger than ME or transferred ones, while the ME or transferred MoS₂ has non-planar morphol-

ogy due to the interaction with the substrate. Therefore, the E_{2g}^1 mode of monolayer MoS₂ is more sensitive to the chemical bonding with the substrate while A_{1g} mode the film morphology. Furthermore, transferred monolayer MoS₂ on SiO₂/Si was annealed up to 300 Å°C twice to study the annealing effect on the change of vibrational properties. The results showed that the temperature dependence of A_{1g} mode in second-cycle annealing was more linear than that of first-cycle, while that of E_{2g}^1 mode in both cycles was quite linear. The reason of this change was due to the morphologic change of the film. The Raman and PL mapping results of the film revealed that the film became more planar and uniform. This further confirmed that A_{1g} mode was sensitive to the morphology of the film.

(C) WS₂

The crystalline structure of WS₂ is the same as that of MoS₂; thus, the temperature dependence of WS₂ is quite alike. The Raman and PL mapping on CVD-grown monolayer WS₂ triangles revealed that the strain distribution over the triangle is not uniform, as well as the doping/defect concentration. Using DFT calculation the maximum difference of strain over a single triangle was estimated to be $\sim 0.5\%$. With the temperature-dependent Raman measurements of CVD-grown monolayer WS₂ samples and transferred CVD monolayers, temperature dependence similar to MoS₂ was observed. Though both modes showed nonlinear temperature dependences, the dependence of E_{2g}^1 mode was more linear. However, the main discover for WS₂ samples was the strain effect originating from the difference in TEC between the film and the substrate. The TEC of WS₂ is higher than those of substrates, both sapphire and SiO₂; thus, the WS₂ monolayer undergoes tensile strain after fast cooling down during growth process. The tensile strain causes the redshift of Raman frequencies of both modes. Regarding the temperature-dependent Raman measurements, the tensile strain was released gradually, leading to the nonlinear temperature dependence

of both modes. As the CVD-grown monolayer WS_2 was transferred to SiO_2/Si substrate, the non-planar morphology gave rise to the nonlinear temperature dependence of A_{1g} mode, which was similar to MoS_2 . Moreover, temperature-dependent PL spectroscopy revealed the thermal quenching processes of CVD-grown monolayer WS_2 on SiO_2/Si and sapphire substrates, and the activation energies were estimated to be 0.40 eV for SiO_2 sample, and 0.20 eV and 1.51 eV for sapphire sample.

(D) Black phosphorus

Black phosphorus has the unique anisotropic nature due to its puckered honeycomb structure, which was revealed by the angle-resolved Raman spectroscopy. Based on the angle-resolved Raman measurements, the crystalline orientation of BP thin films could be determined. The temperature dependent Raman spectroscopy of BP films with different thicknesses exhibited that the temperature dependence was sensitive to film thickness, showing a decreasing trend in temperature coefficient with decreasing thickness, which was attributed to the interaction of the film with substrate as well as the morphology distortion of the film. Furthermore, the average thermal conductivity of BP with a thickness of ~ 70 nm was extracted from the results of both laser power and temperature dependent Raman spectroscopy, which was 15.8 W/mK. Whereas, the effective thermal conductivity of BP supported by SiO_2/Si substrate was calculated to be 29.2 W/mK, indicating that the substrate could significantly impact the properties of BP films.

In general, the work highlighted in this dissertation not only characterizes the vibrational and optical properties of four 2D materials at elevated temperatures, but also emphasizes the importance of understanding the correlation of the properties of 2D materials with strain, film morphology and doping. Most studies were focusing on the electrical and optical properties of 2D materials themselves, the interaction with substrates were seldom investigated. In this dissertation, I propose that the

substrate effect can significantly affect the properties of 2D materials in different ways. For instance, the strain originated from the interaction between the films and the substrates changes the band structure which will further affect their performance in optoelectronic applications. Therefore, this work suggests the importance to fully understand the influence from supporting substrates of 2D material before they can be used as devices, and the discoveries of this dissertation has laid the foundation for further investigation into the substrate effect on 2D materials.

REFERENCES

- [1] Richard P. Feynman. There's plenty of room at the bottom. *Engineering and science*, 23(5):22–36, 1960.
- [2] G.K. Bennig. Atomic force microscope and method for imaging surfaces with atomic resolution, February 9 1988. US Patent 4,724,318.
- [3] E. Ruska. Die elektronenmikroskopische abbildung elektronenbestrahlter oberflächen. *Zeitschrift fur Physik*, 83(7-8):492–497, 1933.
- [4] M. Von Ardenne and D. Beischer. Untersuchung von metalloxyd-rauchen mit dem universal-elektronenmikroskop. *Zeitschrift fur Elektrochemie und angewandte physikalische Chemie*, 46(4):270–277, 1940.
- [5] H. W. Kroto, J. R. Heath, S. C. O'Brien, R. F. Curl, and R. E. Smalley. C60: Buckminsterfullerene. *Nature*, 318(6042):162–163, 1985. 10.1038/318162a0.
- [6] C. G. Smith. Low-dimensional quantum devices. *Reports on Progress in Physics*, 59(2):235, 1996.
- [7] L. Esaki and R. Tsu. Superlattice and negative differential conductivity in semiconductors. *IBM Journal of Research and Development*, 14(1):61–65, 1970.
- [8] J. S. Koehler. Attempt to design a strong solid. *Physical Review B*, 2(2):547–551, 1970. PRB.
- [9] P. R. Wallace. The band theory of graphite. *Physical Review*, 71(9):622–634, 1947. PR.
- [10] K. S. Novoselov, A. K. Geim, S. V. Morozov, D. Jiang, Y. Zhang, S. V. Dubonos, I. V. Grigorieva, and A. A. Firsov. Electric field effect in atomically thin carbon films. *Science*, 306(5696):666–669, 2004.
- [11] K. S. Novoselov, A. K. Geim, S. V. Morozov, D. Jiang, M. I. Katsnelson, I. V. Grigorieva, S. V. Dubonos, and A. A. Firsov. Two-dimensional gas of massless dirac fermions in graphene. *Nature*, 438(7065):197–200, 2005. 10.1038/nature04233.
- [12] R. Arenal, O. Stephan, M. Kociak, D. Taverna, A. Loiseau, and C. Colliex. Electron energy loss spectroscopy measurement of the optical gaps on individual boron nitride single-walled and multiwalled nanotubes. *Physical Review Letters*, 95(12):127601, 2005. PRL.
- [13] Lijie Ci, Li Song, Chuanhong Jin, Deep Jariwala, Dangxin Wu, Yongjie Li, Anchal Srivastava, Z. F. Wang, Kevin Storr, Luis Balicas, Feng Liu, and Pulickel M. Ajayan. Atomic layers of hybridized boron nitride and graphene domains. *Nat Mater*, 9(5):430–435, 2010. 10.1038/nmat2711.

- [14] H. S. Ramakrishna, Matte, A. Gomathi, Arun K. Manna, Dattatray J. Late, Ranjan Datta, Swapan K. Pati, and C. N. R. Rao. MoS₂ and WS₂ analogues of graphene. *Angewandte Chemie International Edition*, 49(24):4059–4062, 2010.
- [15] Manish Chhowalla, Hyeon Suk Shin, Goki Eda, Lain-Jong Li, Kian Ping Loh, and Hua Zhang. The chemistry of two-dimensional layered transition metal dichalcogenide nanosheets. *Nat Chem*, 5(4):263–275, 2013. 10.1038/nchem.1589.
- [16] Han Liu, Adam T. Neal, Zhen Zhu, Zhe Luo, Xianfan Xu, David Tomanek, and Peide D. Ye. Phosphorene: An unexplored 2d semiconductor with a high hole mobility. *ACS Nano*, 8(4):4033–4041, 2014.
- [17] Likai Li, Yijun Yu, Guo Jun Ye, Qingqin Ge, Xuedong Ou, Hua Wu, Donglai Feng, Xian Hui Chen, and Yuanbo Zhang. Black phosphorus field-effect transistors. *Nat Nano*, 9(5):372–377, 2014.
- [18] A. H. Castro Neto, F. Guinea, N. M. R. Peres, K. S. Novoselov, and A. K. Geim. The electronic properties of graphene. *Reviews of Modern Physics*, 81(1):109–162, 2009. RMP.
- [19] F. Molitor, J. Guttinger, C. Stampfer, S. Dirscher, A. Jacobsen, T. Ihn, and K. Ensslin. Electronic properties of graphene nanostructures. *Journal of Physics: Condensed Matter*, 23(24):243201, 2011.
- [20] P. Sutter, M. S. Hybertsen, J. T. Sadowski, and E. Sutter. Electronic structure of few-layer epitaxial graphene on Ru(0001). *Nano Letters*, 9(7):2654–2660, 2009. PMID: 19505134.
- [21] Duhee Yoon, Young-Woo Son, and Hyeonsik Cheong. Negative thermal expansion coefficient of graphene measured by Raman spectroscopy. *Nano Letters*, 11(8):3227–3231, 2011.
- [22] V. P. Gusynin and S. G. Sharapov. Unconventional integer quantum hall effect in graphene. *Physical Review Letters*, 95(14):146801, 2005. PRL.
- [23] K. I. Bolotin, K. J. Sikes, Z. Jiang, M. Klima, G. Fudenberg, J. Hone, P. Kim, and H. L. Stormer. Ultrahigh electron mobility in suspended graphene. *Solid State Communications*, 146(9–10):351–355, 2008.
- [24] E. McCann, K. Kechedzhi, Vladimir I. Fal'ko, H. Suzuura, T. Ando, and B. L. Altshuler. Weak-localization magnetoresistance and valley symmetry in graphene. *Physical Review Letters*, 97(14):146805, 2006. PRL.
- [25] Young-Woo Son, Marvin L. Cohen, and Steven G. Louie. Energy gaps in graphene nanoribbons. *Phys. Rev. Lett.*, 97:216803, Nov 2006.

- [26] Gianluca Giovannetti, Petr A. Khomyakov, Geert Brocks, Paul J. Kelly, and Jeroen van den Brink. Substrate-induced band gap in graphene on hexagonal boron nitride: *Ab initio* density functional calculations. *Phys. Rev. B*, 76:073103, Aug 2007.
- [27] Yuanbo Zhang, Tsung-Ta Tang, Caglar Girit, Zhao Hao, Michael C Martin, Alex Zettl, Michael F Crommie, Y Ron Shen, and Feng Wang. Direct observation of a widely tunable bandgap in bilayer graphene. *Nature*, 459(7248):820–823, 2009.
- [28] Wonbong Choi, Indranil Lahiri, Raghunandan Seelaboyina, and Yong Soo Kang. Synthesis of graphene and its applications: A review. *Critical Reviews in Solid State and Materials Sciences*, 35(1):52–71, 2010.
- [29] Konstantin S Novoselov, VI Fal, L Colombo, PR Gellert, MG Schwab, K Kim, et al. A roadmap for graphene. *Nature*, 490(7419):192–200, 2012.
- [30] Yoichi Kubota, Kenji Watanabe, Osamu Tsuda, and Takashi Taniguchi. Deep ultraviolet light-emitting hexagonal boron nitride synthesized at atmospheric pressure. *Science*, 317(5840):932–934, 2007.
- [31] RadisavljevicB, RadenovicA, BrivioJ, GiacomettiV, and KisA. Single-layer mos2 transistors. *Nat Nano*, 6(3):147–150, 2011. 10.1038/nnano.2010.279.
- [32] Sanghyun Jo, Nicolas Ubrig, Helmuth Berger, Alexey B. Kuzmenko, and Alberto F. Morpurgo. Mono- and bilayer ws2 light-emitting transistors. *Nano Letters*, 14(4):2019–2025, 2014.
- [33] Saptarshi Das, Hong-Yan Chen, Ashish Verma Penumatcha, and Joerg Appenzeller. High performance multilayer mos2 transistors with scandium contacts. *Nano letters*, 13(1):100–105, 2012.
- [34] Bhim Chamlagain, Qing Li, Nirmal Jeevi Ghimire, Hsun-Jen Chuang, Meeghage Madusanka Perera, Honggen Tu, Yong Xu, Minghu Pan, Di Xaio, Jiaqiang Yan, et al. Mobility improvement and temperature dependence in mose2 field-effect transistors on parylene-c substrate. *ACS nano*, 8(5):5079–5088, 2014.
- [35] Hsun-Jen Chuang, Xuebin Tan, Nirmal Jeevi Ghimire, Meeghage Madusanka Perera, Bhim Chamlagain, Mark Ming-Cheng Cheng, Jiaqiang Yan, David Mandrus, David Tomašek, and Zhixian Zhou. High mobility wse2 p-and n-type field-effect transistors contacted by highly doped graphene for low-resistance contacts. *Nano letters*, 14(6):3594–3601, 2014.
- [36] Rudren Ganatra and Qing Zhang. Few-layer mos2: A promising layered semiconductor. *ACS Nano*, 8(5):4074–4099, 2014.

- [37] B. Schonfeld, J. J. Huang, and S. C. Moss. Anisotropic mean-square displacements (msd) in single-crystals of 2h- and 3r-mos₂. *Acta Crystallographica Section B*, 39(4):404–407, 1983.
- [38] Hualing Zeng, Junfeng Dai, Wang Yao, Di Xiao, and Xiaodong Cui. Valley polarization in mos₂ monolayers by optical pumping. *Nature nanotechnology*, 7(8):490–493, 2012.
- [39] Goki Eda, Hisato Yamaguchi, Damien Voiry, Takeshi Fujita, Mingwei Chen, and Manish Chhowalla. Photoluminescence from chemically exfoliated mos₂. *Nano Letters*, 11(12):5111–5116, 2011.
- [40] Jason K. Ellis, Melissa J. Lucero, and Gustavo E. Scuseria. The indirect to direct band gap transition in multilayered mos₂ as predicted by screened hybrid density functional theory. *Applied Physics Letters*, 99(26):–, 2011.
- [41] A. Kuc, N. Zibouche, and T. Heine. Influence of quantum confinement on the electronic structure of the transition metal sulfide *ts*₂. *Phys. Rev. B*, 83:245213, Jun 2011.
- [42] Eugene S. Kadantsev and Pawel Hawrylak. Electronic structure of a single mos₂ monolayer. *Solid State Communications*, 152(10):909–913, 2012.
- [43] Andrea Splendiani, Liang Sun, Yuanbo Zhang, Tianshu Li, Jonghwan Kim, Chi-Yung Chim, Giulia Galli, and Feng Wang. Emerging photoluminescence in monolayer mos₂. *Nano Letters*, 10(4):1271–1275, 2010.
- [44] Oriol Lopez-Sanchez, Dominik Lembke, Metin Kayci, Aleksandra Radenovic, and Andras Kis. Ultrasensitive photodetectors based on monolayer mos₂. *Nat Nano*, 8(7):497–501, 2013.
- [45] A. Molina-Sánchez and L. Wirtz. Phonons in single-layer and few-layer mos₂ and ws₂. *Phys. Rev. B*, 84:155413, Oct 2011.
- [46] Z. Y. Zhu, Y. C. Cheng, and U. Schwingenschlögl. Giant spin-orbit-induced spin splitting in two-dimensional transition-metal dichalcogenide semiconductors. *Physical Review B*, 84(15):153402, 2011. PRB.
- [47] R. Coehoorn, C. Haas, and R. A. de Groot. Electronic structure of mose₂, mos₂, and wse₂. ii. the nature of the optical band gaps. *Physical Review B*, 35(12):6203–6206, 1987. PRB.
- [48] R. Coehoorn, C. Haas, J. Dijkstra, C. J. F. Flipse, R. A. de Groot, and A. Wold. Electronic structure of mose₂, mos₂, and wse₂. i. band-structure calculations and photoelectron spectroscopy. *Physical Review B*, 35(12):6195–6202, 1987. PRB.
- [49] Chunxiao Cong, Jingzhi Shang, Xing Wu, Bingchen Cao, Namphung Peimyoo, Caiyu Qiu, Litao Sun, and Ting Yu. Synthesis and optical properties of large-area single-crystalline 2d semiconductor ws₂ monolayer from chemical vapor deposition. *Advanced Optical Materials*, 2(2):131–136, 2014.

- [50] Simone Bertolazzi, Jacopo Brivio, and Andras Kis. Stretching and breaking of ultrathin mos₂. *ACS Nano*, 5(12):9703–9709, 2011.
- [51] Jae-Ung Lee, Duhee Yoon, and Hyeonsik Cheong. Estimation of youngi⁻s modulus of graphene by raman spectroscopy. *Nano Letters*, 12(9):4444–4448, 2012.
- [52] Liu Leitao, S. Bala Kumar, Ouyang Yijian, and Jing Guo. Performance limits of monolayer transition metal dichalcogenide transistors. *Electron Devices, IEEE Transactions on*, 58(9):3042–3047, 2011.
- [53] D. Ovchinnikov, A. Allain, Y. S. Huang, D. Dumcenco, and A. Kis. Electrical transport properties of single-layer ws₂. *ACS Nano*, 8(8):8174–81, 2014. Ovchinnikov, Dmitry Allain, Adrien Huang, Ying-Sheng Dumcenco, Dumitru Kis, Andras eng Research Support, Non-U.S. Gov't 2014/07/30 06:00 ACS Nano. 2014 Aug 26;8(8):8174-81. doi: 10.1021/nn502362b. Epub 2014 Jul 28.
- [54] Juanxia Wu, Nannan Mao, Liming Xie, Hua Xu, and Jin Zhang. Identifying the crystalline orientation of black phosphorus using angle-resolved polarized raman spectroscopy. *Angewandte Chemie International Edition*, 54(8):2366–2369, 2015.
- [55] Shuang Zhang, Jiong Yang, Renjing Xu, Fan Wang, Weifeng Li, Muhammad Ghufuran, Yong-Wei Zhang, Zongfu Yu, Gang Zhang, Qinghua Qin, and Yuerui Lu. Extraordinary photoluminescence and strong temperature/angle-dependent raman responses in few-layer phosphorene. *ACS Nano*, 8(9):9590–9596, 2014.
- [56] M. Buscema, D. J. Groenendijk, S. I. Blanter, G. A. Steele, H. S. van der Zant, and A. Castellanos-Gomez. Fast and broadband photoresponse of few-layer black phosphorus field-effect transistors. *Nano Lett*, 14(6):3347–52, 2014. Buscema, Michele Groenendijk, Dirk J Blanter, Sofya I Steele, Gary A van der Zant, Herre S J Castellanos-Gomez, Andres eng Research Support, Non-U.S. Gov't 2014/05/14 06:00 Nano Lett. 2014 Jun 11;14(6):3347-52. doi: 10.1021/n-15008085. Epub 2014 May 13.
- [57] Yexin Deng, Zhe Luo, Nathan J. Conrad, Han Liu, Yongji Gong, Sina Najmaei, Pulickel M. Ajayan, Jun Lou, Xianfan Xu, and Peide D. Ye. Black phosphorus δ monolayer mos₂ van der waals heterojunction p δ cn diode. *ACS Nano*, 8(8):8292–8299, 2014.
- [58] Michele Buscema, Dirk J Groenendijk, Gary A Steele, Herre SJ van der Zant, and Andres Castellanos-Gomez. Photovoltaic effect in few-layer black phosphorus pn junctions defined by local electrostatic gating. *Nature communications*, 5, 2014.
- [59] Tu Hong, Bhim Chamlagain, Wenzhi Lin, Hsun-Jen Chuang, Minghu Pan, Zhixian Zhou, and Ya-Qiong Xu. Polarized photocurrent response in black phosphorus field-effect transistors. *Nanoscale*, 6(15):8978–8983, 2014.

- [60] Castellanos-Gomez Andres, Vicarelli Leonardo, Prada Elsa, O. Island Joshua, K. L. Narasimha-Acharya, I. Blanter Sofya, J. Groenendijk Dirk, Buscema Michele, A. Steele Gary, J. V. Alvarez, W. Zandbergen Henny, J. J. Palacios, and S. J. van der Zant Herre. Isolation and characterization of few-layer black phosphorus. *2D Materials*, 1(2):025001, 2014.
- [61] M. Razeghi. *Fundamentals of Solid State Engineering*. Kluwer Academic Publishers, 2002.
- [62] T.D. Steiner. *Semiconductor Nanostructures for Optoelectronic Applications*. Artech House, 2004.
- [63] H. Hiura, T. W. Ebbesen, J. Fujita, K. Tanigaki, and T. Takada. Role of sp³ defect structures in graphite and carbon nanotubes. *Nature*, 367(6459):148–151, 1994. 10.1038/367148a0.
- [64] Thomas W Ebbesen and Hidefumi Hiura. Graphene in 3-dimensions: Towards graphite origami. *Advanced Materials*, 7(6):582–586, 1995.
- [65] H. V. Roy, C. Kallinger, and K. Sattler. Study of single and multiple foldings of graphitic sheets. *Surface Science*, 407(1&3):1–6, 1998.
- [66] Lu Xuekun, Yu Minfeng, Huang Hui, and S. Ruoff Rodney. Tailoring graphite with the goal of achieving single sheets. *Nanotechnology*, 10(3):269, 1999.
- [67] Yi Zhang, Luyao Zhang, and Chongwu Zhou. Review of chemical vapor deposition of graphene and related applications. *Accounts of Chemical Research*, 46(10):2329–2339, 2013.
- [68] Min Yi and Zhigang Shen. A review on mechanical exfoliation for the scalable production of graphene. *Journal of Materials Chemistry A*, 3(22):11700–11715, 2015.
- [69] Keng-Ku Liu, Wenjing Zhang, Yi-Hsien Lee, Yu-Chuan Lin, Mu-Tung Chang, Ching-Yuan Su, Chia-Seng Chang, Hai Li, Yumeng Shi, Hua Zhang, Chao-Sung Lai, and Lain-Jong Li. Growth of large-area and highly crystalline mos₂ thin layers on insulating substrates. *Nano Letters*, 12(3):1538–1544, 2012.
- [70] Yongjie Zhan, Zheng Liu, Sina Najmaei, Pulickel M. Ajayan, and Jun Lou. Large-area vapor-phase growth and characterization of mos₂ atomic layers on a sio₂ substrate. *Small*, 8(7):966–971, 2012.
- [71] Masihur R. Laskar, Lu Ma, Santhakumar Kannappan, Pil Sung Park, Sriram Krishnamoorthy, Digbijoy N. Nath, Wu Lu, Yiyang Wu, and Siddharth Rajan. Large area single crystal (0001) oriented mos₂. *Applied Physics Letters*, 102(25):252108, 2013.

- [72] Yi-Hsien Lee, Xin-Quan Zhang, Wenjing Zhang, Mu-Tung Chang, Cheng-Te Lin, Kai-Di Chang, Ya-Chu Yu, Jacob Tse-Wei Wang, Chia-Seng Chang, Lain-Jong Li, and Tsung-Wu Lin. Synthesis of large-area mos2 atomic layers with chemical vapor deposition. *Advanced Materials*, 24(17):2320–2325, 2012.
- [73] Yu-Chuan Lin, Wenjing Zhang, Jing-Kai Huang, Keng-Ku Liu, Yi-Hsien Lee, Chi-Te Liang, Chih-Wei Chu, and Lain-Jong Li. Wafer-scale mos2 thin layers prepared by moo3 sulfurization. *Nanoscale*, 4(20):6637–6641, 2012.
- [74] Chandrasekhara Venkata Raman and Kariamanikkam Srinivasa Krishnan. A new type of secondary radiation. *Nature*, 121(3048):501–502, 1928.
- [75] Gr Landsberg and L. Mandelstam. uber die lichtzerstreuung in kristallen. *Zeitschrift fur Physik*, 50(11-12):769–780, 1928.
- [76] C. Kittel. *Introduction to solid state physics*. Wiley, 1971.
- [77] YU Peter and Manuel Cardona. *Fundamentals of semiconductors: physics and materials properties*. Springer Science & Business Media, 2010.
- [78] C. Postmus, J. R. Ferraro, and S. S. Mitra. Pressure dependence of infrared eigenfrequencies of kcl and kbr. *Phys. Rev.*, 174:983–987, Oct 1968.
- [79] Josš MenšŠndez and Manuel Cardona. Temperature dependence of the first-order raman scattering by phonons in si, ge, and α – Sn: Anharmonic effects. *Physical Review B*, 29(4):2051–2059, 1984. PRB.
- [80] W. J. Borer, S. S. Mitra, and K. V. Namjoshi. Line shape and temperature dependence of the first order raman spectrum of diamond. *Solid State Communications*, 9(16):1377–1381, 1971.
- [81] M. Balkanski, R. F. Wallis, and E. Haro. Anharmonic effects in light scattering due to optical phonons in silicon. *Physical Review B*, 28(4):1928–1934, 1983. PRB.
- [82] P. G. Klemens. Anharmonic decay of optical phonons. *Physical Review*, 148(2):845–848, 1966. PR.
- [83] YP Varshni. Temperature dependence of the energy gap in semiconductors. *Physica*, 34(1):149–154, 1967.
- [84] MD Sturge, E Cohen, and KF Rodgers. Thermal quenching processes in the low temperature photoluminescence of excitons bound to nitrogen pairs in gap. *Physical Review B*, 15(6):3169, 1977.
- [85] Yong Zhang, MD Sturge, K Kash, BP Van der Gaag, AS Gozdz, LT Florez, and JP Harbison. Temperature dependence of luminescence efficiency, exciton transfer, and exciton localization in gaas/al x ga 1- x as quantum wires and quantum dots. *Physical Review B*, 51(19):13303, 1995.

- [86] D Bimberg, M Sondergeld, and E Grobe. Thermal dissociation of excitons bounds to neutral acceptors in high-purity gaas. *Physical Review B*, 4(10):3451, 1971.
- [87] Adaobi Nwaneshiudu, Christiane Kuschal, Fernanda H. Sakamoto, R. Rox Anderson, Kathryn Schwarzenberger, and Roger C. Young. Introduction to confocal microscopy. *J Invest Dermatol*, 132(12):e3, 2012.
- [88] M. Minsky. Memoir on inventing the confocal scanning microscope. *Scanning*, 10(4):128–138, 1988.
- [89] Marvin Minsky. Microscopy apparatus, December 19 1961. US Patent 3,013,467.
- [90] K. S. Novoselov, D. Jiang, F. Schedin, T. J. Booth, V. V. Khotkevich, S. V. Morozov, and A. K. Geim. Two-dimensional atomic crystals. *Proceedings of the National Academy of Sciences of the United States of America*, 102(30):10451–10453, 2005.
- [91] A. C. Ferrari, J. C. Meyer, V. Scardaci, C. Casiraghi, M. Lazzeri, F. Mauri, S. Piscanec, D. Jiang, K. S. Novoselov, S. Roth, and A. K. Geim. Raman spectrum of graphene and graphene layers. *Physical Review Letters*, 97(18):187401, 2006. PRL.
- [92] PingHeng Tan, YuanMing Deng, and Qian Zhao. Temperature-dependent raman spectra and anomalous raman phenomenon of highly oriented pyrolytic graphite. *Physical Review B*, 58(9):5435–5439, 1998. PRB.
- [93] Stephanie Reich and Christian Thomsen. Raman spectroscopy of graphite. *Philosophical Transactions of the Royal Society of London A: Mathematical, Physical and Engineering Sciences*, 362(1824):2271–2288, 2004.
- [94] R Kostić, M Mirić, T Radić, M Radović, R Gajić, and ZV Popović. Optical characterization of graphene and highly oriented pyrolytic graphite. *Acta Physica Polonica A*, 116(4):718–721, 2009.
- [95] A. Gupta, G. Chen, P. Joshi, S. Tadigadapa, and Eklund. Raman scattering from high-frequency phonons in supported n-graphene layer films. *Nano Letters*, 6(12):2667–2673, 2006.
- [96] C. Thomsen and S. Reich. Double resonant raman scattering in graphite. *Physical Review Letters*, 85(24):5214–5217, 2000. PRL.
- [97] Axel Eckmann, Alexandre Felten, Artem Mishchenko, Liam Britnell, Ralph Krupke, Kostya S Novoselov, and Cinzia Casiraghi. Probing the nature of defects in graphene by raman spectroscopy. *Nano letters*, 12(8):3925–3930, 2012.
- [98] D. M. Basko. Theory of resonant multiphonon raman scattering in graphene. *Physical Review B*, 78(12):125418, 2008. PRB.

- [99] Pedro Venezuela, Michele Lazzeri, and Francesco Mauri. Theory of double-resonant raman spectra in graphene: Intensity and line shape of defect-induced and two-phonon bands. *Physical Review B*, 84(3):035433, 2011. PRB.
- [100] Matteo Bruna, Anna K. Ott, Mari Ij's, Duhee Yoon, Ugo Sassi, and Andrea C. Ferrari. Doping dependence of the raman spectrum of defected graphene. *ACS Nano*, 8(7):7432–7441, 2014.
- [101] Zengguang Cheng, Qiaoyu Zhou, Chenxuan Wang, Qiang Li, Chen Wang, and Ying Fang. Toward intrinsic graphene surfaces: A systematic study on thermal annealing and wet-chemical treatment of sio2-supported graphene devices. *Nano Letters*, 11(2):767–771, 2011.
- [102] I. Calizo, A. A. Balandin, W. Bao, F. Miao, and C. N. Lau. Temperature dependence of the raman spectra of graphene and graphene multilayers. *Nano Letters*, 7(9):2645–2649, 2007.
- [103] Zhou Haiqing, Qiu Caiyu, Yu Fang, Yang Huaichao, Chen Minjiang, Hu Lijun, Guo Yanjun, and Sun Lianfeng. Raman scattering of monolayer graphene: the temperature and oxygen doping effects. *Journal of Physics D: Applied Physics*, 44(18):185404, 2011.
- [104] Mingyuan Huang, Hugen Yan, Tony F. Heinz, and James Hone. Probing strain-induced electronic structure change in graphene by raman spectroscopy. *Nano Letters*, 10(10):4074–4079, 2010.
- [105] Yifei Yu, Chun Li, Yi Liu, Liqin Su, Yong Zhang, and Linyou Cao. Controlled scalable synthesis of uniform, high-quality monolayer and few-layer mos2 films. *Scientific reports*, 3, 2013.
- [106] X. Zhang, W. P. Han, J. B. Wu, S. Milana, Y. Lu, Q. Q. Li, A. C. Ferrari, and P. H. Tan. Raman spectroscopy of shear and layer breathing modes in multilayer mos₂. *Phys. Rev. B*, 87:115413, Mar 2013.
- [107] Mahdi Ghorbani-Asl, Nourdine Zibouche, Mohammad Wahiduzzaman, Augusto F Oliveira, Agnieszka Kuc, and Thomas Heine. Electromechanics in mos2 and ws2: nanotubes vs. monolayers. *Scientific reports*, 3, 2013.
- [108] Hong Li, Qing Zhang, Chin Chong Ray Yap, Beng Kang Tay, Teo Hang Tong Edwin, Aurelien Olivier, and Dominique Baillargeat. From bulk to monolayer mos2: Evolution of raman scattering. *Advanced Functional Materials*, 22(7):1385–1390, 2012.
- [109] Changgu Lee, Hugen Yan, Louis E. Brus, Tony F. Heinz, James Hone, and Sunmin Ryu. Anomalous lattice vibrations of single- and few-layer mos2. *ACS Nano*, 4(5):2695–2700, 2010. PMID: 20392077.
- [110] AG Bagnall, WY Liang, EA Marseglia, and B Welber. Raman studies of mos 2 at high pressure. *Physica B+ C*, 99(1):343–346, 1980.

- [111] Tianshu Li, , and Giulia Galli*. Electronic properties of mos2 nanoparticles. *The Journal of Physical Chemistry C*, 111(44):16192–16196, 2007.
- [112] Ting Cao, Gang Wang, Wenpeng Han, Huiqi Ye, Chuanrui Zhu, Junren Shi, Qian Niu, Pingheng Tan, Enge Wang, Baoli Liu, et al. Valley-selective circular dichroism of monolayer molybdenum disulphide. *Nature communications*, 3:887, 2012.
- [113] Kin Fai Mak, Changgu Lee, James Hone, Jie Shan, and Tony F. Heinz. Atomically thin mos₂: A new direct-gap semiconductor. *Physical Review Letters*, 105(13):136805, 2010. PRL.
- [114] Nils Scheuschner, Oliver Ochedowski, Anne-Marie Kaulitz, Roland Gillen, Mari-ka Schleberger, and Janina Maultzsch. Photoluminescence of freestanding single- and few-layer mos₂. *Phys. Rev. B*, 89:125406, Mar 2014.
- [115] Kin Fai Mak, Keliang He, Changgu Lee, Gwan Hyoung Lee, James Hone, Tony F Heinz, and Jie Shan. Tightly bound trions in monolayer mos₂. *Nature materials*, 12(3):207–211, 2013.
- [116] Nicolas Mounet and Nicola Marzari. First-principles determination of the structural, vibrational and thermodynamic properties of diamond, graphite, and derivatives. *Phys. Rev. B*, 71:205214, May 2005.
- [117] Tsachi Livneh and Eran Sterer. Resonant raman scattering at exciton states tuned by pressure and temperature in 2h-mos₂. *Phys. Rev. B*, 81:195209, May 2010.
- [118] Sina Najmaei, Pulickel M Ajayan, and J Lou. Quantitative analysis of the temperature dependency in raman active vibrational modes of molybdenum disulfide atomic layers. *Nanoscale*, 5(20):9758–9763, 2013.
- [119] Satyaprakash Sahoo, Anand PS Gaur, Majid Ahmadi, Maxime J-F Guinel, and Ram S Katiyar. Temperature-dependent raman studies and thermal conductivity of few-layer mos₂. *The Journal of Physical Chemistry C*, 117(17):9042–9047, 2013.
- [120] Zhen Hua Ni, Hao Min Wang, Zhi Qiang Luo, Ying Ying Wang, Ting Yu, Yi Hong Wu, and Ze Xiang Shen. The effect of vacuum annealing on graphene. *Journal of Raman Spectroscopy*, 41(5):479–483, 2010.
- [121] SH El-Mahalawy and BL Evans. The thermal expansion of 2h-mos₂, 2h-mose₂ and 2h-wse₂ between 20 and 800 c. *Journal of Applied Crystallography*, 9(5):403–406, 1976.
- [122] Biswanath Chakraborty, Achintya Bera, DVS Muthu, Somnath Bhowmick, Umesh V Waghmare, and AK Sood. Symmetry-dependent phonon renormalization in monolayer mos 2 transistor. *Physical Review B*, 85(16):161403, 2012.

- [123] Wu Zhou, Xiaolong Zou, Sina Najmaei, Zheng Liu, Yumeng Shi, Jing Kong, Jun Lou, Pulickel M Ajayan, Boris I Yakobson, and Juan-Carlos Idrobo. Intrinsic structural defects in monolayer molybdenum disulfide. *Nano letters*, 13(6):2615–2622, 2013.
- [124] Alper Gurarlsan, Yifei Yu, Liqin Su, Yiling Yu, Francisco Suarez, Shanshan Yao, Yong Zhu, Mehmet Ozturk, Yong Zhang, and Linyou Cao. Surface-energy-assisted perfect transfer of centimeter-scale monolayer and few-layer mos2 films onto arbitrary substrates. *ACS nano*, 8(11):11522–11528, 2014.
- [125] Ji Feng, Xiaofeng Qian, Cheng-Wei Huang, and Ju Li. Strain-engineered artificial atom as a broad-spectrum solar energy funnel. *Nature Photonics*, 6(12):866–872, 2012.
- [126] Ayse Berkdemir, Humberto R Gutiérrez, Andrés R Botello-Méndez, Néstor Perea-López, Ana Laura Elías, Chen-Ing Chia, Bei Wang, Vincent H Crespi, Florentino López-Urías, Jean-Christophe Charlier, et al. Identification of individual and few layers of ws2 using raman spectroscopy. *Scientific reports*, 3, 2013.
- [127] Xi Ling, LG Moura, Marcos A Pimenta, and Jin Zhang. Charge-transfer mechanism in graphene-enhanced raman scattering. *The Journal of Physical Chemistry C*, 116(47):25112–25118, 2012.
- [128] Seok Daniel Namgung, Suk Yang, Kyung Park, Ah-Jin Cho, Hojoong Kim, and Jang-Yeon Kwon. Influence of post-annealing on the off current of mos2 field-effect transistors. *Nanoscale research letters*, 10(1):1–6, 2015.
- [129] Freddie Withers, Thomas Hardisty Bointon, David Christopher Hudson, Monica Felicia Craciun, and Saverio Russo. Electron transport of ws2 transistors in a hexagonal boron nitride dielectric environment. *Scientific reports*, 4, 2014.

APPENDIX A: QUADRATIC FIT COMPARISON GRAPHS

The appendices should be used for whatever material you or your advisory committee believes should be included, but would not be appropriate in the text of the thesis or dissertation. Such materials can include:

1. the original data obtained in the thesis or dissertation research, including computer programs and printouts, surveys, or correspondence;
2. detailed descriptions of procedures, which go beyond the general outline of methods and approaches presented in the text;
3. a particularly extensive review of the literature and other information that may be useful to future scholars who may wish to delve more deeply into the research topic.

A.1 Section in appendix

This is a section in the appendix.

VITA

If you decide to include a vita (a biosketch about yourself), you would include the text of your vita here.

The thesis or dissertation may conclude with a biographical sketch of the author. The sketch should be written in the third person and should indicate birth date and birthplace, where the author earned the bachelor's degree and if applicable the master's degree, professional societies to which the authors belongs, and other professional activities.